

University of Mississippi

eGrove

Electronic Theses and Dissertations

Graduate School

2016

Anodic Metal Dissolution In Haloaluminate Molten Salts/Ionic Liquids

Chen Wang
University of Mississippi

Follow this and additional works at: <https://egrove.olemiss.edu/etd>

 Part of the [Chemistry Commons](#)

Recommended Citation

Wang, Chen, "Anodic Metal Dissolution In Haloaluminate Molten Salts/Ionic Liquids" (2016). *Electronic Theses and Dissertations*. 925.

<https://egrove.olemiss.edu/etd/925>

This Dissertation is brought to you for free and open access by the Graduate School at eGrove. It has been accepted for inclusion in Electronic Theses and Dissertations by an authorized administrator of eGrove. For more information, please contact egrove@olemiss.edu.

ANODIC METAL DISSOLUTION IN HALOALUMINATE MOLTEN SALTS/IONIC
LIQUIDS

A Dissertation

Presented in partial fulfillment of the requirements
for the degree of Doctor of Philosophy
in the Department of Chemistry and Biochemistry
The University of Mississippi

by

Chen Wang

August, 2016

Copyright Chen Wang 2016

ALL RIGHT RESERVED

ABSTRACT

The anodization of aluminium was investigated in the low-melting, mixed halide molten salt system, $\text{LiAlBr}_4\text{-NaAlCl}_4\text{-KAlCl}_4$ (30-50-20 m/o), and in the Lewis acidic chloroaluminate ionic liquid, aluminum chloride-1-ethyl-3-methylimidazolium chloride ($\text{AlCl}_3\text{-EtMeImCl}$) using rotating disk electrode voltammetry. In both cases, at modest overpotentials, the anodization reaction proceeds under mixed kinetic/mass-transport control. However, at larger positive overpotentials and correspondingly higher anodization rates, the reaction transitions to a mass transport-limited process governed by the dissolution of a passive layer of $\text{AlCl}_3(\text{s})$ and/or $\text{AlBr}_3(\text{s})$ on the electrode surface. In $\text{AlCl}_3\text{-EtMeImCl}$, the passive current density scales linearly with the concentration of AlCl_4^- in the ionic liquid. The heterogeneous rate constant, referenced to the equilibrium potential, and the transfer coefficient of the Al anodization reaction were measured in the absence of passivation in both ionic solvents. The exchange current densities were independent of the composition of the $\text{AlCl}_3\text{-EtMeImCl}$ ionic liquid, and the anodic transfer coefficients were close to zero in both cases. Surprisingly, the kinetic results were independent of the Al grain size.

The anodic dissolution of copper was also investigated in the $\text{AlCl}_3\text{-EtMeImCl}$ ionic liquid. A kinetic analysis of the anodic dissolution of copper in the Lewis acidic and basic compositions of the $\text{AlCl}_3\text{-EtMeImCl}$ ionic liquid was completed. In the Lewis acidic ionic liquid, the current density is potential-dependent and time-independent under all experimental

conditions. That is, the anodization of copper proceeds under mixed kinetic/mass-transport control without complication from surface species, e.g., salt precipitates. However, in the Lewis basic ionic liquids, when the anodic dissolution rate is increased above a certain critical value, the current density becomes potential-independent. This behavior is due to the formation of a CuCl surface film, and the passive current density is governed by the dissolution of this species. At lower anodization rates, when the Cu reaction exhibits mixed control, modeling indicated that CuCl_2^- is the diffusion-limited species. The anodic transfer coefficient was close to 0.5.

ACKNOWLEDGMENTS

First, I would like to express my sincere gratitude for the help and guidance provided by my research advisor, Dr. Charles L. Hussey. Teaching someone experimental techniques is easy; teaching someone to think is difficult. Over the years of my Ph.D. study, I have not only gained diverse experimental skills that will help me solve difficult problems in electrochemistry, but also the ability to solve all kinds of problems in my own life, such as fixing a broken pipe in my kitchen, making a simple vacuum system for experiments inside the glovebox, annealing glassware, and soldering different kinds of materials. More importantly, he taught me that Ph.D. stands for Doctor of Philosophy, which has certain meaning and expectations. Learning the way to identify, think, and solve the problems you encounter, is the true meaning of the degree. That's what a person who has the Ph.D. degree should be able to do. I am still aspiring to be better, but no one can deny that all the things he taught me have already made me a better scholar, a better scientist, a better husband, a better father, and most importantly, a better man.

Second, I would like to express my thanks to all of my committee members, Dr. Walter E. Cleland, Dr. Steve Davis, Dr. Jason Ritchie, and Dr. Wei-Yin Chen, for their support and advice during my graduate studies.

Third, I want to thank all of my previous and current lab colleagues, Dr. Li-Hsien Chou, Dr. Yunfeng Pan, Dr. Lorlyn Reidy and Mr. Kurachi Akifumi. They made my journey to the Ph.D. degree much more pleasant and enjoyable.

Finally, many thanks to my wife and my daughter. Their mental support cannot be replaced by anything in the world. My whole family has given me great encouragement and support, which makes me a better person. Especially, I would like to thank my parents-in-law for their continuous support and taking care of my daughter while I was not able to do so.

Financial support for this work was funded by the Strategic Environmental Research and Development Program (SERDP) through contract DE-AC05-00OR22725 to Oak Ridge National Laboratory with subcontract to the University of Mississippi.

*To my dear wife, Jing Ma,
You are my heart. You always have been. You always will be.*

RATIONAL

The role of metal anodes in electrochemical devices and processes is often neglected or at best, poorly understood. For example, various low equivalent weight metals, e.g., lithium, sodium, and aluminum, are often employed as anodes in high energy density batteries. During the cell discharge process, slow electron-transfer kinetics at the anode as well as anode dissolution reactions resulting in passive film formation can potentially limit the overall cell reaction rate,^{1,2} i.e., the cell reaction becomes anode- rather than cathode-limited.

Some other processes involving the electrochemical dissolution of metals are electrochemical machining (ECM) and electropolishing.³⁻⁷ The former is employed to selectively remove large amounts of material from a metal surface to obtain a complex shape, whereas the latter is used to clean or smooth metal surfaces as well as intentionally passivate surfaces in preparation for chemical modification processes. ECM is invaluable for the modification of hard-to-machine materials such as aluminum, titanium, and most especially steel, where traditional physical machining methods not only result in excessive cutting-tool wear, but are also difficult to apply to surfaces with complex shapes. As expected, the anode reaction is critical to the success of both the ECM and electrochemical machining processes. For example, the anodic dissolution of metal substrates under convective mass-transport conditions can often lead to considerable improvement of the surface roughness of the substrate.

Finally, the well-behaved anodic dissolution of metals is crucial to the success of the electroplating processes in cells that employ anodes of the metal being plated. This application

is perhaps less affected by the anode reaction than the others listed above because it is usually possible to avoid current limitations by making the anode surface area substantially larger than the cathode where the actual plating reaction takes place. Nevertheless, there are still instances where anode limitations can affect the overall success of the plating reaction.

Most prior investigations of electrochemical metal dissolution have been undertaken in aqueous solutions in conjunction with studies of metal surface corrosion processes.⁸ A recent monograph gives examples of the thoroughness of this work and the great body of information that has been amassed.⁹ However, much less is known about anodic dissolution in highly conductive non-aqueous solvents such as molten salts and ionic liquids. The advantages of these ionic solvents as electrolytes for batteries and fuel cells, for electrochemical machining and electropolishing, and for the electroplating of different metals are numerous.¹⁰ First, most of these liquids can solvate a variety of reducible metal ions. Second, they exhibit high intrinsic conductivities and low vapor pressures. And third, they do not contain water. The latter factor avoids the formation of oxide and hydroxide films on the anode surface during the dissolution process. The formation of these films limits the efficacy of the electropolishing process. Finally, some of the ionic liquids exhibit Lewis acid-base chemistry, which offers the opportunity to tailor the solvation environment for many metal ions. Surprisingly, little is known about the factors affecting the anode reaction rate in ionic liquids. In this investigation, we intend to investigate the anodic dissolution process for some common electrode reactions in two different ionic liquids: the moisture reactive chloroaluminate system resulting from the combination of aluminum chloride (AlCl_3) with a quaternary ammonium chloride salt, 1-ethyl-3-

methylimidazolium chloride (EtMeImCl), and the hydrophobic ionic liquid, 1-ethyl-3-methylimidazolium bis(trifluoromethylsulfonyl)imide (EtMeImTf₂N). The goal of this investigation is to probe the nature of the electrode reaction and the electron transfer rate for the electrodisolution of aluminum and copper in the former and copper in the latter.

In all cases mentioned above, a thorough investigation of electrode performance, in which all aspects of the processes affecting the electrode reaction rate and the chemical reversibility of the electrode reaction are required.

TABLE OF CONTENTS

| | |
|---|-------|
| ABSTRACT | ii |
| ACKNOWLEDGMENTS | iv |
| RATIONAL | vii |
| LIST OF ABBREVIATIONS AND SYMBOLS | xiii |
| LIST OF TABLES | xviii |
| LIST OF FIGURES | xix |
| CHAPTER 1 INTRODUCTION | 1 |
| 1.1 History of Haloaluminate Molten Salts and Ionic Liquids | 1 |
| 1.2 Dissolution of Al in Inorganic Chloroaluminate Molten Salts | 5 |
| 1.3 Dissolution of Al in Organic Chloroaluminate Ionic Liquids | 8 |
| 1.4 Dissolution of Copper | 10 |
| 1.5 Techniques for the Investigation of Electrode Reactions..... | 15 |
| 1.5.1 Rotating Disk Electrode Voltammetry..... | 17 |
| 1.5.2 Chronoamperometry | 26 |
| 1.5.3 Electrochemical Impedance Spectroscopy | 30 |
| 1.6 Research Objectives | 32 |

| | | |
|-----------|---|----|
| CHAPTER 2 | EXPERIMENTAL..... | 36 |
| 2.1 | Preparation and Purification of the Chloroaluminate Ionic Solvents..... | 36 |
| 2.1.1 | LiAlBr ₄ -NaAlCl ₄ -KAlCl ₄ (30-50-20 m/o) Molten Salt..... | 36 |
| 2.1.2 | AlCl ₃ -EtMeImCl Ionic Liquids..... | 36 |
| 2.2 | Density and Viscosity Measurements | 37 |
| 2.3 | Electrochemical Measurements..... | 38 |
| CHAPTER 3 | RESULTS AND DISCUSSION..... | 41 |
| 3.1 | Aluminum Anodization in the LiAlBr ₄ -NaAlCl ₄ -KAlCl ₄ Molten Salt..... | 41 |
| 3.1.1 | Determination of Physical and Transport Properties | 41 |
| 3.1.2 | Anodization of Al Electrodes..... | 49 |
| 3.1.3 | Heterogeneous Kinetics of the Al Anodization Reaction..... | 51 |
| 3.1.4 | Summary..... | 60 |
| 3.2 | Anodic Dissolution of Aluminum in the Aluminum Chloride-1-Ethyl-3-methylimidazolium Chloride Molten Salt..... | 61 |
| 3.2.1 | Characterization of the Al Anode Film in AlCl ₃ -EtMeImCl..... | 61 |
| 3.2.2 | Anodic Dissolution Experiments | 61 |
| 3.2.3 | Dissolution of Al under Passive Conditions | 66 |
| 3.2.4 | Dissolution of Al under Active Conditions | 73 |

| | | |
|-------|--|-----|
| 3.2.5 | Electron Backscatter Diffraction..... | 89 |
| 3.2.6 | Summary | 93 |
| 3.3 | Lewis Acid-Dependent Copper Anodization in the AlCl ₃ -EtMeImCl Ionic Liquid..... | 93 |
| 3.3.1 | Cu anodization in Acidic Ionic Liquids | 93 |
| 3.3.2 | Anodic Dissolution of Copper in Basic Chloroaluminate Ionic Liquids | 101 |
| 3.3.3 | Summary | 115 |
| | LIST OF REFERENCES | 117 |
| | VITA | 122 |

LIST OF ABBREVIATIONS AND SYMBOLS

| | |
|---------------------------|--|
| A | : Electrode surface area, cm^2 |
| BuMeImTf ₂ N | : 1-(1-Butyl)-3-methylimidazolium bis(trifluoromethylsulfonyl)imide |
| BuMePyroTf ₂ N | : 1-(1-Butyl)-1-methylpyrrolidinium bis(trifluoromethylsulfonyl)imide |
| C^* | : Bulk concentration of electroactive species, mol or mmol cm^{-3} |
| C_O^* | : Bulk concentration of oxidized species, mol or mmol cm^{-3} |
| C_R^* | : Bulk concentration of reduced species, mol or mmol cm^{-3} |
| C_{Cl^-} | : Bulk concentration of chloride ion, mol or mmol cm^{-3} |
| CE | : Counter electrode |
| CV | : Cyclic voltammetry |
| D_i | : Diffusion coefficient, $\text{cm}^2 \text{s}^{-1}$ |
| D_O | : Diffusion coefficient of the oxidized Species, $\text{cm}^2 \text{s}^{-1}$ |
| D_R | : Diffusion coefficient of the reduced Species, $\text{cm}^2 \text{s}^{-1}$ |
| E | : Electrode potential, V |
| E^0 | : Standard electrode potential, V |
| $E^{0'}$ | : Formal electrode potential, V |
| E_{app} | : Applied potential, V |

| | |
|---------------------------|--|
| E_{cell} | : Cell potential, V |
| E_{eq} | : Equilibrium potential, V |
| E_{ref} | : Standard electrode potential, V |
| E_a | : Activation energy, kJ mol^{-1} |
| $E_{a,\eta}$ | : Activation energy for absolute viscosity, kJ mol^{-1} |
| $E_{a,\Lambda}$ | : Activation energy for molar conductance, kJ mol^{-1} |
| EtMeImCl | : 1-Ethyl-3-methylimidazolium chloride |
| EtMeImTf ₂ N | : 1-Ethyl-3-methylimidazolium bis(trifluoromethylsulfonyl)imide |
| EBS | : Electron backscatter diffraction |
| ECM | : Electrochemical machining |
| EDS | : Energy dispersive x-ray spectroscopy |
| EIS | : Electrochemical impedance spectroscopy |
| F | : Faraday constant, 96485 C eq^{-1} |
| ΔG_a^\ddagger | : Gibbs free energy of activation, kJ mol^{-1} |
| $\Delta G_{a,0}^\ddagger$ | : Apparent activation energy, kJ mol^{-1} |
| i_l | : Limiting current, A |
| $i_{l,a}$ | : Anodic limiting current, A |

| | |
|------------|---|
| $i_{l,c}$ | : Cathodic limiting current, A |
| j_l | : Limiting current density, A |
| K_{eq} | : Equilibrium constant |
| k_a | : Anodic heterogeneous rate constant, cm s^{-1} |
| k_c | : Cathodic heterogeneous rate constant, cm s^{-1} |
| k^0 | : Standard heterogeneous rate constant, cm s^{-1} |
| M | : Metal |
| M_x | : Molecular weight |
| m/o | : Percent mole fraction |
| m_o | : Mass transport coefficient (m/s) |
| m.p. | : Melting point |
| n | : Number of electrons in the charge transfer step |
| OCP | : Open circuit potential |
| R | : Molar gas constant, $8.314 \text{ J mol}^{-1} \text{ K}^{-1}$ |
| R_{ct} | : Charge transfer resistance, Ω |
| R_Ω | : Solution resistance, Ω |
| RDE | : Rotating disk electrode |

| | |
|------------|--|
| RDEV | : Rotating disk electrode voltammetry |
| RE | : Reference electrode |
| SCE | : Saturated calomel electrode |
| SSC | : Silver/silver chloride electrode |
| T | : Temperature, K |
| W | : Warburg impedance, Ω |
| x | : Mole fraction |
| Z | : Impedance, Ω |
| Z_{re} | : Real impedance, Ω |
| Z_{im} | : Imaginary impedance, Ω |
| α | : Transfer coefficient |
| α_a | : Anodic transfer coefficient |
| α_c | : Cathodic transfer coefficient |
| η | : a. Overpotential, V or mV : b. Absolute viscosity, cP |
| κ | : Specific conductance, $\text{cm}^{-1} \Omega^{-1}$ |
| Λ | : Molar conductance, $\text{cm}^2 \Omega^{-1} \text{mol}^{-1}$ |

ν : a. Voltammetric potential scan rate, V s^{-1}
: b. Kinematic viscosity, $\text{cm}^2 \text{s}^{-1}$

ρ : Density, g cm^{-3}

ω : Electrode rotation frequency, rad s^{-1}

δ : Diffusion layer thickness

LIST OF TABLES

| | |
|--|-----|
| Table 3.1.1: Density, molar conductivity, and viscosity as a function of temperature for LiAlBr ₄ -NaAlCl ₄ -KAlCl ₄ (30-50-20 m/o)..... | 42 |
| Table 3.1.2: Fitted parameters for density, molar conductivity, and viscosity, from Eq. 3.1.1 and 3.1.3..... | 43 |
| Table 3.1.3: Physical and transport properties of various molten salts and ionic liquids..... | 46 |
| Table 3.2.1: RDE results for the anodization of Al in the AlCl ₃ -EtMeImCl ionic liquid..... | 90 |
| Table 3.3.1: RDE results for the anodization of Al in the Lewis basic AlCl ₃ -EtMeImCl ionic liquid. | 116 |

LIST OF FIGURES

| | |
|---|----|
| Figure 1.5.1: A classic three electrode cell..... | 18 |
| Figure 1.5.2: Representation of fluid velocities near a rotating disk electrode. | 21 |
| Figure 1.5.3: Concentration profiles and approximate diffusion layer thicknesses..... | 22 |
| Figure 1.5.4: Example of a typical Tafel plot. | 27 |
| Figure 1.5.5: (a) Waveform for a step experiment. (b) Concentration profiles for various times. | 29 |
| Figure 1.5.6: A typical CA plot for the oxidation of a metal at a RDE. | 31 |
| Figure 1.5.7: A typical impedance plot for a Randles cell model. | 34 |
| Figure 1.5.8: A Nyquist plot from a typical surface film. | 35 |
| Figure 3.1.1: Walden plots for: (○) LiAlBr ₄ -NaAlCl ₄ -KAlCl ₄ (30-50-20 m/o), (□) AlCl ₃ -NaCl (50-50 m/o), (△) AlCl ₃ -MeEtImCl (50-50 m/o), and (●) BuMePyroTf ₂ N. The solid line is the ideal line for a 1 M aqueous KCl solution. | 48 |
| Figure 3.1.2: Current-time plots recorded during the anodization of an Al RDE at different overpotentials: (a) 0.10 V, (b) 0.20 V, (c) 0.30 V, (d) 0.40 V, (e) 0.50 V, (f) 0.60 V, (g) 0.70 V, and (h) 0.80 V. The temperature was (upper) 111 °C and (lower) 131 °C. The rotation rates were 157 rad s ⁻¹ | 53 |
| Figure 3.1.3: Current-sampled voltammograms constructed from the data in Fig. 3.1.1 and 3.1.2: (○) 111°C and 10 s; (●) 111°C and 300 s, (□) 131°C and 10 s, and (■) 131°C and 300 s. The rotation rates were 157 rad s ⁻¹ | 54 |

Figure 3.1.4: Levich plots for the anodization of an Al RDE in the molten salt at (a) 111°C and (b) 131°C. The currents were sampled at 300 s. 55

Figure 3.1.5: (a) Levich plots for the anodization of an Al RDE in the molten salt at 151°C. The currents were sampled at 300 s; (b) Koutecky-Levich plots constructed from the data in (a). 57

Figure 3.1.6: Plot of the anodic rate constant versus the overpotential calculated from data similar to that shown in Fig. 3.1.5b. The results shown here are the average values of five independent experiments. 58

Figure 3.1.7: Arrhenius plot for the anodic rate constant referenced to the equilibrium potential. 59

Figure 3.2.1(A): Current-time plots recorded during the anodization of Electrode A at different anodic overpotentials in the 65 m/o ionic liquid: (a) 0.045 V, (b) 0.096 V, (c) 0.143 V, (d) 0.181 V, (e) 0.213 V, (f) 0.478 V, (g) 0.578 V, (h) 0.678 V, (i) 0.778 V and (j) 0.878 V. The temperature was 32 °C, and the electrode rotation rates were 157 rad s⁻¹. 64

Figure 3.2.1(B): Current-time plots recorded during the anodization of electrode B at different anodic overpotentials in the 65 m/o ionic liquid: (a) 0.028 V, (b) 0.060 V, (c) 0.093 V, (d) 0.125 V, (e) 0.153 V, (f) 0.178 V, (g) 0.202 V, (h) 0.428 V, (i) 0.668 V and (j) 0.766 V. The temperature was 32 °C, and the electrode rotation rates were 157 rad s⁻¹. 65

Figure 3.2.1(C): Current-time plots recorded during the anodization of electrode C at different anodic overpotentials in the 65 m/o ionic liquid: (a) 0.028 V, (b) 0.089 V, (c) 0.151 V, (d) 0.208 V, (e) 0.256 V, (f) 0.318 V, (g) 0.893 V, (h) 1.086 V, and (i) 1.273 V. The temperature was 32 °C, and the electrode rotation rates were 157 rad s⁻¹. 66

Figure 3.2.2: Current-sampled voltammograms constructed from data similar to that shown in Fig. 3.2.1 for Electrode A, but at different ionic liquid compositions and temperatures: (a) 32 °C; (●) 51 m/o, (■) 54 m/o, (▲) 58 m/o, (◆) 62 m/o, and (▼) 65 m/o AlCl₃; (b) 65 m/o AlCl₃; (●) 32°C, (■) 41°C, (▲) 51°C, and (◆) 62°C. The electrode rotation rate was 157 rad s⁻¹..... 68

Figure 3.2.3: Plot of the critical current density, j_{crit} , versus the ionic liquid composition for Electrode A. The temperature was 32 °C, and the electrode rotation rate was 157 rad s⁻¹. The line is drawn to aid the eye. 69

Figure 3.2.4: Levich plots for the passive limiting currents measured at (●) Electrode A, (■) Electrode B, and (▲) Electrode C in the 65 m/o ionic liquid at an anodic overpotential of 1.0 V. The temperature was 32 °C..... 70

Figure 3.2.5: Viscosity-corrected passive limiting current densities versus the AlCl₄⁻ concentration for Electrode A. In each case, the temperature was 32 °C, and the electrode rotation rate was 157 rad s⁻¹. The limiting currents were measured at an anodic overpotential of 1.0 V..... 74

Figure 3.2.6(A): Example of Levich plots for the anodization of Electrode A at 32°C in the 65 m/o ionic liquid. The currents were sampled at 300 s. The anodic overpotentials were: (●) 0.053 V, (■) 0.082 V, (▲) 0.111 V, (◆) 0.130 V, (▼) 0.144 V, (○) 0.160 V, (□) 0.174 V, and (△) 0.190 V 75

Figure 3.2.6(B): Example of Levich plots for the anodization of Electrode B at 32°C in the 65 m/o ionic liquid. The currents were sampled at 300 s. The anodic overpotentials were: (●)

0.025 V, (■) 0.040 V, (▲) 0.055 V, (◆) 0.065 V, (▼) 0.075 V, (○) 0.086 V, (□) 0.097 V, and (△) 0.108 V 76

Figure 3.2.6(C): Example of Levich plots for the anodization of Electrode C at 32°C in the 65 m/o ionic liquid. The currents were sampled at 300 s. The anodic overpotentials were: (●) 0.028 V, (■) 0.043 V, (▲) 0.058 V, (◆) 0.068 V, (▼) 0.078 V, (○) 0.088 V, (□) 0.098 V, and (△) 0.108 V 77

Figure 3.2.7(A): Example of Koutecky-Levich plots for Electrode A constructed from the data in Fig. 3.2.6(A): The anodic overpotentials were the same as those given in this figure. The dashed lines are drawn to aid the eye..... 80

Figure 3.2.7(B): Example of Koutecky-Levich plots for Electrode B constructed from the data in Fig. 3.2.6(B): The anodic overpotentials were the same as those given in this figure. The dashed lines are drawn to aid the eye..... 81

Figure 3.2.7(C): Example of Koutecky-Levich plots for Electrode C constructed from the data in Fig. 3.2.6(C): The anodic overpotentials were the same as those given in this figure. The dashed lines are drawn to aid the eye..... 82

Figure 3.2.8(A): Example of a Tafel plot for Electrode A prepared from the data in Fig. 3.2.7(A). The error bars represent the 95 % C.I. The dashed line is drawn to aid the eye..... 83

Figure 3.2.8(B): Example of a Tafel plot for Electrode B prepared from the data in Fig. 3.2.7(B). The error bars represent the 95 % C.I. The dashed line is drawn to aid the eye..... 84

Figure 3.2.8(C): Example of a Tafel plot for Electrode C prepared from the data in Fig. 3.2.7(C). The error bars represent the 95 % C.I. The dashed line is drawn to aid the eye..... 85

| | |
|---|-----|
| Figure 3.2.9(A): Example of a Tafel plot for Electrode A prepared from data recorded in the 54 m/o ionic liquid..... | 86 |
| Figure 3.2.9(B): Example of a Tafel plot for Electrode B prepared from data recorded in the 54 m/o ionic liquid..... | 87 |
| Figure 3.2.9(C): Example of a Tafel plot for Electrode C prepared from data recorded in the 54 m/o ionic liquid..... | 88 |
| Figure 3.2.10: Example of Arrhenius plots for (●) Electrode A, (■) Electrode B, and (▲) Electrode C prepared from data recorded in the 54 m/o ionic liquid..... | 91 |
| Figure 3.3.1: Nernst plot for the $\text{Cu}^+ + \text{e}^- \leftrightarrow \text{Cu}$ reaction in the 60 m/o $\text{AlCl}_3\text{-EtMeImCl}$ ionic liquid..... | 95 |
| Figure 3.3.2: Current-time plots recorded during the anodization of Cu rotating disk electrode at different anodic overpotentials in the 60 m/o ionic liquid: (a) 0.8 V, (b) 0.9 V, (c) 1.0 V, (d) 1.1 V, (e) 1.2 V, (f) 1.3 V, (g) 1.4 V, (h) 1.5 V, (i) 1.6 V and (j) 1.7 V..... | 96 |
| Figure 3.3.3: Example of a Tafel plot prepared from the data in Fig. 3.3.2..... | 97 |
| Figure 3.3.4: Examples of Levich plots for the anodization of a Cu RDE at 32°C in the 60 m/o ionic liquid..... | 99 |
| Figure 3.3.5: Examples of Koutecky-Levich plots, constructed from the data in Fig. 3.3.4: The anodic overpotentials were the same as those given in the previous figure. The dashed lines are drawn to aid the eye..... | 100 |
| Figure 3.3.6: Tafel plots resulting from experiments conducted at different Cu^+ concentrations..... | 103 |

| | |
|---|-----|
| Figure 3.3.7: Arrhenius plot for the exchange current density referenced to the equilibrium potential..... | 104 |
| Figure 3.3.8: Cyclic voltammogram recorded at a Pt electrode at 30 °C in 44 m/o AlCl ₃ -EtMeImCl containing 25 mmol L ⁻¹ Cu(I)..... | 105 |
| Figure 3.3.9: Current-time plots recorded during the anodization of Cu RDE at different applied potentials: (a) 0.1, (b) 0.2, (c) 0.3, (d) 0.4, (e) 0.5, (f) 0.6, (g) 0.7, (h) 0.8 V, (i) 1.0 V, (j) 1.1 V and (k) 1.2 V. AlCl ₃ -EtMeImCl solution containing 75 mmol L ⁻¹ Cl ⁻ at 30°C..... | 106 |
| Figure 3.3.10: Current-potential plots constructed from data in the previous figure at 60 s. | 107 |
| Figure 3.3.11: Examples of Levich plots for the anodization of a Cu RDE at 32°C in the ionic liquid containing 75 mmol L ⁻¹ Cl ⁻ . The anodic overpotentials were: (●) 0.17 V, (■) 0.21 V, (▲) 0.25 V, (◆) 0.29 V, (▼) 0.33 V, (○) 0.37 V, (□) 0.41 V, and (△) 0.45 V..... | 111 |
| Figure 3.3.12: Examples of Koutecky-Levich plots for the anodization of Cu Electrodes at 32°C in the ionic liquid containing 75mmol L ⁻¹ Cl ⁻ . The anodic overpotentials were: (●) 0.17 V, (■) 0.21 V, (▲) 0.25 V, (◆) 0.29 V, (▼) 0.33 V, (○) 0.37 V, (□) 0.41 V, and (△) 0.45 V..... | 112 |
| Figure 3.3.13: Log- log plot of $\partial j^{-1} / \partial \omega^{-1/2}$ versus the Cl ⁻ concentration at 30 °C, $\eta = 0.17$ V.. | 113 |
| Figure 3.3.14: Examples of Tafel plots recorded at a Cu RDE prepared from the data in Fig. 3.3.12. The error bars represent the 95 % C.I..... | 114 |

CHAPTER 1

INTRODUCTION

1.1 History of Haloaluminate Molten Salts and Ionic Liquids

Because of their high conductivity, excellent electrochemical stability, and relatively low cost, inorganic chloroaluminate molten salts are of interest for use as electrolytes for secondary batteries and for the high-rate plating of aluminium. Aluminium deposition was first investigated from the inorganic $\text{AlCl}_3\text{-NaCl}$ molten salt in the early 1930s.^{1,2} Unfortunately, typical low-melting Lewis acidic inorganic chloroaluminate molten salts such as the $\text{AlCl}_3\text{-NaCl}$ (60.0-40.0 m/o, m.p. = 113.2 °C) eutectic mixture are problematic because of the loss of volatile AlCl_3 (actually Al_2Cl_6) from open cells, which restricts their use to sealed systems. Furthermore, although the most common Lewis neutral chloroaluminate salts, e.g., $\text{AlCl}_3\text{-NaCl}$ (50-50 m/o) or $\text{AlCl}_3\text{-KCl}$ (50-50 m/o), show low vapor pressure, they exhibit high melting points, typically 157 and 250 °C, respectively.¹¹ A short review of these molten salt systems has been published.¹² Hjuler et al.¹³ have described a complex mixture of the inorganic compounds, AlBr_3 , AlCl_3 , KBr , LiCl , and NaCl that are combined in the proportions needed to prepare a molten salt with the formal composition $\text{LiAlBr}_4\text{-NaAlCl}_4\text{-KAlCl}_4$ (30-50-20 m/o) [or alternately $\text{LiAlCl}_4\text{-NaAlCl}_4\text{-NaAlBr}_4\text{-KAlCl}_4$ (30-20-30-20 m/o)], which has a melting point of only 86 °C and an electrochemical potential window of approximately 2.0 V at 100 °C. This salt was originally formulated for use as an electrolyte for rechargeable Al/molten salt/ Ni_3S_2 batteries. In contrast

to the Lewis-neutral NaAlCl_4 molten salt, it was observed that Al could be readily plated from this mixed-halide melt. A novel aspect of this molten salt is that it is a completely inorganic system, but exhibits a melting point within the range now commonly reserved for organic salt-based ionic liquids discussed below. This molten salt may prove to have many useful applications.

Although the melting point of the aforementioned molten salt is lower than most traditional inorganic molten salt systems, it is still fairly high. Scientists have also discovered aluminium chloride-based molten salts, which can be used under or close to room temperature. In the 1950s, Hurley and Wier¹⁴ proposed a room temperature molten salt, aluminium chloride-ethylpyridinium bromide. The melting point could be as low as $-40\text{ }^\circ\text{C}$ for mixtures containing 67 mole percent (m/o) AlCl_3 . These salts were formulated for the specific purpose of electroplating aluminium. (By universal consensus, these and all related low-melting molten salts are now called “ionic liquids” if they melt at less than $100\text{ }^\circ\text{C}$). In the late 1970s, Gale and Osteryoung¹⁵ carried out research on the corresponding chloride-based pyridinium molten salts. Although the elimination of bromide improved the photostability of these liquids, the Lewis basic (<50 m/o AlCl_3) ionic liquids are easily reduced by aluminium metal to the corresponding viologen. For example, when aluminium is added to the basic AlCl_3 -1-(1-butyl)pyridinium chloride ionic liquid, the beautiful, purple-colored 1,1'-dibutyl-4,4'-bipyridinium ion results. This chemistry also narrows the cathodic electrochemical window of this ionic solvent,¹⁶ limiting its use in many applications. In 1982, Wilkes and co-workers¹⁷ reported what has proven to be the most successful and enduring class ionic liquids, the aluminium chloride-1-3-dialkylimidazolium chlorides, especially AlCl_3 -1-ethyl-3-methylimidazolium chloride (EtMeImCl). The physical properties of this class of ionic liquids are superior to those based on

the 1-alkylpyridinium chloride systems, and they do not seem to react with aluminium. These ionic liquids are still in use today and are part of the subject of this dissertation.

A powerful advantage of all chloroaluminate molten salts is their Lewis acid-base behavior, which depends only on the ratio of AlCl_3 to the chloride salt, RCl . R^+ is usually either a quaternary organic salt, e.g., EtMeImCl , or an alkali chloride salt. Just as hydrogen ions control the acidity and electrochemistry of aqueous solutions in the Bronsted acid-base system, the chloride ion concentration controls the Lewis chloroacidity, which defines the electrochemistry in these ionic liquids as a result of the autosolvolysis reaction shown below. For example, compare the Bronsted and Lewis acid-base reactions in Eq. 1.1.1 and 1.1.2.



In the latter reaction, the coordinately unsaturated species, Al_2Cl_7^- , is a Lewis acid and Cl^- is a Lewis base.¹⁸ The equilibrium constant, K_{eq} , for this reaction depends on the nature of RCl and the temperature. For the AlCl_3 - EtMeImCl ionic liquid, where $\text{R}^+ = \text{EtMeIm}^+$, $K_{\text{eq}} \sim 10^{-18}$ at 40 °C,¹⁹ indicating that the equilibrium lies far to the left. The concentration of the Al_2Cl_7^- species increases as the mole fraction of AlCl_3 increases beyond 0.50, and the ionic liquid becomes more acidic. Likewise, when the mole fraction of AlCl_3 is smaller than 0.50, the molten salt contains unbound Cl^- ion and is designated as Lewis basic.

Not unexpectedly, different compositions of chloroaluminate ionic liquids and molten salts exhibit different electrochemical windows.¹⁸ The neutral melt ($x_{\text{Al}} = 0.50$) possesses the widest window, which extends from -2.0 V to 2.5 V. For the anodic reaction, if an aluminium electrode is used, Eq. 1.1.3 describes the reaction. If an inert electrode such as platinum or glassy carbon is used, the reaction proceeds according to Eq. 1.1.4. In a basic ionic liquid, Eq. 1.1.5 describes the limiting anode reaction. The expected cathodic reactions also differ by composition. These reactions decide the negative limit of the salt system. If the ionic liquid or molten salt is Lewis acidic, Al can be plated according to Eq. 1.1.6. However, the identity of the cation determines the cathodic reaction in the neutral and basic liquids. For ionic liquids based on quaternary organic cations, this reaction involves reduction of the organic cation, sometimes giving brilliant orange-colored solutions. However, in neutral or basic chloroaluminate molten salts where the organic cation is derived from an alkali chloride salt, most often NaCl, KCl, or LiCl or a combination thereof, the cathode reaction will follow Eq. 1.1.8. Thus, Al can be electroplated from both acidic and basic inorganic chloroaluminate molten salts, but not organic salt-based ionic liquids.





With the wide composition range available to ionic liquids, the dissolution process can be studied under different Lewis acidities. This is more difficult to achieve in high-melting chloroaluminate molten salts because the strong alkali cation polarizabilities promote an additional equilibrium reaction parallel to Eq. 1.1.2



with K_{eq} of about 10^{-7} for both reactions at 175 °C in the AlCl_3 - NaCl system.²⁰ Because Al_2Cl_6 has a high vapor pressure, the second reaction guarantees a small, but persistent vapor pressure of $\text{Al}_2\text{Cl}_6(\text{g})$ or $\text{AlCl}_3(\text{g})$ above the molten salt, greatly increasing experimental difficulties.

1.2 Dissolution of Al in Inorganic Chloroaluminate Molten Salts

The continuous electrodeposition or electroplating of aluminum from an aluminum-based electrolyte or molten salt requires an anode to resupply the aluminum species that is reduced at

the cathode and lost from the electrolyte during the plating process. Much research has been directed at the electrodeposition mechanism or plating reaction at the cathode in various chloroaluminate molten salts and ionic liquids (and numerous reviews are available), but little attention has been directed at the reactions taking place at the anode. It is usually assumed that any current limitations that are encountered can be overcome by using an anode with a suitably large surface area. This may be feasible in large volume plating baths, but in Al-based batteries with confined anodes, this could be problematic.

One of the earliest investigations of aluminum anodization in haloaluminates was carried out by Del Duca²¹ in $\text{AlCl}_3\text{-NaCl}$ (50-50 m/o) and $\text{AlCl}_3\text{-LiCl-KCl}$ (50.0-20.5-29.5 m/o). In this work, transient galvanostatic techniques were used to investigate the kinetics of this reaction over the temperature range from 175 to 313 °C. These results were subsequently criticized for their failure to take into account the propensity of Al to form surface oxides and the lack of electrode surface preparation, which were believed to greatly affect the results.²² Li and Bjerrum²³ discussed problems related to the activation of aluminum anodes in haloaluminate molten salts as a result of this oxide layer. Using a different approach, Holleck and Giner,¹ employed rotating disk electrode voltammetry to examine the anodization of Al in $\text{AlCl}_3\text{-KCl-NaCl}$ mixtures containing > 50 m/o AlCl_3 (Lewis acidic mixtures). Because these experiments involve significant currents under forced convection conditions, extant surface oxide films will be removed quickly as the Al undergoes anodic dissolution. Passivation of the Al-RDE was noted in these experiments, and the exchange current for the Al dissolution process was measured with a transient technique. Finally, there have been reports in the early literature that the anodization of Al in $\text{AlCl}_3\text{-NaCl}$ molten salts produces subvalent species. However, Gale

and Osteryoung²⁴ showed that these findings likely resulted from the corrosion of Al by adventitious impurities in the melts.

From an environmental perspective, haloaluminate molten salts/ionic liquids are relatively benign compared to those pyrophoric materials currently used for the commercial plating of aluminum, which are typically composed of mixtures of alkylaluminum compounds and alkali salts dissolved in toluene.²⁵ These environmental concerns have sparked a renewed and growing interest in the use of haloaluminate molten salts/ionic liquids as Al plating baths with the main interest directed at low-melting systems. Thus, as recently noted, information about the mechanism associated with the Al anode is crucial to the development of an efficient commercial plating process based on these ionic solvents.²⁶ In addition, an understanding of the Al anodization mechanism and the various factors that affect the anodization rate is crucial to the development of industrial processes for the electrochemical machining and electropolishing of Al in haloaluminate molten salts/ionic liquids.

As noted above, with the exception of the early work by Holleck and Giner¹, virtually nothing is known about the anodization of Al in haloaluminate molten salts, including the kinetics of this process and the role of passivation. Thus, in seeking a “model” alkali halide-based haloaluminate salt for the study of Al anodization, we have employed the low-melting $\text{LiAlBr}_4\text{-NaAlCl}_4\text{-KAlCl}_4$ (30-50-20 m/o) system. We have chosen this molten salt because of its high conductivity, low melting point and negligible vapor pressure. Using this ionic solvent, we have developed a reliable procedure for investigating the Al anodization process. In addition, we report the density and viscosity of this molten salt as an adjunct to the electrical conductivity data given by Hjuler et al.¹³ and compare these results to those for some other molten salts and ionic liquids.

1.3 Dissolution of Al in Organic Chloroaluminate Ionic Liquids

Room-temperature chloroaluminate ionic liquids are obtained by combining aluminum chloride with certain anhydrous quaternary ammonium chloride salts. The most popular examples of these well-known salts are those based on the 1,3-dialkylimidazolium cations, notably 1-ethyl-3-methylimidazolium chloride (EtMeImCl).¹⁷ A unique and very versatile feature of these ionic liquids is their adjustable chloroacidity, which is based on the extant anions. This property is directly tied to the AlCl₃ content and is commonly expressed as the AlCl₃/organic chloride salt ratio, mol fraction of AlCl₃ (x_{Al}), or percent mol fraction (m/o) of AlCl₃. In this article, all compositions will be reported using the latter two conventions. Mixtures that contain less than 50 m/o AlCl₃ ($x_{Al} < 0.50$) are Lewis basic by virtue of excess unbound chloride ion, whereas those containing greater than 50 m/o AlCl₃ ($x_{Al} > 0.50$) are Lewis acidic because they contain the coordinately unsaturated species, Al₂Cl₇⁻. Equimolar mixtures of the organic salt and AlCl₃ ($x_{Al} = 0.50$) contain only AlCl₄⁻ and are designated as “neutral” ionic liquids.

Acidic room-temperature chloroaluminates are of interest as solvents for the electroplating of aluminum and aluminum alloys due to the easily accessible redox reaction²⁷



It is also possible to electrochemically reduce the coordinately saturated species, AlCl₄⁻, but this reaction is normally accessible only in alkali chloride-based systems such as AlCl₃-NaCl where this anion can be reduced at more positive potentials than the alkali cation. However, this does

not seem to be the case in chloroaluminates based on organic cations. Room-temperature chloroaluminates are safer, less problematic alternatives to the traditional plating baths based on mixtures of aromatic hydrocarbons, alkali halide salts, and pyrophoric aluminum alkyl compounds commonly used in commercial Al plating technology. In fact, BASF now supplies the 60 m/o AlCl_3 -EtMeImCl ionic liquid for this purpose (Basionic™ AL 01) along with suitable beneficial additives to improve deposit morphology. The high-rate electroplating of aluminum from room-temperature chloroaluminate ionic liquids and traditional plating baths has been comprehensively reviewed^{26,28} with practical comparisons of the plated products obtained from engineering studies using different plating baths²⁵ and will not be discussed further herein.

There have been a number of investigations of Al anodization or the anodic dissolution of bulk Al in Lewis acidic chloroaluminate/haloaluminate molten salts, including AlCl_3 -NaCl and related alkali chloride systems.^{1,21,22,24,27-29} But only few such investigations have been undertaken in the related room-temperature ionic liquids, e.g., AlCl_3 -EtMeImCl³⁰ and AlCl_3 -BuMeImCl,²⁴ with the former study conducted in the basic (Cl^- -rich) ionic liquid. However, the kinetics and mechanistic aspects of the anodization reaction are far from settled. Historical reports seem to conflict with some investigators observing classical Tafel behavior.²¹ Others have reported the formation of a passive layer of $\text{AlCl}_3(\text{s})$, which results in a limiting current governed by the diffusion of reacting ions to the electrode surface.¹

In a recent article,³¹ we reported the anodic dissolution of Al in the Lewis neutral LiAlBr_4 - NaAlCl_4 - KAlCl_4 (30-50-20 m/o) haloaluminate molten salt as a function of temperature. This investigation was carried out by using rotating disk electrode voltammetry at a miniature Al electrode.³¹ In this case, both types of behavior described above were observed. For example, at small overpotentials, the Al dissolution process proceeds under mixed kinetic/mass-transport

control, but at higher dissolution rates, the current decreases significantly due to the formation of a passive/blocking layer of $\text{AlCl}_3(\text{s})$, and the current becomes mass-transport limited.

In this investigation, we have examined the anodic dissolution of Al in Lewis acidic $\text{AlCl}_3\text{-EtMeImCl}$ as a function of the ionic liquid composition using the same experimental procedures. It was not possible to examine the composition dependence of this reaction during our previous investigation due to experimental limitations inherent to working with the higher-melting acidic $\text{LiAlBr}_4\text{-NaAlCl}_4\text{-KAlCl}_4$ molten salt. However, there are no such limitations in the $\text{AlCl}_3\text{-EtMeImCl}$ system. In addition, we carried out experiments on polycrystalline Al samples of varying conformation that have undergone different processing conditions in order to assess whether the structural differences of these materials is reflected by their different dissolution rates.

1.4 Dissolution of Copper

As mentioned above in the Rationale, electrochemical machining (ECM) and electropolishing are invaluable for the modification of different metals. Among the metals of interest, copper draws great attention because of its high thermal and electrical conductivity; it is a good conductive material that can be used for heat transfer and electrical purposes; and is a constituent of various important metal alloys, such as brass and bronze. As noted many times above, because of their adjustable chloroacidity, chloroaluminate ionic liquids offer a unique solvation environment for many metals. On the one hand, basic $\text{AlCl}_3\text{-EtMeImCl}$ provides a solvation environment that is not unlike aqueous NaCl , except without the H_2O . The Lewis acidic ionic liquid is, however, a very different story because there are no “hard” ligands

available to form stable anionic complexes with the anodization product, which at small potentials is known to be Cu^+ . In fact the opposite situation prevails wherein the main ionic component of the solvent is actually a coordinately unsaturated electron deficient species. There are no reports of studies about the anodic dissolution of copper in chloroaluminate salts. However, investigations describing the anodic dissolution of copper in aqueous systems and deep eutectic solvents²⁶ abound, with some of the first reports appearing as early as the 1950s.³² Foremost among this work is that of Ken Nobe at UCLA in the 1980s.^{33,34} Nobe's group studied the anodic polarization behavior of Cu in Bronsted acidic chloride solvents. His group pointed out that when the applied potential is sufficient to reach the limiting current, the reaction is under mass-transfer control, which is governed by the formation and solvation of the cuprous chloride complex, CuCl_2^- . Based on the model that Nobe proposed, which assumes the formation of a thin film of CuCl on the electrode surface and a rate determining step involving the diffusion of the chloride ions, they were able to calculate kinetic data in the acidic aqueous chloride solutions. Three possible mechanisms leading to this result are shown below³⁵

Mechanism 1



Mechanism 2



Mechanism 3



As the amount of CuCl_2^- in the solution increases, the Cu^+ precipitates as Cu_2O



The equilibrium constant for this reaction is $\sim 10^{20}$, which guarantees the precipitation of Cu_2O . Of course, in the water-free environment afforded by chloroaluminate ionic liquids, the reaction given by Eq. 1.4.6 is impossible because there is no oxide or hydroxide source. Depending on which reaction is chosen as the rate-determining step in each mechanism, it may

be possible to use classical Tafel analysis to elucidate which of these mechanisms relates to the oxidation of Cu in basic $\text{AlCl}_3\text{-EtMeImCl}$. Based on the papers by Brossard³⁶ and Faita³⁷, if the first mechanism is the oxidation of Cu in the ionic liquid, which represents the direct formation of CuCl_2^- , the following Nernst equation is applicable.

$$E_{eq} = E^{0'} + \frac{RT}{F} \ln \frac{[\text{CuCl}_2^-]}{[\text{Cl}^-]^2} \quad [1.4.7]$$

According to Fick's first law,³⁸ the current for the oxidation of copper is:

$$j = \frac{FD_{\text{CuCl}_2^-}}{1.61D_{\text{CuCl}_2^-}^{1/3} \nu^{1/6} \omega^{-1/2}} \quad [1.4.8]$$

By combining Eq. 1.4.7 and 1.4.8, Eq. 1.4.9 is

$$j = 0.62D_{\text{CuCl}_2^-}^{2/3} \nu^{1/6} \omega^{-1/2} [\text{Cl}^-]^2 \exp \frac{F(E_{eq} - E^0)}{RT} \quad [1.4.9]$$

From Eq. 1.4.9, we can derive the following relationships:

$$\left(\frac{\partial E_{eq}}{\partial \log j} \right)_{298K} = 59 \text{ mV/decade} \quad [1.4.10]$$

$$\left(\frac{\partial j}{\partial \omega^{1/2}} \right) = \text{constant} \quad [1.4.11]$$

$$\left(\frac{\partial E_{\text{eq}}}{\partial \log\left(\frac{\partial j}{\partial \omega^{1/2}}\right)} \right)_{298K} = 59 \text{ mV/decade} \quad [1.4.12]$$

The mechanism can be tested by plotting three graphs, which are E_{eq} versus $\log j$, j versus $\omega^{1/2}$, and E_{eq} versus $\log(j\omega^{-1/2})$. If the results match the relationships above, that means that mechanism 1 can be applied to the anodization of copper in the basic ionic liquid.

Schifferin^{39,40} derived the Koutecky-Levich equation for the second mechanism thought to govern the oxidation of copper in basic solutions. This equation is very close to the K-L equation used in the acid solution, as shown below:

$$\frac{1}{j} = \frac{1}{nFk_a} + \frac{1.61 k_c D_{\text{Cu}^+}^{-2/3}}{nFk_a \nu^{-1/6}} \frac{1}{\omega^{1/2}} \quad [1.4.13]$$

This means the slope of the i^{-1} vs $\omega^{-1/2}$ plot should be proportional to the ratio of k_c/k_a , which is shown in Eq. 1.4.14

$$\frac{k_c}{k_a} = \exp^{-n(E_{\text{eq}} - E^0)f} \quad [1.4.14]$$

where $f = RT/F$. Therefore, the following relationship is obtained,

$$\frac{\partial \log(\partial j^{-1} / \partial \omega^{-1/2})}{\partial E_{\text{eq}}} = -nF/2.3RT \quad [1.4.15]$$

In this case, Mechanism 2 can be tested by plotting the slope of the j^{-1} versus $\omega^{-1/2}$ plot versus E_{eq} .

If the results match Eq. 1.4.15, then Mechanism 2 might represent the anodization of copper in the ionic liquid.

The papers that support the third mechanism, which are published by Nobe,³⁴ Crundwell,⁴¹ and Tribollet⁴² introduced the derivation of the rate equation for the Cu electrode anodization. The final, simplified Koutecky-Levich equation is shown below:

$$\frac{1}{i} = \frac{1}{FAK_0C_{Cl^{-2}}} + \frac{1.61 k_{-2}}{FAD_{CuCl_2}^{-2/3} \nu^{-1/6} K_0 C_{Cl^{-2}}} \frac{1}{\omega^{1/2}} \quad [1.4.16]$$

where $K_0 = \frac{k_1 k_2}{k_{-1}} \exp(FE_{eq}/RT)$, and k_1 and k_2 stand for the rate constants of the forward reaction of the first and second steps of the mechanism, and k_{-1} and k_{-2} stand for the back reactions, respectively. Based on Eq. 1.4.16, the slope of a plot of j^{-1} vs $\omega^{-1/2}$ is proportional to $C_{Cl^{-2}}$. This suggests that if we plot $\log j^{-1}/\omega^{-1/2}$ vs the $\log C_{Cl^{-}}$, the slope should be 2. If that applies to the Cu anodization reaction of the ionic liquid, we can assume that the oxidation of Cu is described by Mechanism 3.

1.5 Techniques for the Investigation of Electrode Reactions

In terms of electrochemistry, the simplest possible reaction is $O + ne^- \leftrightarrow R$, where both O, the oxidized species, and R, the reduced species are soluble in the electrolyte. O and R can be metal ions, as well as dissolved organic or inorganic metallic species. This type of reaction is typically investigated in an electrochemical cell, which is equipped with working, counter and reference electrodes (sometimes the counter electrode can also serve as the reference electrode too). In our lab, we employ a classic three electrode cell as shown below in Fig. 1.5.1 to study

molten salts and ionic liquids. A is the thermocouple to monitor temperature, B is the reference electrode or reference half-cell, C is the working electrode, D is the counter electrode, and E is an electrical resistance furnace.

If both O and R are present in the solution, the working electrode will reach its equilibrium potential, E_{eq} , versus the reference half-cell if no external potential is applied. This potential is given by the familiar Nernst equation:

$$E_{eq} = E^{0'} + \frac{RT}{nF} \ln \frac{C_O^*}{C_R^*} \quad [1.5.1]$$

where $E^{0'}$ is the thermodynamic standard (or formal) electrode potential of the O/R half-cell reaction, and C_O^* and C_R^* are the bulk concentrations of O and R, respectively. It is important to know that this relationship actually reflects the potential of the O/R half-cell electrode versus a particular reference electrode. In water, the NHE or normal hydrogen electrode ($E^0 = 0$ V) is the standard of choice for all half-cell reactions, but it is experimentally impractical. However, there are many other reference electrodes besides the NHE for use in water, including the calomel electrode (SCE) and the silver/silver chloride electrode (SSC). We will not discuss these further here because they are of little value as reference electrodes in molten salts and ionic liquids. The reference electrodes for use in these electrolytes are chosen on a case-by-case basis depending on the ionic liquid. Once a reliable reference has been established, the cell potential, E_{cell} , can be calculated by using the relationship $E_{cell} = E_{eq} - E_{ref}$. Once the E_{cell} is known, the electrochemical reaction can be controlled by applying a potential either more positive or more negative than E_{cell} , which will cause the oxidation of R or reduction of O, respectively.

The reaction discussed above is the simplest case. For the experiments we report herein, R is a metal, and O is the oxidation product of the metal. Furthermore, anodization of the metal will be the main reaction, $M \leftrightarrow M^{n+} + ne^-$. Thus, the concentration of the R species, which is the metal, can be assigned unit activity or $C_M = 1$. Another fact that needs to be pointed out is that the $E^{0'}$ of this electrode is based on the reduction reaction, $M^{n+} + ne^- \leftrightarrow M$. Therefore, the equilibrium potential, E_{eq} , will be

$$E_{eq} = E^{0'} + \frac{RT}{nF} \ln C_{M^{n+}}^* \quad [1.5.2]$$

where $C_{M^{n+}}^*$ is the bulk concentration of M^{n+} in the electrolyte.

There are many electrochemical techniques commonly used to analyze how an electrode reaction behaves, i.e., to study the kinetics and thermodynamics of electrode reactions. In this study of metal anodization, Rotating Disk Electrode Voltammetry (RDEV), Chronoamperometry (CA), and Electrochemical Impedance Spectroscopy (EIS) will be the main techniques employed. These techniques are briefly summarized below.

1.5.1 Rotating Disk Electrode Voltammetry

The rotating disk electrode or RDE is widely used to perform many types of electrochemical measurements, usually under controlled potential or potential conditions, because it allows controlled convective mass transport of the reactants and products. It is usually made of a conductive metal disk (Al and Cu in our case) shrouded with an inert, non-conductive

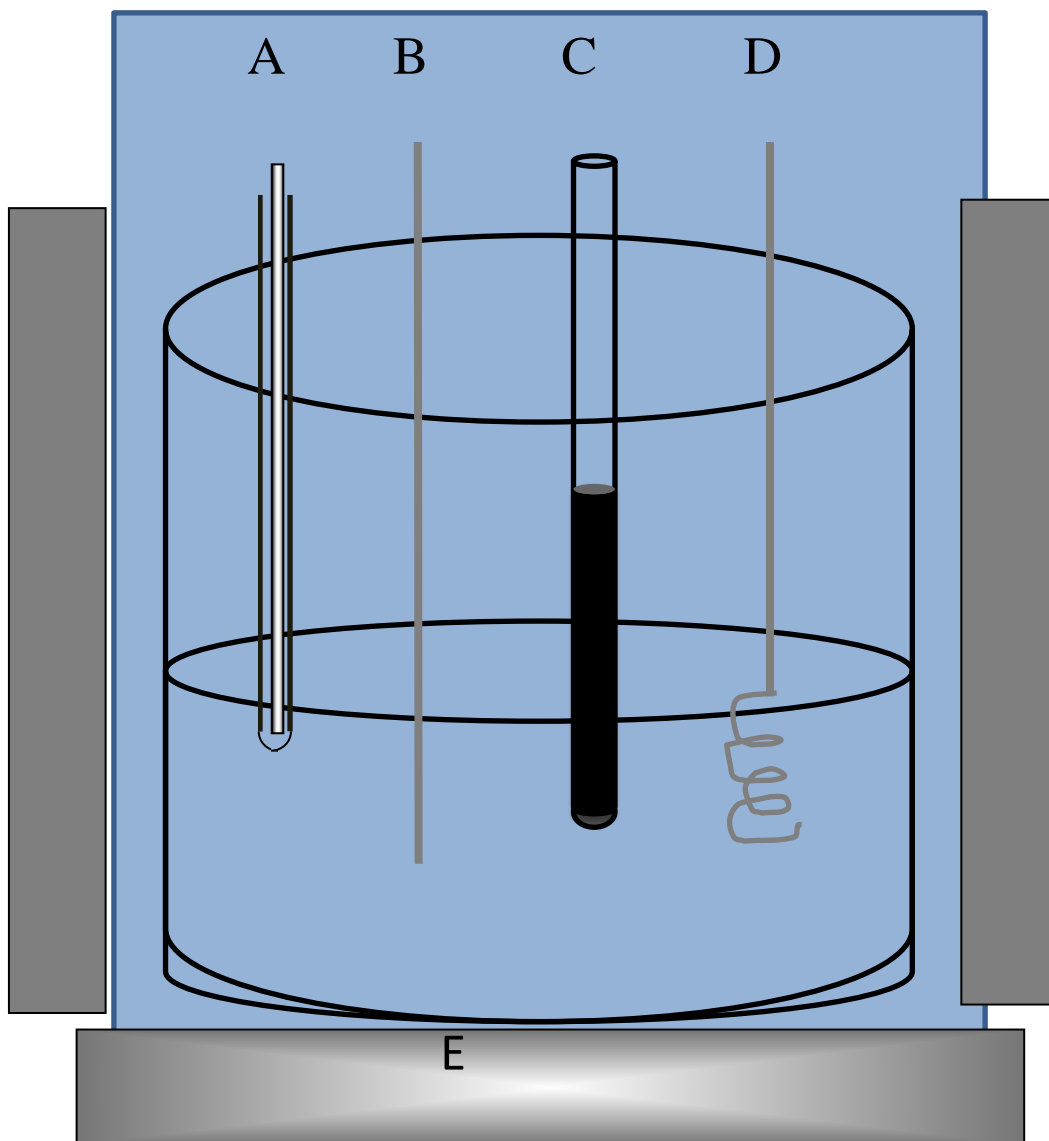


Figure 1.5.1: A classic three electrode cell.

material (polymer, resin, ceramic). Precise rotation is provided by a separate motor-driven electrode rotator.

As shown in Fig. 1.5.2 below, when the electrode spins, the centrifugal force drags the electrolyte fluid at its surface and flings the fluid away from the center of the electrode at the same time. Once the reaction starts after the application of a suitable potential to cause O to be reduced to R, the concentration of the O species at the electrode surface, $C_O(y = 0)$, will be smaller than that in the bulk solution, C_O^* , as noted in Fig. 1.5.3 for E_1 . If the potential is sufficiently negative of E_{cell} , $C_O(y = 0)$ can be driven to zero, and the concentration profile below will be obtained as depicted in Fig. 1.5.3 for E_2 . This establishes a diffusion layer, δ_O , for O and δ_R , for R, respectively, as shown in Fig. 1.5.3. Note that $E_1 > E_2$. The dashed line indicates the approximate thickness of δ_O and δ_R , which are determined by the electrode rotational frequency, ω . Note that the diffusion layer thickness is not proportional to the applied potential. The potential only affects $C_O(y = 0)$, and the thickness is proportional to ω ,

$$\delta_i = 1.61 D_i^{1/3} \omega^{-1/2} \nu^{1/6} \quad [1.5.3]$$

where D_i is the diffusion coefficient of either O or R, and ν is the kinematic viscosity of the electrolyte.^{43,44}

The concentration of the reactant, O, near the electrode surface, as determined by the potential, is constant. Because convective mass transport controls the thickness of δ_O and δ_R as ω is changed, a concentration gradient is established, $\partial C_O / \partial y = [C_O^* - C_O(y = 0)] / \delta_O$, that depends on ω and E . The cell current is related to $\partial C_O / \partial y$ by Eq. 1.5.4

$$i = nFAD_0 \left(\frac{\partial C_O}{\partial y} \right)_{y=0} \quad [1.5.4]$$

Defining m_0 as the mass transport coefficient, or D_0/δ_0 , where D_0 is the diffusion coefficient of O, $m_0 = 0.62 D_0^{2/3} \omega^{1/2} \nu^{-1/6}$ for the RDE.⁴⁴ Equation 1.5.4 can be rewritten as

$$i = nFAm_0 [C_O^* - C_O(y=0)] \quad [1.5.5]$$

Imposing the condition that $C_O(y=0) = 0$, which is achieved by applying a suitably negative potential, the Levich equation is obtained.⁴³ This equation is shown below

$$i_l = 0.62nFAD_0^{2/3} \omega^{1/2} \nu^{-1/6} C_O^* \quad [1.5.6]$$

where i_l is the limiting current, and all other experimental variables have been defined. The Levich equation indicates that if the reaction is under mass-transport control, i_l is proportional to $\omega^{1/2}$. By using this equation, we can calculate diffusion coefficients from the limiting currents we measure. On the other hand, if D_0 is known, then we can use i_l to determine C_O^* .

Not all reactions proceed under mass transport control. In the case where the simple reduction reaction $O + ne^- \leftrightarrow R$ exhibits kinetic limitations, the equations describing the relationship between the current and the other variables must include terms that account for the kinetic rate. In this case, the net current can be written as

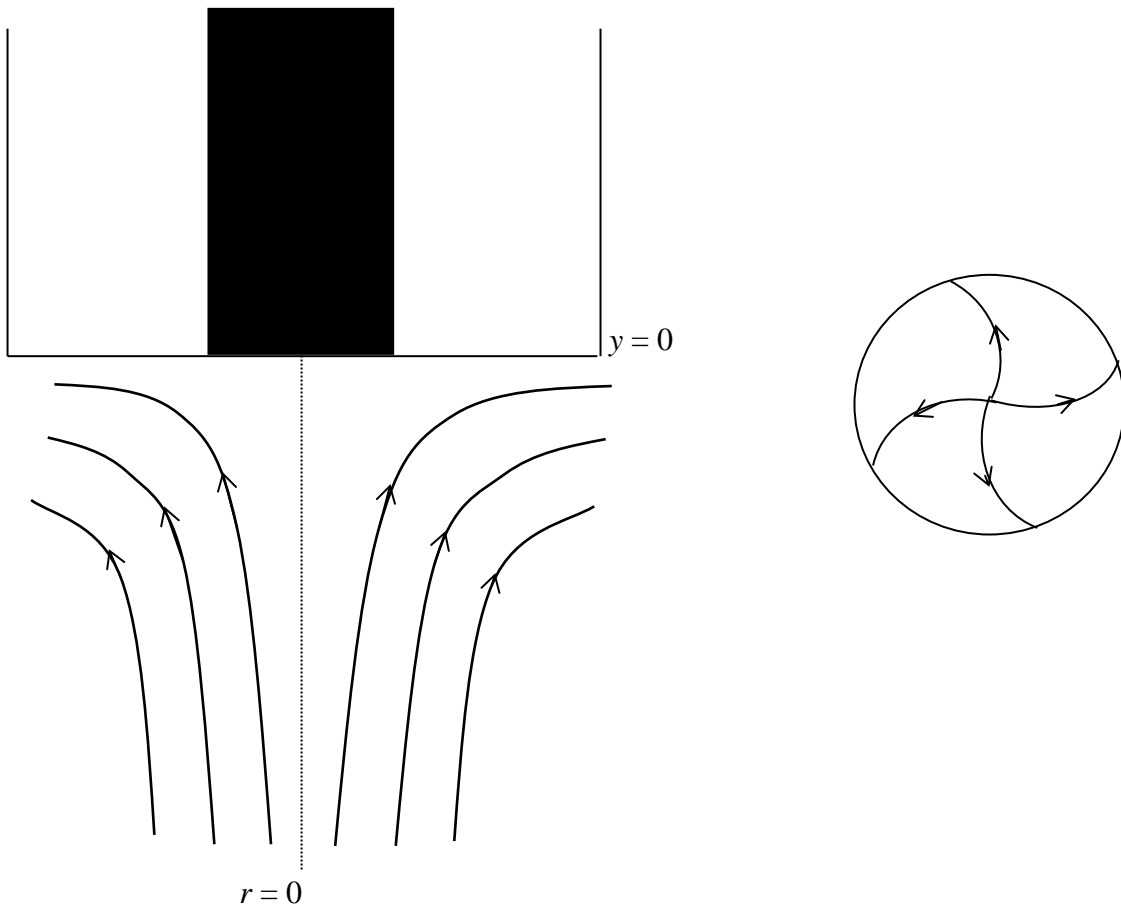


Figure 1.5.2: Representation of fluid velocities near a rotating disk electrode.

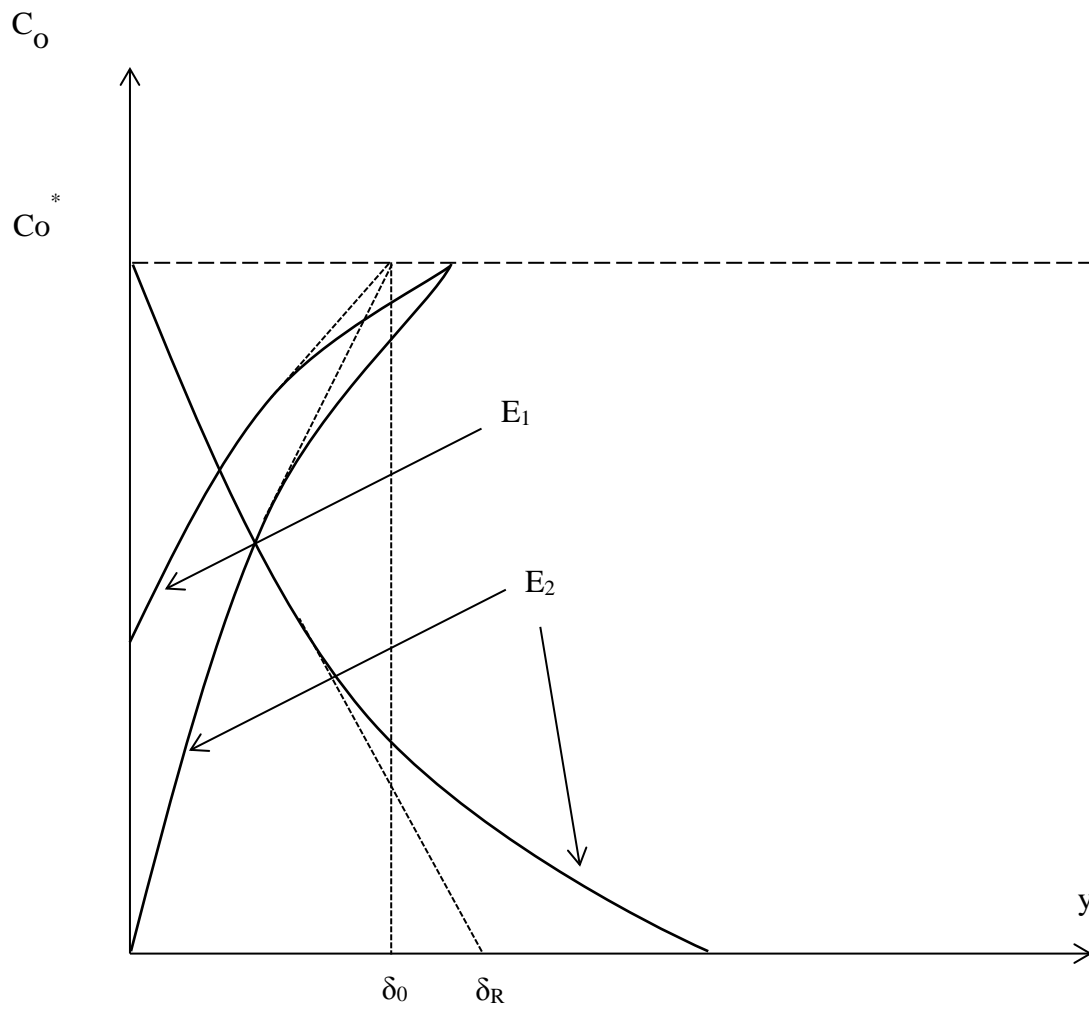


Figure 1.5.3: Concentration profiles and approximate diffusion layer thicknesses.

$$i = nFA[k_c C_O(y=0) - k_a C_R(y=0)] \quad [1.5.7]$$

where k_a and k_c are the anodic and cathodic heterogeneous rate constants with units of cm s^{-1} . The relationship between the current and surface concentration of O, is Eq. 1.5.7, and that for R, is given by Eq. 1.5.8

$$i = nFAm_R[C_R(y=0) - C_R^*] \quad [1.5.8]$$

Note that $m_R = 0.62 D_R^{2/3} \omega^{1/2} \nu^{-1/6}$. Combining Eq. 1.5.5, 1.5.7 and 1.5.8, by eliminating the surface concentrations gives, after some algebra, the Koutecky-Levich equation^{44,45} for a simple reduction reaction $O + ne^- \leftrightarrow R$ that exhibits mixed kinetic-mass transport limitations or “mixed control”⁴⁶

$$\frac{1}{i} = \frac{1}{nFA(k_c C_O^* - k_a C_R^*)} + \frac{1.61 (k_c D_R^{-2/3} + k_a D_O^{-2/3})}{nFA(k_c C_O^* - k_a C_R^*) \nu^{-1/6}} \frac{1}{\omega^{1/2}} \quad [1.5.9]$$

If the solution contains only O, i.e., $C_R^* = 0$, the back reaction can be ignored and the Koutecky-Levich equation simplifies to Eq. 1.5.10

$$\frac{1}{i} = \frac{1}{nFAk_c C_O^*} + \frac{1.61 D_O^{-2/3}}{nFAC_O^* \nu^{-1/6}} \frac{1}{\omega^{1/2}} \quad [1.5.10]$$

Note that in the Koutecky-Levich equation, the first term, which equals to $nFA(k_c C_O^* - k_a C_R^*)$, stands for the kinetic current i_k . This is the current in the absence of mass-transport effects. In other words, when the rotation rate goes to infinity, the current will be limited only by rate of charge transfer, and the second term in Eq. 1.5.9 and 1.5.10 goes to zero.

The equations shown above are based on the reaction, $O + ne^- \leftrightarrow R$. However, for the proposed experiments, the anodic dissolution of different metals will be investigated. In order to derive the equations for metal dissolution, we start from the simplest reaction, $M \leftrightarrow M^{n+} + ne^-$. In terms of this reaction, Eq. 1.5.5, 1.5.7 and 1.5.8 will become Eq. 1.5.11, 1.5.12 and 1.5.13.

$$i = nFA[k_a C_M(y=0) - k_c C_{M^{n+}}(y=0)] \quad [1.5.11]$$

$$i = nFA m_{M^{n+}} [C_{M^{n+}}(y=0) - C_{M^{n+}}^*] \quad [1.5.12]$$

$$i = nFA m_M [C_M^* - C_M(y=0)] \quad [1.5.13]$$

However, considerable simplification occurs because $C_M(y=0) = 1$ and $C_M^* = 0$. So that Eq. 1.5.11 becomes Eq. 1.5.14

$$i = nFA[k_a - k_c C_{M^{n+}}(y=0)] \quad [1.5.14]$$

and Eq. 1.5.12 becomes irrelevant. Combining Eq. 1.5.12 and 1.5.14 and noting that $m_{M^{n+}} = 0.62 D_{M^{n+}}^{2/3} \omega^{1/2} \nu^{-1/6}$, gives Eq. 1.5.15, which is the Koutecky-Levich equation for metal dissolution⁴⁷

$$\frac{1}{i} = \frac{1}{nFA(k_a - k_c C_{M^{n+}}^*)} + \frac{1.61 k_a D_{M^{n+}}^{-2/3}}{nFA(k_a - k_c C_{M^{n+}}^*) \nu^{-1/6}} \frac{1}{\omega^{1/2}} \quad [1.5.15]$$

note $nFA(k_a - k_c C_{M^{n+}}^*) = i_k$. By making a plot of $1/i$ versus $1/\omega^{1/2}$, the intercept will be the $1/i_k$ at the specified temperature and applied potential. If the solution is initially devoid of the reducible metal ions, i.e., $C_{M^{n+}}^* = 0$, then Eq. 1.5.15 simplifies further to give

$$\frac{1}{i} = \frac{1}{nFAk_a} + \frac{1.61 k_a D_{M^{n+}}^{-2/3}}{nFAk_a \nu^{-1/6}} \frac{1}{\omega^{1/2}} \quad [1.5.16]$$

Note that now $i_k = nFAk_a$. Once i_k is known as a function of potential, graphs of $\log i_k$ versus η , allow determination of the exchange current, i_0 , by extrapolation of the linear portions of these graphs to $\eta = 0$, where $\eta = E - E_{eq}$ by using the Tafel expression

$$\log i_k = \log i_0 + \alpha_a F \eta / RT \quad [1.5.17]$$

In this expression, α_a is the anodic transfer coefficient, which represents the symmetry of the anodic activation energy barrier and contains information about the rate-determining step in the electrode reaction mechanism. Examples of a typical graph with the extrapolated anodic Tafel line are shown in Fig. 1.5.4. The exchange current is another measure of kinetic facility and is given by the expression⁴⁶ $i_0 = nFAk^0 C_O^{*\alpha_a} C_R^{*\alpha_c}$. However, when the reaction is a simple metal dissolution process, the expression is greatly simplified. In this case, the exchange current is the same as i_k that is corrected for the back reaction, and in this example is also given by $nFAk_{a,0}$.

Rather than being the standard heterogeneous rate constant, k^0 at $E^{0'}$, $k_{a,0}$ is simply the rate constant at $\eta = 0$ or E_{eq} . If M^{n+} is present in the solution, this is a way to get $k_{a,0}$ by extrapolation from large positive potentials where the back reaction $M^{n+} + ne^- \leftrightarrow M$ proceeds at a negligible rate.

Collecting data at different temperatures allows determination of the activation energy, ΔG^\ddagger as well. Thus, the Koutecky-Levich equation is a powerful tool for the calculation of kinetic data from RDE results when the reaction is under mixed control.

1.5.2 Chronoamperometry

Chronoamperometry is a simple controlled-potential technique, which measures the current response resulting from a potential step in a three-electrode cell. During these measurements, a constant potential is applied to the cell for a certain time, and the total current is recorded. The relationship between the applied potential and the current simply reflects the change in the concentration gradient close to the electrode surface.

As shown in Fig. 1.5.5a, E_i is the initial potential region where there is no electrochemical reaction. It could be E_{eq} . Once a more negative potential (E_1) is applied, the reduction reaction occurs. Note that when the reaction starts, the concentrations of O and R at the surface are now different from the concentrations in the bulk solution, and a diffusion layer is formed. However, as Fig. 1.5.5b illustrates, unlike the steady-state case for the RDE, δ_O and δ_R vary with time. For a Nernstian reaction when the potential is applied the surface concentration of O (and R) changes from C_O^* instantly. If E_2 is sufficiently negative, then $C_O(x=0) = 0$. The concentration gradient caused by the initial reduction will produce continuing fluxes of O to the

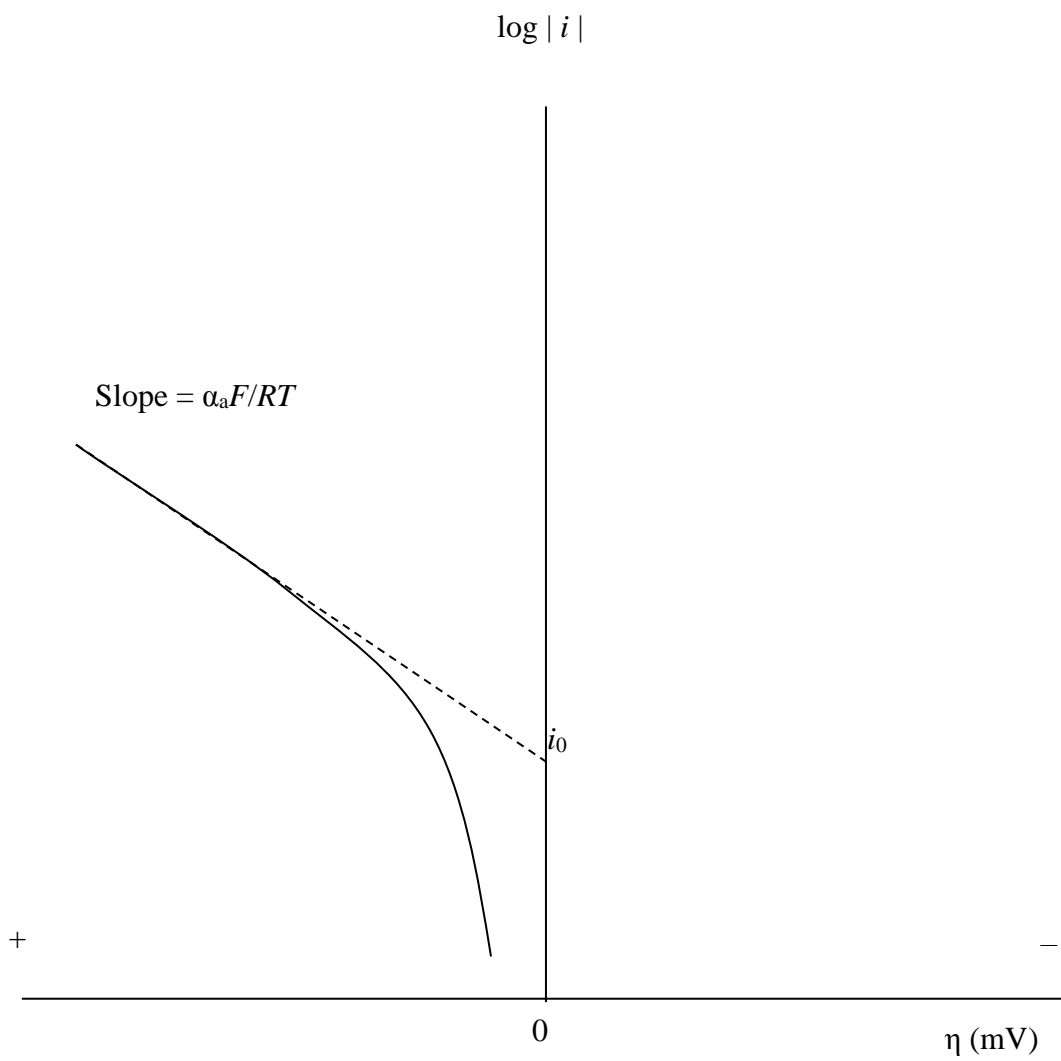


Figure 1.5.4: Example of a typical Tafel plot.

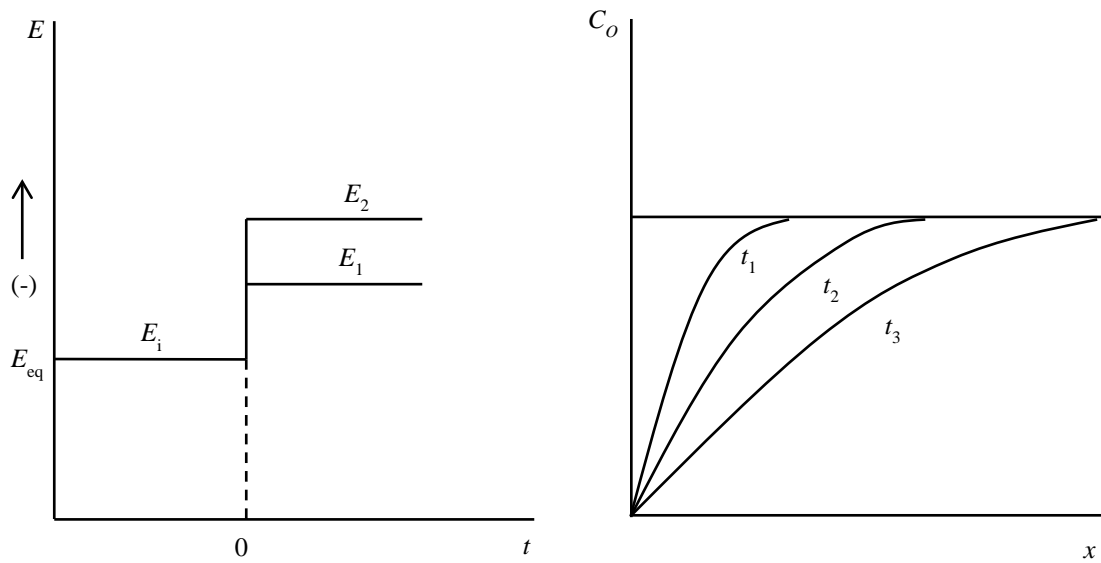
electrode surface and R away from the surface in an unstirred solution (no forced convection that diminishes with time). Therefore, the flux of O is proportional to the concentration gradient, and this is why the slope of the concentration profile declines with time, $t_3 > t_2 > t_1$. Figure 1.5.5c is the current-time response to the potential step experiment described in Fig. 1.5.5a and 1.5.5b at different E values. This current response in an unstirred solution is given by the Cottrell equation, with $C_O(x=0)$ determined by the magnitude of the applied potential.⁴⁸

$$i(t) = \frac{nFAD_O^{1/2}[C_O^* - C_O(x=0)]}{\pi^{1/2}t^{1/2}} \quad [1.5.18]$$

The current at E_2 corresponds to diffusion control, i.e., $C_O(x=0) = 0$.

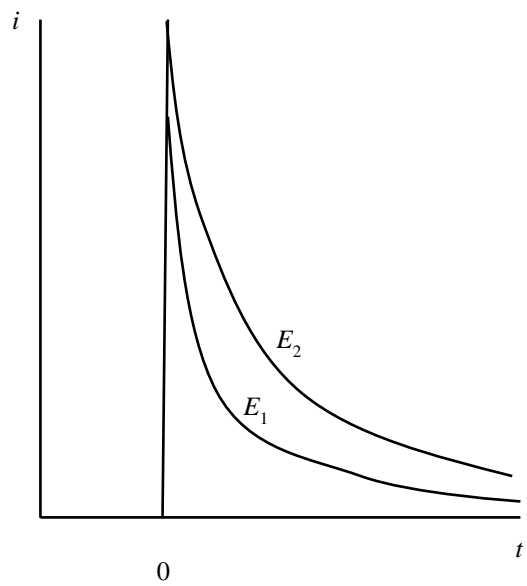
For the proposed anodization experiments, CA is used with the metal RDE at constant ω . Because the solution is stirred, the current will usually assume a constant value that depends only on the applied E . By applying several designated potentials to the metal working electrode, current-time or current density ($j = i/A$) plots or can be obtained, as shown below (Fig. 1.5.6).

This is a typical CA plot for the oxidation of a metal at the RDE and is quite different from Fig. 1.5.5c. As can be seen in the graph, the current densities increase immediately following the application of the potential step, and then decay to a steady-state value. This sharp current spike is due to the charging of the electrode double-layer. There is no diffusion-limited current for the anodic dissolution of a metal. The combination of Eq. 1.5.4 written for $x = 0$ with Eq. 1.5.5 with $C_O^* = 0$ and eliminating $C_O(x=0)$ shows that the current for metal anodization depends only on E . However, if there are complications such as passivation or the formation of a blocking surface film, the current response may not depend on E as discussed above, and the current will appear to reach a limiting value, but this is somewhat illusory.



(a)

(b)



(c)

Figure 1.5.5: (a) Waveform for a step experiment. (b) Concentration profiles for various times.

(c) Current flow versus time.

1.5.3 Electrochemical Impedance Spectroscopy

Electrochemical Impedance Spectroscopy (EIS) is an electrochemical technique that allows the study of the electron transfer kinetics of electrochemical reactions and also has many applications in the field of corrosion, particularly for the deduction of corrosion mechanisms.⁴⁹ With this technique, electrochemists try to model the cell reaction by using electrical circuit elements such as resistance or impedance, capacitance and inductance, and various combinations thereof. In EIS, a sinusoidal potential signal is used to excite the working electrode, and the impedance response of the whole electrochemical cell is measured as a function of frequency at the desired applied potential, usually E_{eq} . A classic Randles equivalent circuit model for an uncomplicated electrode reaction, such as $O + ne^- \leftrightarrow R$, is shown in the inset of Fig. 1.5.7 below.⁵⁰ The series resistor, R_{Ω} , stands for the resistance of the electrolyte, as well as the circuit wires/connections for the whole system.⁴⁶ The parallel resistance, R_{ct} , is called the charge transfer resistance. It is related to i_0 through the expression

$$R_{ct} = \frac{RT}{nFi_0} \quad [1.5.19]$$

The capacitance is a model of the response of the electrode double layer as a function of frequency, ω . However, a pure capacitor is an imperfect representation of the electrode double layer. Instead, the double layer capacitance is often modeled by a pseudocapacitance, called a constant phase element (CPE). This component includes both impedance and capacitance. The impedance, W , is called the Warburg impedance and takes into account the impedance due to diffusion, which has real and imaginary parts. W is proportional to $1/\sqrt{\omega}$.

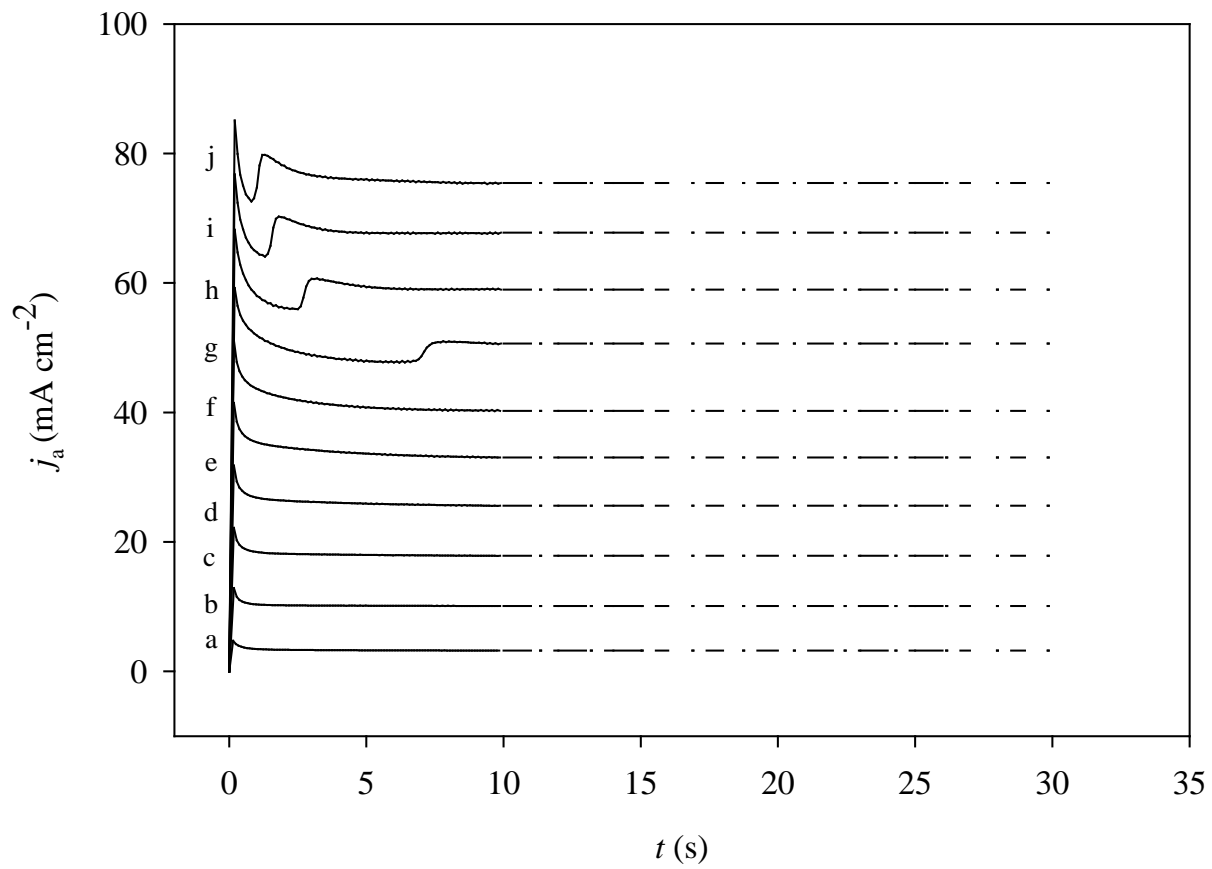


Figure 1.5.6: A typical CA plot for the oxidation of a metal at a RDE.

By applying an AC potential at different frequencies to the electrochemical system, the impedance of the cell, $Z(\omega)$, is measured. The impedance $Z(\omega)$ is defined as a ratio of the applied potential and the measured current. $Z(\omega)$ has two parts, real (Z_{re}) and imaginary (Z_{im}), $Z_{re} = R$, $Z_{im} = 1/j\omega C$. Plotting EIS data as a Nyquist or complex plane impedance plot gives data that can be modelled by choosing different arrangements of circuit elements. Once the right model is chosen for the electrochemical system, data about R_{ct} , and thus the exchange current and kinetic rate constant can be extracted. Different kinds of circuit models can be used to fit the electrochemical impedance data with the Randles cell being the most common. For a Randles cell model, the impedance plot usually appears as shown in Fig. 1.5.7, consisting of a semicircle and a Warburg line (45 degree straight line). At high frequencies, the CPE acts as an electrical short. Thus, the intercept of the plot on the Z_{re} axis is R_{Ω} . At low frequencies, the CPE is an open circuit, and the impedance is the sum $R_{\Omega} + R_{ct} + W$.

Another real example is the Nyquist plot from a typical surface film shown in Fig 1.5.8.⁵⁰ Because there is no contribution from the diffusion, there will be no W . The semicircle denotes the charge transfer between the electrode and the electrolyte. This simple model contains only R_{Ω} , R_{ct} and a CPE. R_{Ω} is the film resistance, and R_{ct} is related to the rate of charge transfer through the film.

1.6 Research Objectives

In this investigation, our objectives are to

1. Study the anodic dissolution process for Al in two different ionic liquids: the high-melting moisture reactive chloroaluminate system resulting from the combination of aluminium chloride ($AlCl_3$) with NaCl, KBr, LiCl and $AlBr_3$, and a low-melting system based on a

quaternary ammonium chloride salt, 1-ethyl-3-methylimidazolium chloride (EtMeImCl) and AlCl_3 .

2. Investigate the dissolution of Cu in the AlCl_3 -EtMeImCl ionic liquid listed above under Lewis acidic and basic conditions.

3. Probe the nature of the electrode reaction and the electron transfer rate for the electrodisolution of aluminium in the high- and low-melting chloroaluminates as well as copper in the latter.

4. Study the electrode performance, during which all aspects of the processes affecting the electrode reaction rate and the chemical reversibility of the overall electrode reactions will be undertaken.

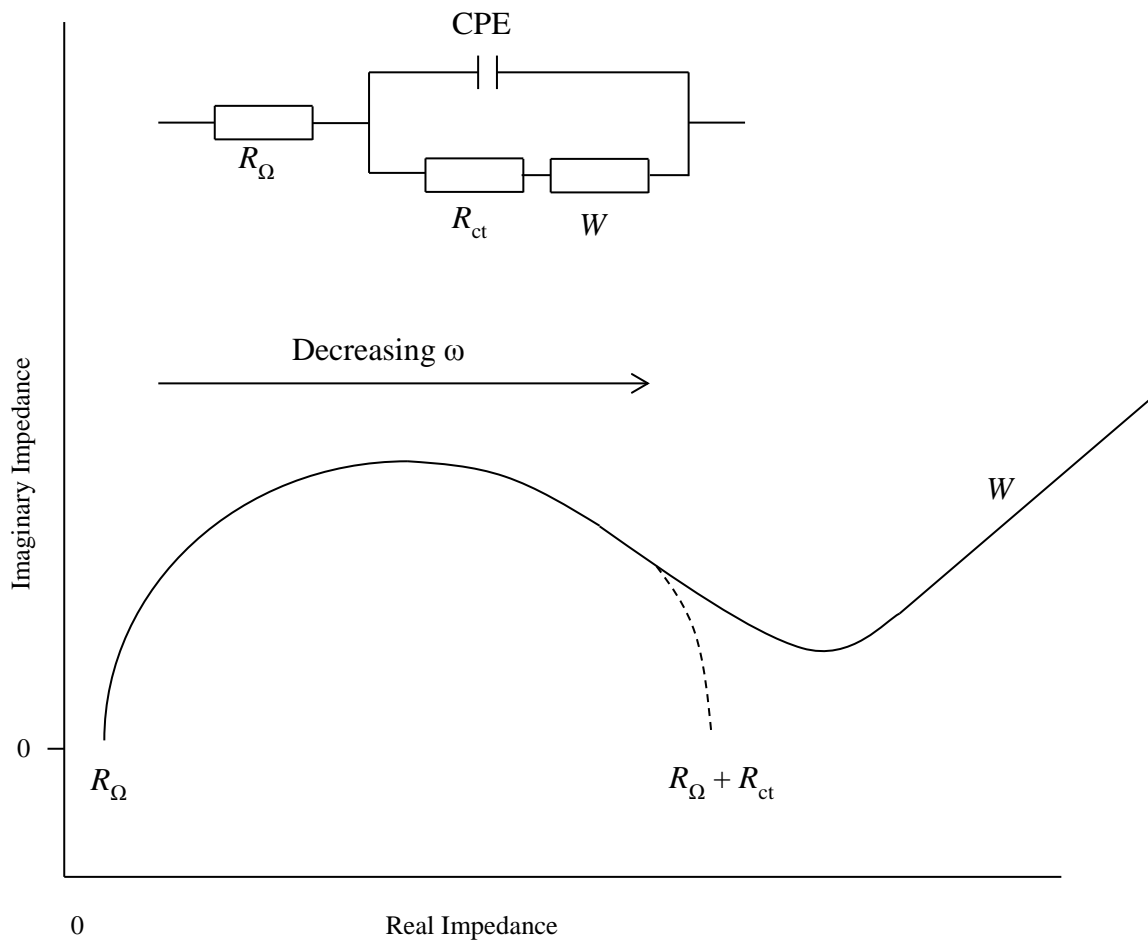


Figure 1.5.7: A typical impedance plot for a Randles cell model.

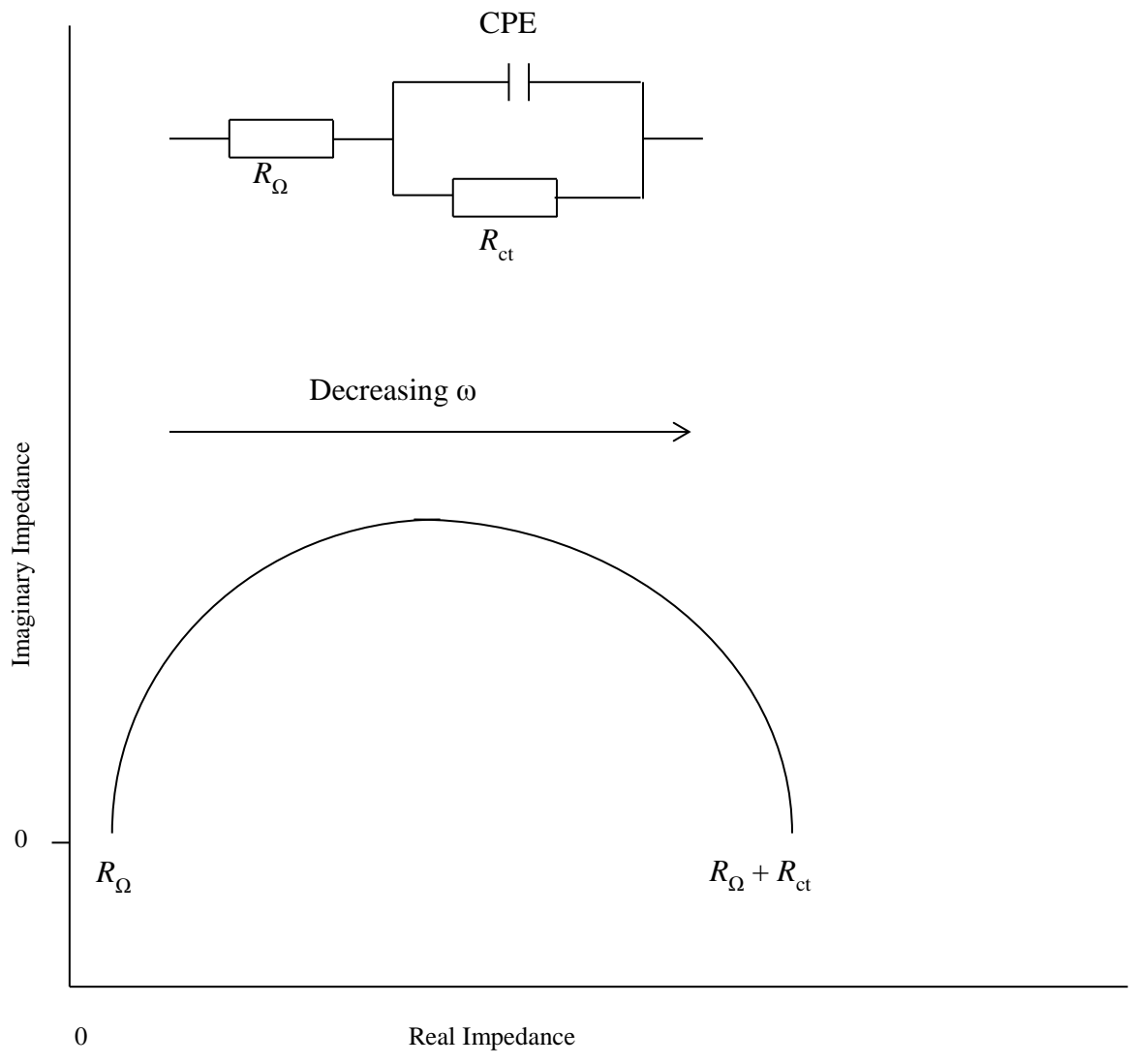


Figure 1.5.8: A Nyquist plot from a typical surface film.

CHAPTER 2

EXPERIMENTAL

2.1 Preparation and Purification of the Chloroaluminate Ionic Solvents

2.1.1 LiAlBr₄-NaAlCl₄-KAlCl₄ (30-50-20 m/o) Molten Salt

The preparation and purification of both ionic solvents was carried out dry nitrogen-filled glove boxes (VAC Atmospheres or LC Technology Solutions, Inc.) with oxygen and moisture contents less than 1 ppm. Aluminum chloride (Fluka >99%) and aluminum bromide (Alfa Aesar, 98%) were purified by vacuum sublimation. Sodium chloride (Alfa Aesar, 99.99%), lithium chloride (Sigma-Aldrich, 99.0%), and potassium bromide (Alfa Aesar, 99%, ACS grade) were purified by fusion in a muffle furnace. The LiAlBr₄-NaAlCl₄-KAlCl₄ (30-50-20 m/o) molten salt was prepared by fusing the five materials in the proper ratio in a sealed flask. The resulting molten salt was purified by continuous electrolysis between two 6-mm diam aluminum rods (Alfa Aesar, Puritronic® grade) at this same temperature for a minimum of three days.

2.1.2 AlCl₃-EtMeImCl Ionic Liquids

Aluminum chloride (Fluka >99%) was purified by vacuum sublimation from the AlCl₃-NaCl melt as described previously.³¹ EtMeImCl (Sigma-Aldrich, BASF, >95.0%) was obtained in the form of a solid yellow-orange crude product and was purified by repeated recrystallization

until a colorless product was obtained. $\text{AlCl}_3\text{-EtMeImCl}$ ionic liquids of the desired composition were prepared by mixing appropriate amounts of the two materials in a flask and stirring for ~2 hours at 50 °C. The Lewis acidic ionic liquids were purified by constant current electrolysis (< 2 V applied potential) between two 6-mm diam aluminum rods (Alfa Aesar, Puritronic® grade) until the final product was water-clear, and cyclic voltammetry (CV) conducted at a Pt electrode indicated that it was free from electroactive impurities

2.2 Density and Viscosity Measurements

Density measurements were carried out in an aluminum-alloy pycnometer (Cole-Parmer, T-38001-00) in a heating mantle. The pycnometer was cleaned thoroughly by using distilled water and dried in an oven before each use. The density of the $\text{AlCl}_3\text{-NaCl}$ (50-50 m/o) molten salt at different temperatures given by Fannin et al.⁵¹ was used to calibrate the volume of the pycnometer. The weight of the pycnometer was determined to ± 0.1 mg after it was cooled to room temperature.

Kinematic viscosities were measured with a modified No. 150 Cannon-Fenske viscometer. The viscometer was capped with a four-way Pyrex glass valve, which was attached to the open ends of the viscometer with ball joints. The two valve stems that were open to the atmosphere were connected to short lengths of Tygon tubing, which were terminated with Drierite-filled drying tubes. The valve could be operated to allow liquid to be drawn into the measuring arm with a vacuum or to connect the open ends to the atmosphere during measurement of the efflux times. The viscometer was calibrated by using the viscosity data for $\text{AlCl}_3\text{-NaCl}$ (50-50 m/o) taken from Brockner et al.⁵² The viscometer was immersed in a temperature bath prepared with poly(ethylene glycol-ran-propylene glycol)monobutyl ether. The

efflux times were measured three times at each temperature to a precision of ± 0.01 s by using a digital stopwatch. All efflux times exceeded 50 seconds. The temperatures of the heating mantle and liquid bath were determined to ± 0.1 °C with a NIST-traceable digital thermometer.

2.3 Electrochemical Measurements

All electrochemistry experiments were carried out in three-electrode Pyrex glass cells inside a glove box with a Biologic SP-200 potentiostat/galvanostat. A Pine Instruments electrode rotator provided controlled electrode rotation. The temperature of the electrochemical cell was maintained in a homemade furnace whose temperature was regulated with an Ace Glass temperature controller to ± 0.5 °C.

For experiments in the $\text{LiAlBr}_4\text{-NaAlCl}_4\text{-KAlCl}_4$ molten salt, the working electrode (WE) was miniature rotating disk electrode (RDE) fabricated from a 2-mm diam Al wire (Alfa Aesar, 99.9995%), which was covered with two layers of heat-shrink Teflon tubing to convert the end of the wire into a miniature disk electrode. This electrode is similar to that described by Holleck and Giner.¹ The wire was mounted with setscrews in a precision mandrel fabricated from the stainless-steel shaft of a Pine Instruments rotating electrode. The setscrews were adjusted as needed to ensure that the electrode ran perfectly true when rotated.

Three different Al WEs were used for experiments in the $\text{AlCl}_3\text{-EtMeImCl}$ Ionic Liquids. The first (Electrode A) was the miniature Al-RDE described above.³¹ The second working electrode (Electrode B) was a Teflon-sheathed aluminum RDE purchased from Pine Instruments Company with a diameter of 5.0 mm. The surface area of this electrode is 0.196 cm^2 . A third Al RDE (Electrode C) was constructed in-house from a short length of 6-mm diam Al rod (Alfa Aesar, Puritronic®, 99.9965%) and was mounted on a Pine Instruments electrode shaft

and fitted with a machined Teflon sheath similar to the Pine RDE. Experiments with copper dissolution were undertaken with a Teflon-sheathed copper RDE purchased from Pine Instruments Company. The surface area of this electrode is 0.196 cm^2 .

All of the working electrodes were polished with 400, 600, and 1500 grit silicon carbide sandpaper before use inside the glove box. In addition, they were further pretreated before data collection by repeated anodic dissolution until the maximum currents were observed at a fixed potential and rotation rate. Furthermore, during data collection, the electrodes were checked frequently against a standard applied potential and electrode rotation rate to make sure that there were no gross changes in electrode area.

The reference electrode (RE) and counter electrode (CE) were also prepared from 2-mm diam Al wire (Alfa Aesar, 99.9995%). The counter electrode was a multi-coil spiral of this wire with an extremely large surface area to prevent CE current limitations. Because experiments in the $\text{LiAlBr}_4\text{-NaAlCl}_4\text{-KAlCl}_4$ did not involve changes in composition, a simple undivided cell was used for experiments in this molten salt. However, the composition was varied in the acidic $\text{AlCl}_3\text{-EtMeImCl}$ ionic liquid. Therefore, the Al reference electrode was isolated in a fine porosity frit tube filled with 60-40 m/o ionic liquid to provide a fixed composition-independent reference point.

The three Al electrodes described above were analyzed using electron backscatter diffraction (EBSD). The samples were sectioned, mounted in epoxy, and polished. Final polishing included vibratory polishing with MasterMet® colloidal silica for 5 hours to provide a ‘deformation free’ surface. EBSD patterns were recorded using Oxford Aztec Software. EBSD scans resulted in hit rates (number of indexed points divided by total number of points) of about 75%. Unindexed pixels were assigned using standard iterating techniques involving nearest

neighbors. Note that this process does create artifacts in the grain size and shape, particularly at the boundaries of the image. Pole figures were created from the grain orientation and contour plots showing the relative intensities of different orientations in the pole figure. Microhardness measurements were performed (Electrodes A and B) on a Buehler Micromet® 5124 machine using a Vickers microindenter and a load of 100 gram-force and indentation time of 15 seconds.

CHAPTER 3

RESULTS AND DISCUSSION

3.1 Aluminum Anodization in the LiAlBr₄-NaAlCl₄-KAlCl₄ Molten Salt

3.1.1 Determination of Physical and Transport Properties

With the exception of the specific conductivities given by Hjuler et al.,¹³ the physical and transport properties of the LiAlBr₄-NaAlCl₄-KAlCl₄ (30-50-20 m/o) molten salt are unknown. Thus, we were obliged to determine the temperature-dependent density and kinematic viscosity of this molten salt over the range of temperatures from 100 to 200 °C. The density and viscosity were measured multiple times at each temperature. The data resulting from density experiments are collected in Table 3.1.1. Sigma-Plot software (V. 8.0.2) was used to fit Eq. 3.1.1 to this data

$$\rho = a + bT \quad [3.1.1]$$

where ρ (g cm⁻³) is the experimental density, T is the temperature (K), and a and b are adjustable parameters. The results of the fitting procedure are collected in Table 3.1.2.

Table 3.1.1: Density, molar conductivity, and viscosity as a function of temperature for LiAlBr₄-NaAlCl₄-KAlCl₄ (30-50-20 m/o).

| T (K) | ρ (g cm ⁻³) | Λ^a (cm ² Ω^{-1} mol ⁻¹) | T (K) | μ (cP) |
|---------|------------------------------|--|---------|------------|
| 391.85 | 2.1018 | 20.9076 | 395.05 | 6.1316 |
| 402.95 | 2.0895 | 24.1308 | 397.35 | 5.7393 |
| 413.45 | 2.0773 | 27.1850 | 405.65 | 5.1422 |
| 423.65 | 2.0715 | 30.0666 | 407.95 | 5.1510 |
| 449.75 | 2.0468 | 37.5373 | 419.45 | 4.4778 |
| 474.05 | 2.0276 | 44.3755 | 421.75 | 4.2710 |
| | | | 444.55 | 3.4252 |
| | | | 444.65 | 3.4566 |
| | | | 467.35 | 2.8523 |
| | | | 467.55 | 2.8710 |

^aCalculated from the density and Table 3.1.2 in ref. 11

Table 3.1.2: Fitted parameters for density, molar conductivity, and viscosity, from Eq. 3.1.1 and 3.1.3.

| | ρ (g cm ⁻³) | Λ (cm ² Ω^{-1} mol ⁻¹) | μ (cP) |
|-----------------------|------------------------------|--|------------|
| <i>a</i> | 2.449 | 7.372 | -3.013 |
| <i>b</i> | -8.913 x 10 ⁻⁴ | -1688 | 1893 |
| <i>r</i> ² | 0.996 | 0.996 | 0.996 |

The specific conductivity, κ , for the LiAlBr₄-NaAlCl₄-KAlCl₄ molten salt can be calculated from the equations and fitted parameters given in the article by Hjuler et al.¹³ By using the density data measured in the present investigation, values of κ from this article were converted to the molar conductivity, Λ (S cm² mol⁻¹), with the well-known expression $\Lambda = \kappa M_x / \rho$, where M_x is the molecular weight of the LiAlBr₄-NaAlCl₄-KAlCl₄ mixture (243.53 g mol⁻¹). M_x was calculated from the formula

$$M_x = x_{\text{LiBr}}M_{\text{LiBr}} + x_{\text{KCl}}M_{\text{KCl}} + x_{\text{NaCl}}M_{\text{NaCl}} + x_{\text{AlBr}_3}M_{\text{AlBr}_3} + x_{\text{AlCl}_3}M_{\text{AlCl}_3} \quad [3.1.2]$$

(For convenience, in subsequent discussions we represent the molten salt anion as the nominal “average” haloaluminate species, AlX₄⁻, where X⁻ = (0.30 Br⁻ + 0.70 Cl⁻.) The resulting calculated values of Λ are given in Table 3.1.1. The kinematic viscosities resulting from the viscometry experiments conducted over the temperature range from 120 to 200 °C were converted to absolute viscosities, μ (cP or mPa·s), by using density data calculated from Eq. 3.1.1. These results are also shown in Table 3.1.1.

In both cases, the experimental transport data were represented by a simple linearized form of the Arrhenius equation.^{53,54}

$$\ln \Lambda \text{ or } \ln \mu = a + b/T \quad [3.1.3]$$

Equation 3.1.3 was fitted to the molar conductivity and absolute viscosity data, and the resulting parameters are given in Table 3.1.2.

In Eq. 3.1.3, the coefficient b contains information about the activation energy for the respective transport process. The activation energy for the molar conductivity is $E_{a,\Lambda} = -bR = 14.03 \text{ kJ mol}^{-1}$, whereas the activation energy for viscous flow is $E_{a,\mu} = bR = 15.74 \text{ kJ mol}^{-1}$. Although there is a paucity of data for Lewis neutral alkali haloaluminate systems with mixed halide or bromide anions similar to that studied here, a few comparisons can be made with some binary chloride-based systems. For example, $E_{a,\Lambda} = 11.49 \text{ kJ mol}^{-1}$ for the $\text{AlCl}_3\text{-LiCl}$ (50-50 m/o) molten salt,¹⁴ whereas $E_{a,\mu} = 13.50 \text{ kJ mol}^{-1}$ for the nominal $\text{AlCl}_3\text{-NaCl}$ melt (50-50 m/o).⁵⁵ Thus, the activation energies for the transport properties determined in this mixed halide system are more than 2 kJ mol^{-1} higher than found in the related chloride systems, probably due to the presence of larger anions containing bromide.

Table 3.1.3 shows a generalized comparison of the densities, viscosities and molar conductivities of several well-known molten salts/ionic liquids as well as selected data for the $\text{LiAlBr}_4\text{-NaAlCl}_4\text{-KAlCl}_4$ melt. Irrespective of the measurement temperature associated with each entry, comparison of this data reveals that the density of the $\text{LiAlBr}_4\text{-NaAlCl}_4\text{-KAlCl}_4$ molten salt is the highest of those listed, whereas the viscosity of this system is among the lowest. The molar conductivity is also quite good and compares favorably with that for $\text{AlCl}_3\text{-NaCl}$ (50-50 m/o) at the much higher temperature of $200 \text{ }^\circ\text{C}$. The molar volume of this mixed chloride-bromide melt, which reflects the packing of the anions and cations in the molten salt, is about the same as that of the organic chloroaluminate $\text{AlCl}_3\text{-EtMeImCl}$ (50-50 m/o), which is an ionic liquid based on large organic cations.

Table 3.1.3: Physical and transport properties of various molten salts and ionic liquids.

| Molten salt/ionic liquid | t (°C) | ρ (g cm ⁻³) | V_M (L mol ⁻¹) | μ (cP) | Λ (cm ² Ω ⁻¹ mol ⁻¹) |
|--|-------------|---------------------------------|---------------------------------|---------------|---|
| BuMePyroTf ₂ N ⁶⁰ | 35 | 1.3858 | 0.3048 | 50.12 | 1.25 |
| EtMeImTf ₂ N ⁶⁰ | 35 | 1.5089 | 0.2593 | 23.11 | 3.18 |
| BuMeImTf ₂ N ⁶⁰ | 35 | 1.4268 | 0.2939 | 33.58 | 1.72 |
| AlCl ₃ -EtMeImCl (50-50 m/o) ⁶³ | 35 | 1.2861 | 0.1088 | 13.76 | 3.10 |
| AlCl ₃ -NaCl (50-50 m/o) ^{51, 52, 64} | 200 | 1.6822 | 0.0570 | 2.25 | 29.76 |
| LiAlBr ₄ -NaAlCl ₄ -KAlCl ₄ (30-50-20 m/o) | 120 | 2.0980 | 0.1161 | 6.19 | 21.31 |

We also examined the relationship between the viscosity and conductivity of the LiAlBr₄-NaAlCl₄-KAlCl₄ molten salt by application of the well-known fractional Walden rule,⁵⁶ given here in logarithmic form

$$\log \Lambda = \alpha \log \mu^{-1} + \log C' \quad [3.1.4]$$

Although somewhat controversial,⁵⁷ this simple empirical expression nevertheless provides a reliable way to relate Λ to the fluidity, $1/\mu$, (P^{-1}) of a molten salt/ionic liquid. It is arbitrarily referenced to a single data point based on a 1.0 M aqueous solution of KCl. The “ideal line” of the Walden plot is constructed from this data point. It is given a unit slope and passes through the origin of the plot, i.e., $C' = 1$. Electrolytes that fall on the line of this plot are considered to be ideal with the cations moving independently of the anions (high ionicity), whereas those that fall below the line with $C' < 1$ tend to show ion associations leading to measureable vapor pressures (low ionicity).⁵⁸ The slope, α , accounts for the fact that for most electrolytes the slopes of plots of $\log \Lambda$ versus $\log \mu^{-1}$, even those that intersect the ideal Walden line at some point, are almost always less than unity and tend to vary with temperature. Angell and coworkers⁵⁶ interpret this behavior as an increase the number of non-conducting ion pairs as the temperature is increased. This method of transport property analysis has been applied on numerous occasions to second-generation ionic liquids. For a recent example from our laboratory, see Fig. 5 in Pan, et al.⁵⁹ viscosity and conductivity data described above as well as a plots for AlCl₃-NaCl (50-50 m/o), AlCl₃-EtMeImCl (50-50 m/o), and the second generation ionic liquid, BuMePyroTf₂N, are

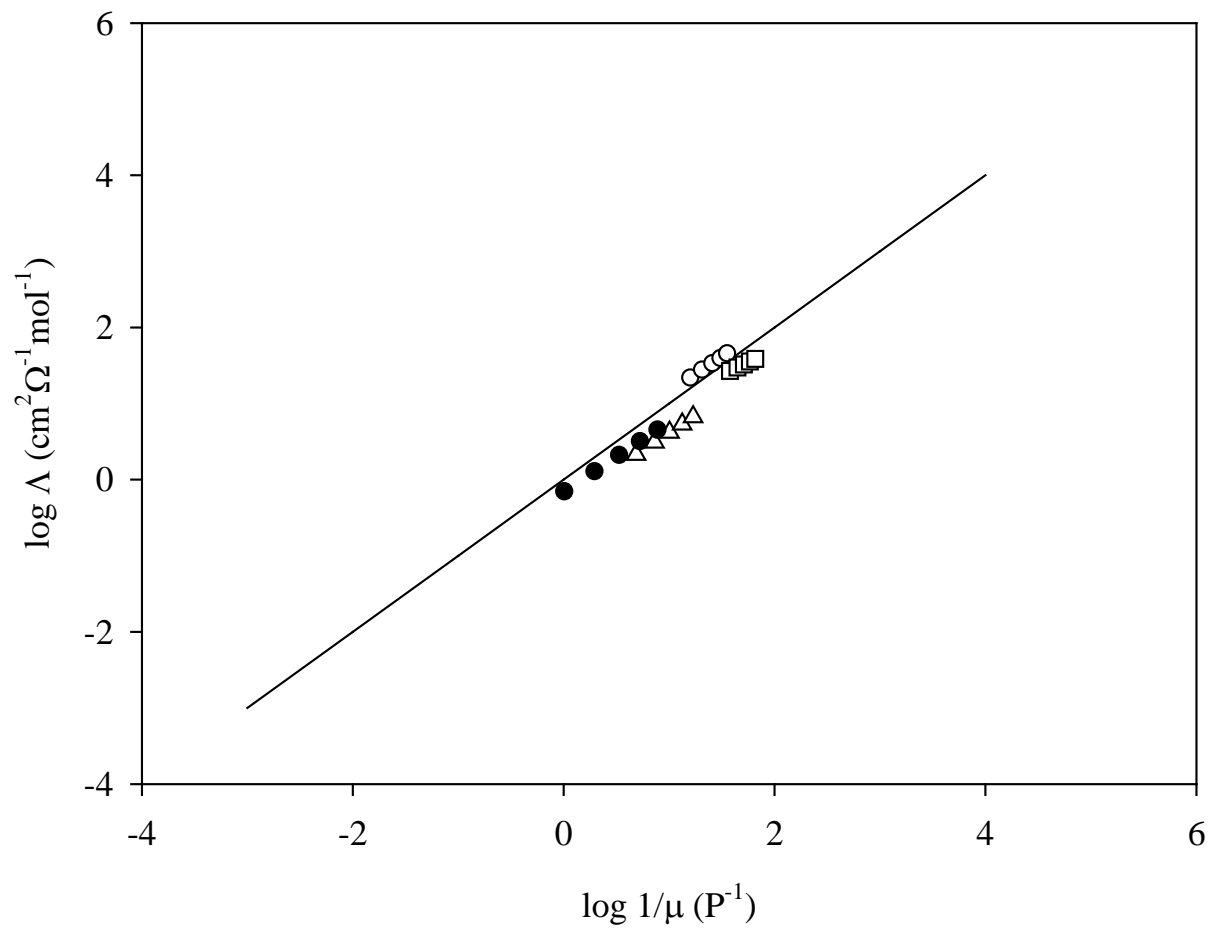


Figure 3.1.1: Walden plots for: (\circ) $\text{LiAlBr}_4\text{-NaAlCl}_4\text{-KAlCl}_4$ (30-50-20 m/o), (\square) $\text{AlCl}_3\text{-NaCl}$ (50-50 m/o), (\triangle) $\text{AlCl}_3\text{-MeEtImCl}$ (50-50 m/o), and (\bullet) $\text{BuMePyroTf}_2\text{N}$. The solid line is the ideal line for a 1 M aqueous KCl solution.

compared in Fig. 3.1.1. Unlike the latter three systems, the data for molten $\text{LiAlBr}_4\text{-NaAlCl}_4\text{-KAlCl}_4$ fall on the Walden line, suggesting that this molten salt is very close to an ideal electrolyte. According to Angell's classification system,⁶⁰ they can be classified as "good" ionic liquids. These results are quite similar to those reported for the $\text{ZnCl}_2\text{-NaCl-KCl}$ (60-20-20 m/o) molten salt.⁶¹ The exponent α was obtained from the slope of a linear plot of $\log \Lambda$ versus $\log \mu^{-1}$ and found to be 0.899 as is the case for almost all molten salts and ionic liquids that have been examined in this way.

3.1.2 Anodization of Al Electrodes

In the simple undivided cell used for these anodization experiments, which consisted of an Al RDE electrode and Al wire reference electrode immersed in the pure melt, the equilibrium potential, E_{eq} , is 0 V. Defining the overpotential, η , as $E_{\text{app}} - E_{\text{eq}}$, where E_{app} is the applied potential, the application η of greater than 0 V to the Al RDE electrode should initiate the anodization of Al into the molten salt. Figure 3.1.2 shows current density-time plots resulting from potential-step experiments recorded at the Al RDE as a function of η at a fixed electrode rotation rate, ω . Results obtained at two different temperatures are included in this graph. At $\eta \leq 0.40$ V, the anodization current densities reach steady-state values at about 3s after the imposition of the potential step. (This invariance of the current densities with time indicates that there is little change in the effective area of the Al RDE electrode on the time scale of these experiments.) However, if η is increased to 0.50 V, the current densities increase commensurately immediately following the application of the potential step, but then decrease to time- and potential-independent values, indicative of passivation of the Al surface.¹ Temperature is an important factor here because passivation occurs more quickly at 111 °C than at 131 °C. At

the latter temperature, the electrode must be anodized for up to 300 s before the current density reaches a steady-state value. When the temperature was increased to 151 °C, passivation could not be detected, regardless of the value of η . However, experiments at this temperature created practical problems because the anodization rate was so great that the Al RDE, which was prepared with annealed (soft) Al, had to be renewed frequently.

Figure 3.1.3 shows graphs of the current densities versus η taken from the data in Fig. 3.1.2. These graphs are equivalent to the manual recording of sampled-current voltammograms. The aforementioned dependence of the Al RDE current density on η is obvious. That is, at short sampling times (10 s), the current density exhibits an extralinear increase with η . At longer sampling times (300 s), the current density attains a potential-independent, limiting value, but only when $\eta \geq \sim 0.50$ V. One possible explanation for these results is a mechanism involving these reactions



At η values less positive than those leading to the onset of passivation, the electrode reaction proceeds completely according to the established multielectron reaction depicted in Eq. 3.1.5, where the ultimate Al oxidation product is Al_2X_7^- .²⁷ As η is made more positive, and the rate of the Al anodization reaction increases, the electrode diffusion layer becomes rich in AlX_3 . The

solubility of this species is eventually exceeded, and the electrode becomes passivated by a thin layer of $\text{AlX}_3(\text{s})$, as indicated in Eq. 3.1.6. Similar results were noted by Gilbert, et al.²⁹ during a chronopotentiometric study of Al oxidation in Lewis acidic $\text{AlCl}_3\text{-NaCl}$. Following the onset of passivation, the current densities reach limiting values (Fig. 3.1.3), which are governed by the steady-state formation and dissolution of $\text{AlX}_3(\text{s})$ according to the reactions shown in Eq. 3.1.6 and 3.1.7, respectively.

Figure 3.1.4 shows Levich plots prepared with data taken from potential step experiments with $t = 300$ s at different electrode rotation rates. The two plots that resulted from experiments at potentials where passivation is observed, in this case $\eta = 0.70$ V, are reasonably linear and pass through the origin. As indicated by Fig. 3.1.3, similar results were obtained from all experiments carried out at $\eta \geq 0.50$ V. These results confirm that the passivation process is convective mass-transport controlled. The current density-time graphs in Fig. 3.1.2 (upper) show some unusual minima at shorter times. Holleck and Giner¹ proposed that such minima might be due to the supersaturation of the diffusion layer by liquid AlCl_3 followed by the subsequent precipitation of $\text{AlCl}_3(\text{s})$. The proposed passivation mechanism described above is consistent with this explanation.

3.1.3 Heterogeneous Kinetics of the Al Anodization Reaction

Unlike the linear Levich plots in Fig. 3.1.4 derived from data at $\eta = 0.70$ V that are indicative of mass transport control, the plots in this figure resulting from experiments at $\eta \leq 0.30$ V are clearly non-linear and show only a small dependence on the electrode rotation rate. Given that passivation is clearly absent at these potentials, these plots indicate that the anodization reaction (Eq. 3.1.5) proceeds under mixed kinetic/mass transfer control. In order to

probe the kinetic rate of the heterogeneous reaction in Eq. 3.1.5, Al RDE experiments were carried out at temperatures ≥ 150 °C where passivation does not take place within the accessible potential range. One example of the results of such Al RDE experiments is shown in Fig. 3.1.5a. Again, the non-linearity of the Levich plots is very obvious. To extract kinetic information, Koutecky-Levich plots were constructed from the data in Fig. 3.1.5a and are shown in Fig. 3.1.5b. The intercepts of these plots at infinite rotation rate contain information about the potential-dependent anodic rate constant, k_a , of the Al anodization reaction (Eq. 3.1.5) according to the following expression⁴⁷

$$1/j_a = 1/(3Fk_a) + k_c/k_a[0.537(FD^{2/3})^{-1}v^{1/6}] \omega^{-1/2} \quad [3.1.8]$$

In deriving Eq. 3.1.8, the reducible product of the Al anodization reaction, $Al_2X_7^-$, is considered to be absent from the bulk molten salt, which eliminates the need to consider the cathodic back reaction.

The anodic rate constant of the reaction given in Eq. 3.1.5 referenced to E_{eq} or zero current, $k_{a,0}$, was estimated from the intercept of a plot of $\ln k_a$ versus η , according to the expression

$$\ln k_a = \ln k_{a,0} + \alpha_a F \eta / RT \quad [3.1.9]$$

where α_a is the apparent anodic transfer coefficient defined here as $(RT/F)(d \ln k_a / d \eta)$.⁶² A plot of the 151 °C data is shown in Fig. 3.1.6. Analysis of the slope and intercept of this plot leads to

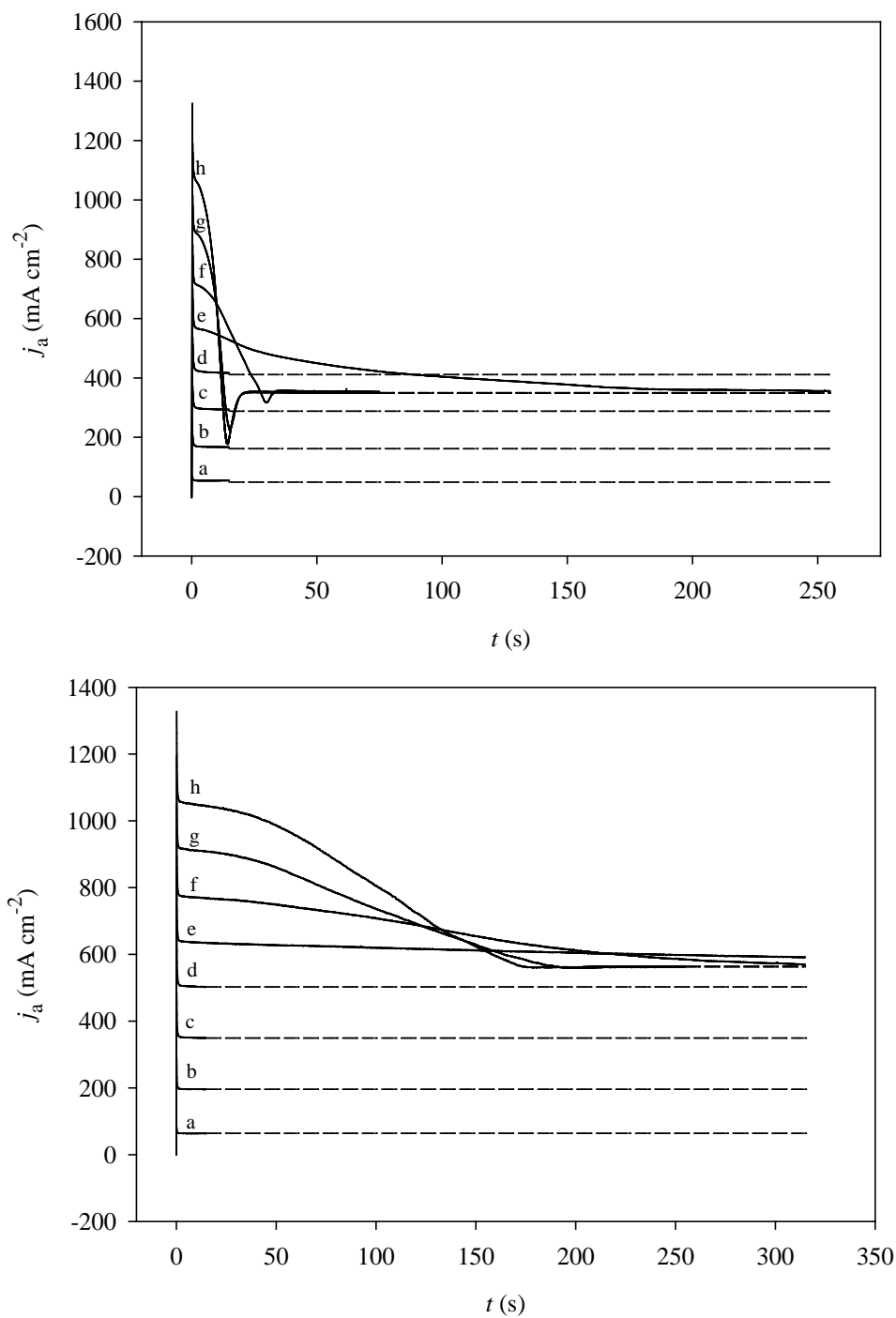


Figure 3.1.2: Current-time plots recorded during the anodization of an Al RDE at different overpotentials: (a) 0.10 V, (b) 0.20 V, (c) 0.30 V, (d) 0.40 V, (e) 0.50 V, (f) 0.60 V, (g) 0.70 V, and (h) 0.80 V. The temperature was (upper) $111\text{ }^\circ\text{C}$ and (lower) $131\text{ }^\circ\text{C}$. The rotation rates were 157 rad s^{-1} .

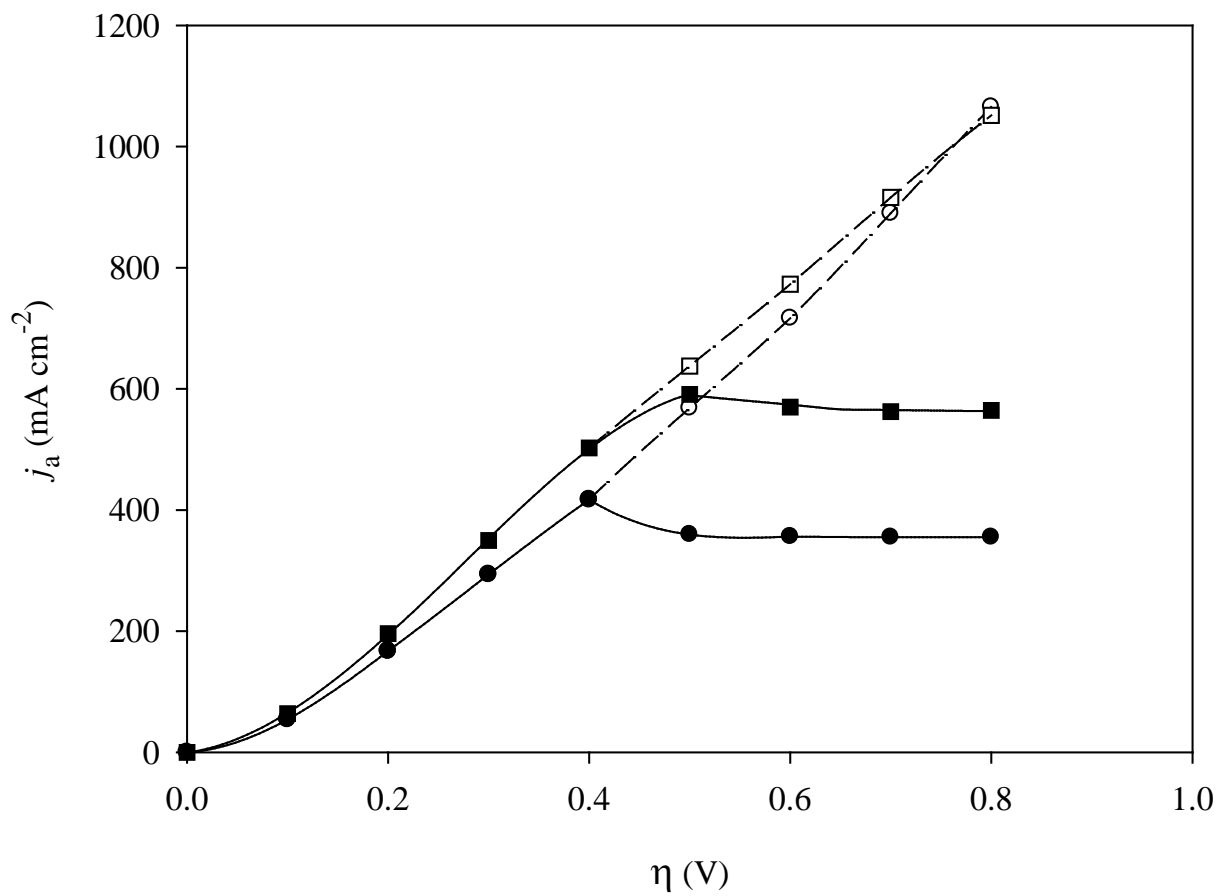


Figure 3.1.3: Current-sampled voltammograms constructed from the data in Fig. 3.1.1 and 3.1.2: (○) 111°C and 10 s; (●) 111°C and 300 s, (□) 131°C and 10 s, and (■) 131°C and 300 s. The rotation rates were 157 rad s⁻¹.

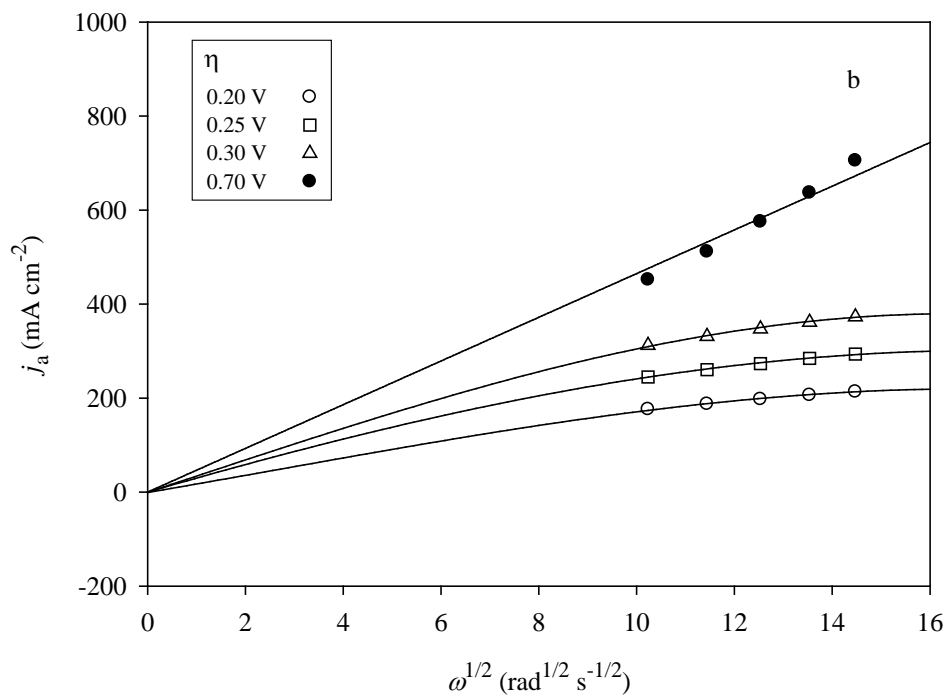
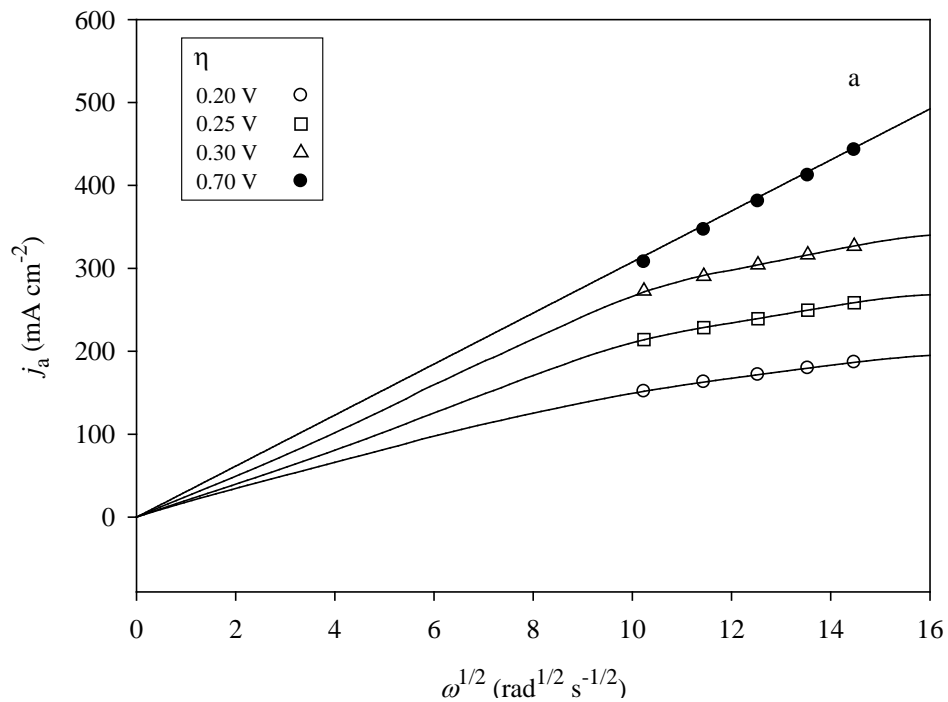


Figure 3.1.4: Levich plots for the anodization of an Al RDE in the molten salt at (a) 111°C and (b) 131°C. The currents were sampled at 300 s.

$k_{a,0} = 6.5 \times 10^{-7} \text{ cm s}^{-1}$ and $\alpha_a = 0.168 \pm 0.006$. The exchange current density, j_0 , is 0.19 A cm^{-2} , which is about 70 % of that measured for Al dissolution in the acidic $\text{AlCl}_3\text{-KCl-NaCl}$ (57.5-12.5-20.0 m/o) molten salt at $130 \text{ }^\circ\text{C}$ by using galvanostatic pulse techniques.¹ Interestingly, experiments conducted at higher temperatures and in the related low melting $\text{AlCl}_3\text{-EtMeImCl}$ ionic liquid at $50 \text{ }^\circ\text{C}$ gave virtually the same result for α_a . A simplistic interpretation of this result is that the Al anodization mechanism does not change with temperature over the range investigated.

In order to estimate the Gibbs free energy of activation, ΔG_a^\ddagger , for this reaction under the described conditions, we determined $k_{a,0}$ at several additional temperatures using the same experimental procedure described above. The results were very similar to those obtained at $151 \text{ }^\circ\text{C}$ (Fig. 3.1.5 and 3.1.6), and for reasons of space and repetition these plots are not reproduced here. The results were analyzed with a simple Arrhenius-type expression, with the assumption that ΔG_a^\ddagger and A are independent of temperature in the range investigated

$$\ln k_{a,0} = \ln A - \Delta G_a^\ddagger/RT \quad [3.1.10]$$

A plot of $\ln k_{a,0}$ versus $1/T$ is shown in Fig. 3.1.7. Analysis of the slope and intercept that resulted from the fitting of Eq. 3.1.10 to this data gave $\Delta G_a^\ddagger = 17.1 \text{ kJ mol}^{-1}$ and $A = 8.3 \times 10^{-5} \text{ cm s}^{-1}$ with $R^2 = 0.97$. These data can then be used with Eq. 3.1.9 and 3.1.10 to predict $k_{a,0}$ at different temperatures and the corresponding values of k_a at different η or E_{app} in the absence of passivation.

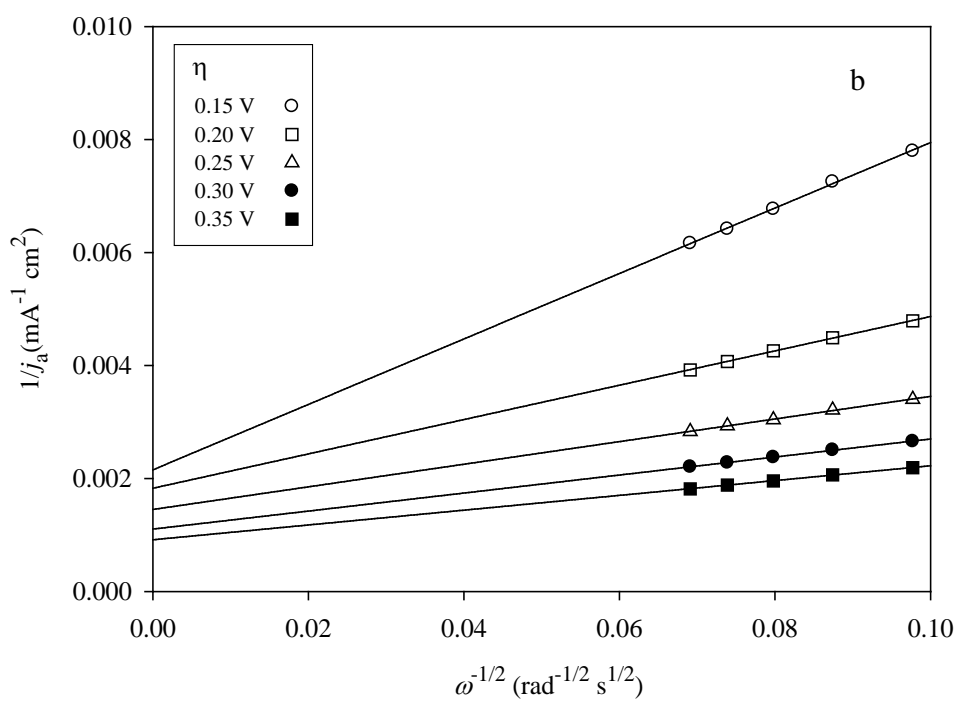
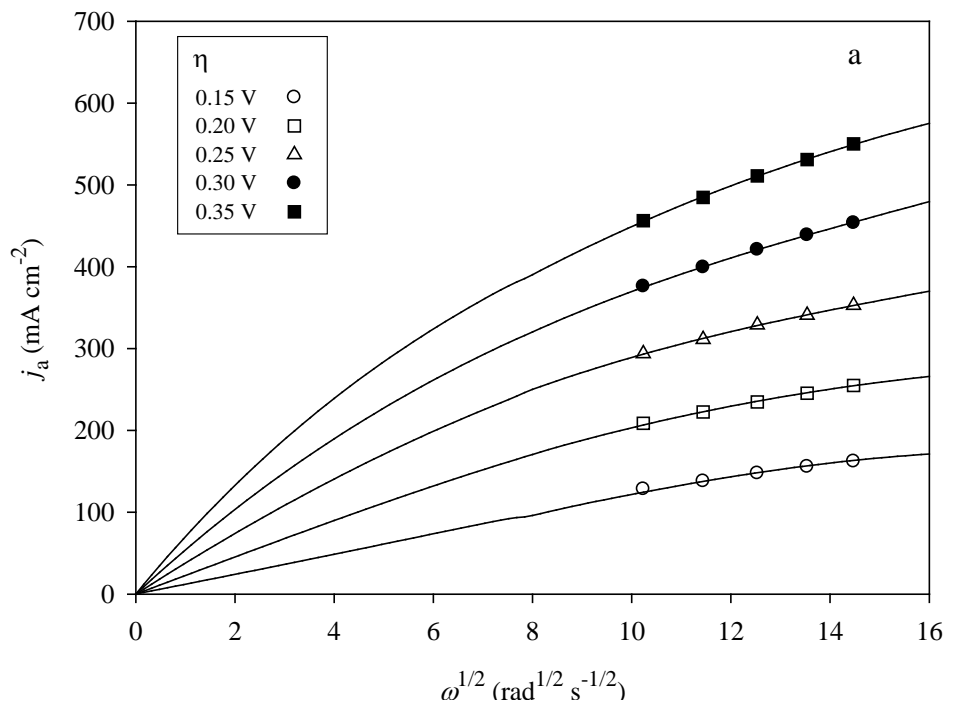


Figure 3.1.5: (a) Levich plots for the anodization of an Al RDE in the molten salt at 151°C. The currents were sampled at 300 s; (b) Koutecky-Levich plots constructed from the data in (a).

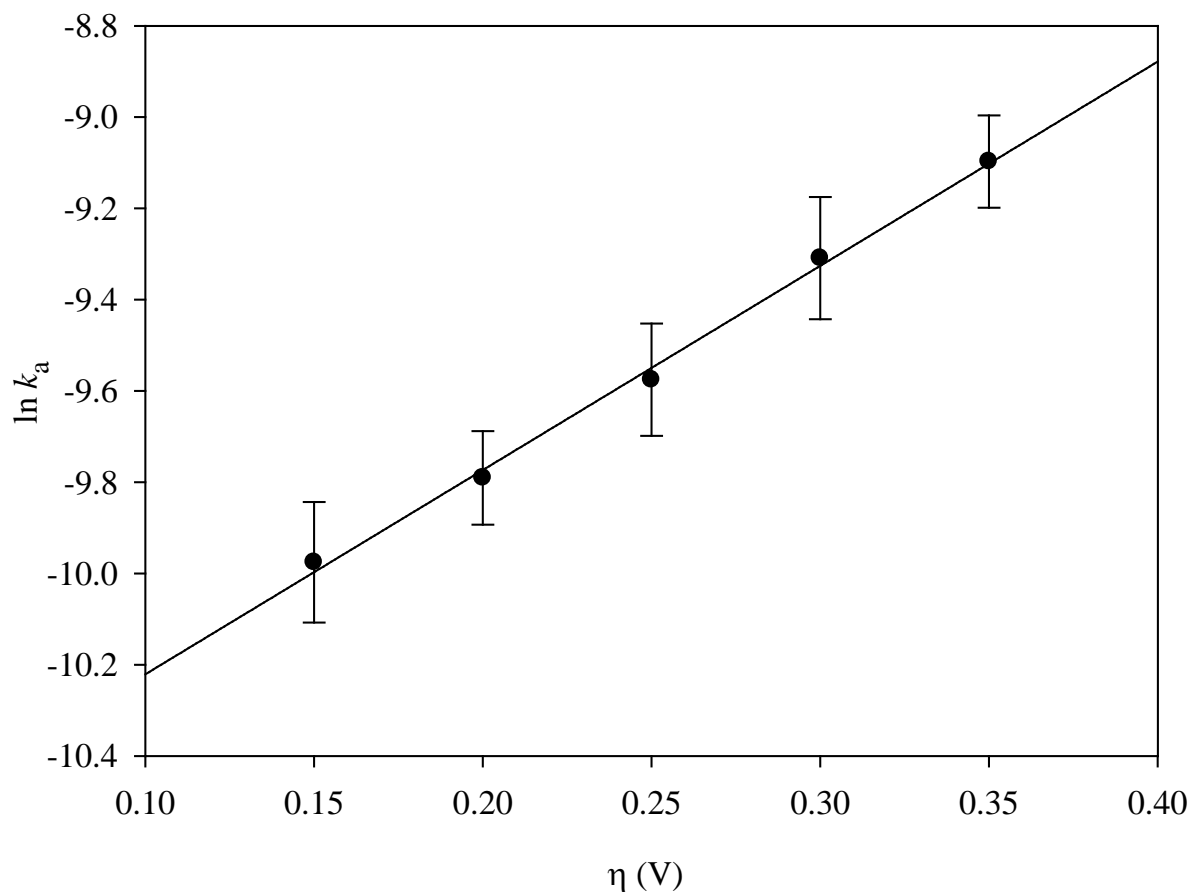


Figure 3.1.6: Plot of the anodic rate constant versus the overpotential calculated from data similar to that shown in Fig. 3.1.5b. The results shown here are the average values of five independent experiments.

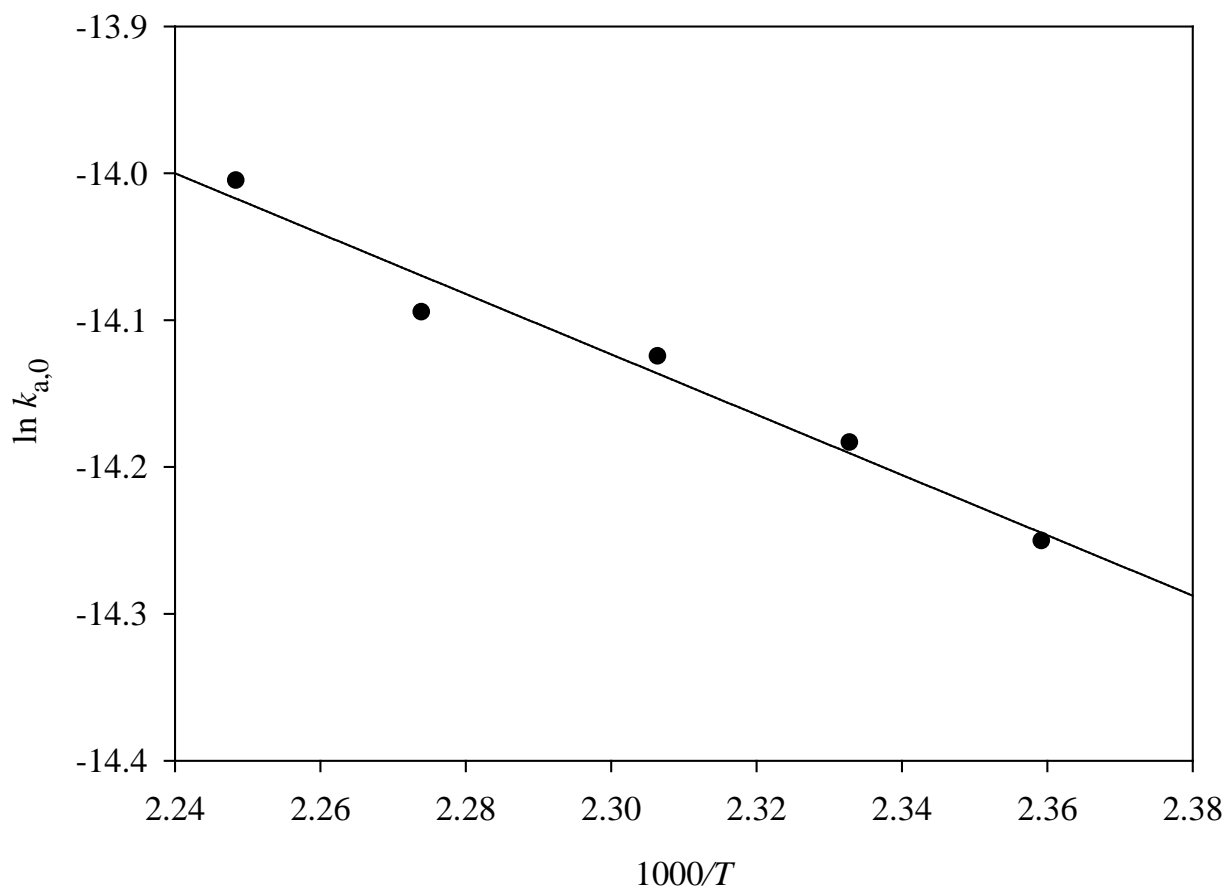


Figure 3.1.7: Arrhenius plot for the anodic rate constant referenced to the equilibrium potential.

3.1.4 Summary

In conclusion, the low-melting Lewis-neutral $\text{LiAlBr}_4\text{-NaAlCl}_4\text{-KAlCl}_4$ (30-50-20 m/o) molten salt proved to be a useful model system for investigating the electrodisolution of aluminum at elevated temperatures. Experiments with this low vapor pressure, high-ionicity haloaluminate melt proved that the mass transport-limited oxidation of aluminum in inorganic haloaluminates described in the early literature actually results from the dissolution of a passive layer of AlCl_3 from the electrode surface. In the absence of this passivation phenomenon, the rate of the aluminum dissolution reaction is considerably greater, but in this case the process is quasireversible, i.e., it proceeds under mixed kinetic/mass transport control. Again by carrying out experiments with the Al RDE, we measured the heterogeneous rate constant for the anodization reaction referenced to the equilibrium potential. One disadvantage of this molten salt is that its Lewis acidity cannot be changed conveniently by the addition of AlCl_3 or AlBr_3 without a marked increase in vapor pressure. This is a problem that plagues all Lewis acidic haloaluminate systems prepared from alkali halide salts. Thus, future work involving the anodization of Al will be extended to organic salt-based room temperature haloaluminate systems such as $\text{AlCl}_3\text{-1-ethyl-3-methylimidazolium chloride}$, where the influence of the Lewis acidity (Al_2Cl_7^- concentration) on the Al dissolution process can be readily investigated. Finally, it is important to note that the results presented herein are specific to annealed Al. Preliminary experiments with hardened or tempered Al resulted in an anodization rate that was only a fraction of that reported herein for the softer, annealed samples. These results will be the subject of a future communication.

3.2 Anodic Dissolution of Aluminum in the Aluminum Chloride-1-Ethyl-3-methylimidazolium Chloride Molten Salt

3.2.1 Characterization of the Al Anode Film in AlCl₃-EtMeImCl

As noted in the experimental section, the acidic AlCl₃-EtMeImCl ionic liquid is conveniently purified by electrolysis between Al electrodes. During electrolysis, the anode rod sometimes developed a water-insoluble black coating. The formation of this black surface film on Al anodes in chloroaluminate molten salts and ionic liquids has been reported by many workers^{21, 24, 29, 65, 66} and has been attributed to finely divided Al resulting from the disproportionation of subvalent Al species produced during an initial one-electron oxidation reaction.^{65,66} Gale and Osteryoung²⁴ investigated this phenomenon in some detail in acidic AlCl₃-NaCl, but were unable to confirm the participation of subvalent Al ions. Their analysis of this film by atomic emission spectroscopy indicated that it consisted of Si, B, Sn, Mn, as well as Al. Collection and subsequent analysis by energy dispersive x-ray spectroscopy (EDS) of the black material produced on the Al anode in acidic AlCl₃-EtMeImCl indicated that it was almost completely carbonaceous. We found that by repeatedly removing the rod from the electrolysis cell and cleaning off this black material it was eventually possible to remove all of the impurities in the ionic liquid that produced the film, and the electrode remained bright. Thus, it seems unlikely in this case that the black film results from the disproportionation of subvalent species during the dissolution of Al in acidic AlCl₃-EtMeImCl.

3.2.2 Anodic Dissolution Experiments

The experiments used to characterize the anodization of aluminum electrodes in the AlCl₃-EtMeImCl ionic liquid were similar in scope and function to those conducted in the LiAlBr₄-

NaAlCl₄-KAlCl₄ (30-50-20 m/o) molten salt at $t > 100$ °C and are described in a recent article.²⁸ However, the results were considerably different from those obtained in this previous study because the current density for the oxidation of Al in the ionic liquid was much smaller than observed in the higher melting salt mixture, owing to the significantly lower conductivity of the ionic liquid. As noted above, experiments were conducted in an undivided cell. In this cell, the equilibrium potential, E_{eq} , of the Al working electrode is 0 V. Thus, if the overpotential, η , is greater than this value, the anodization of Al will take place.

The current-potential behavior of the Al electrode was studied at the three Al rotating disk electrodes described in the Experimental Section by applying potential steps and then observing the oxidation current as a function of time. The overpotentials, η , used varied from 0.1 to 1.0 V. Figure 3.2.1 shows current-time plots recorded during the anodization of the three Al electrodes (samples A, B, and C) at fixed temperatures and angular frequencies, ω (s⁻¹). For $\eta \leq 0.0$ V, the current densities reach constant values about 1 s after the potential is applied. These current densities are potential dependent, but time independent. However, for $\eta > 0.60$ V, the current densities increase at the beginning of the potential-step experiments, but then decrease sharply thereafter and become independent of both time and overpotential. These sharp decreases in current were attributed to a passivation-like process occurring on the Al electrode surface.¹ The onset of this passivation process is potential-dependent, with passivation occurring sooner when the overpotential is larger. Thus, the oxidation of Al appears to involve two distinct mechanisms depending on the overpotential/anodic dissolution rate. The first is an active dissolution process represented by the overall reaction,



which is simply the reverse of Eq. 1.1.6,²⁷ and another process leading to the passivation-like behavior. We have addressed both of these scenarios below in more detail.

In order to study the passive dissolution process, additional experiments were performed as a function of temperature and composition. However, instead of plotting the resulting current densities as a function of time, the results are presented as current-sampled voltammograms. The results obtained with Electrode A (Al wire RDE) are shown in Fig. 3.2.2. In each case, the currents were recorded after each potential step when they had reached a constant, time independent value. The results for the Electrode B (Pine Al RDE) and Electrode C (Al RDE prepared in-house) were similar, but passivation could not be achieved under all of the conditions represented in this figure at these much larger area electrodes due experimental limitations resulting from the higher current densities that were required. Figure 3.2.2 confirms the potential independence of the current densities at large overpotentials. Passivation is most readily achieved in the more acidic (highest AlCl₃ content) ionic liquids and can scarcely be induced in the less acidic ionic liquids i.e., < 55 m/o AlCl₃. We also investigated the effect of temperature, but were limited to a maximum of ~60 °C to avoid physical damage to the larger Teflon-shrouded Electrodes (B and C).

From the graphs in Fig. 3.2.2, it is also possible to define a critical current density, j_{crit} , for the anodic dissolution reaction. At a fixed temperature and ionic liquid composition, this is the largest current density that can be supported continuously by the anode reaction under the specified convective conditions without inducing passivation. Assuming that the cathode reaction does not control the cell current, this empirical parameter might be useful in the design

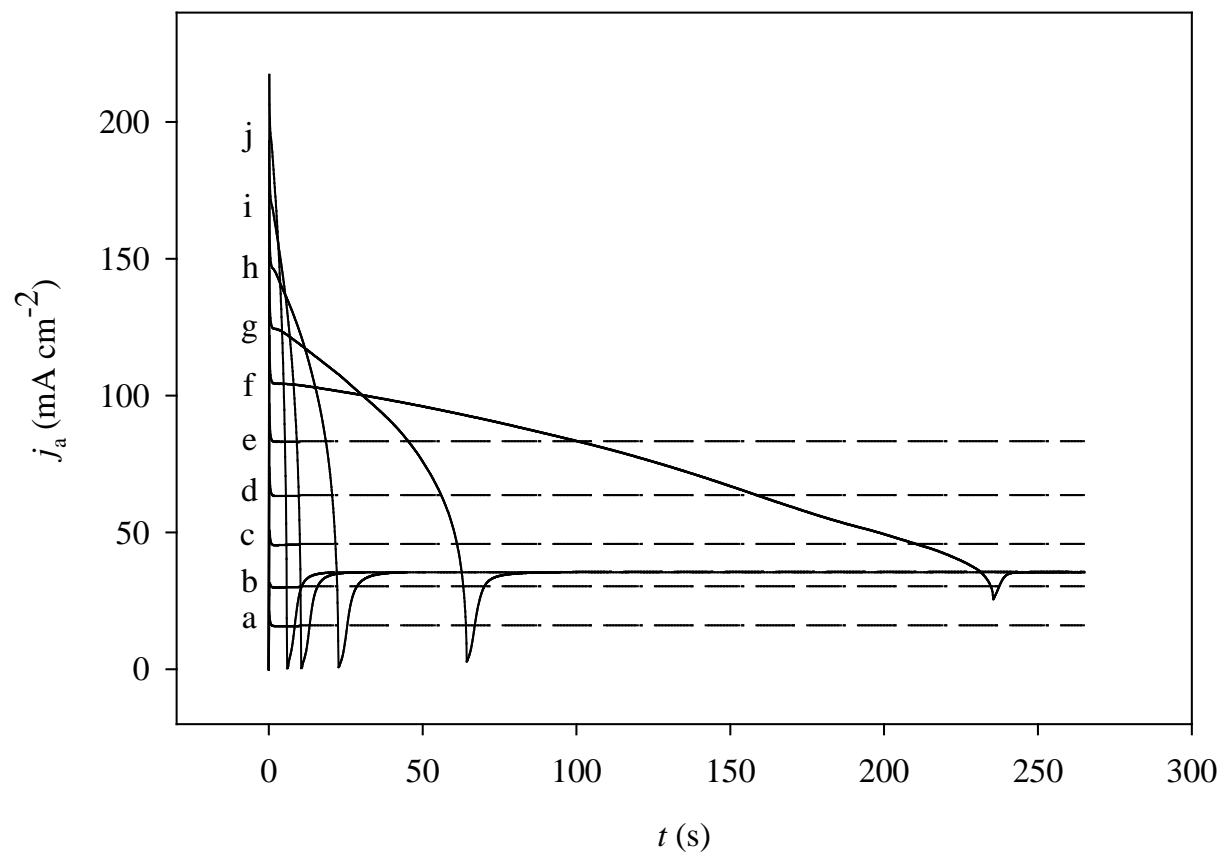


Figure 3.2.1(A): Current-time plots recorded during the anodization of Electrode A at different anodic overpotentials in the 65 m/o ionic liquid: (a) 0.045 V, (b) 0.096 V, (c) 0.143 V, (d) 0.181 V, (e) 0.213 V, (f) 0.478 V, (g) 0.578 V, (h) 0.678 V, (i) 0.778 V and (j) 0.878 V. The temperature was 32 °C, and the electrode rotation rates were 157 rad s⁻¹.

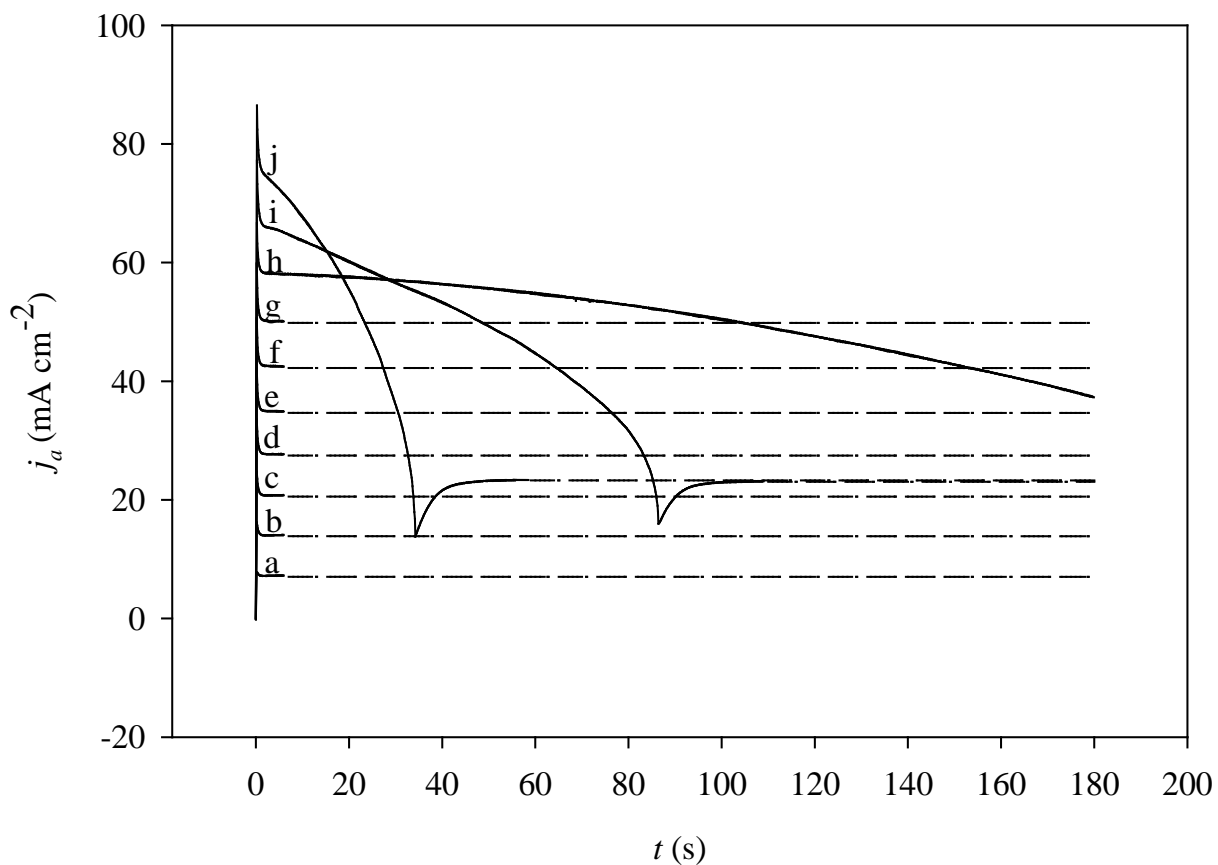


Figure 3.2.1(B): Current-time plots recorded during the anodization of electrode B at different anodic overpotentials in the 65 m/o ionic liquid: (a) 0.028 V, (b) 0.060 V, (c) 0.093 V, (d) 0.125 V, (e) 0.153 V, (f) 0.178 V, (g) 0.202 V, (h) 0.428 V, (i) 0.668 V and (j) 0.766 V. The temperature was 32 °C, and the electrode rotation rates were 157 rad s⁻¹.

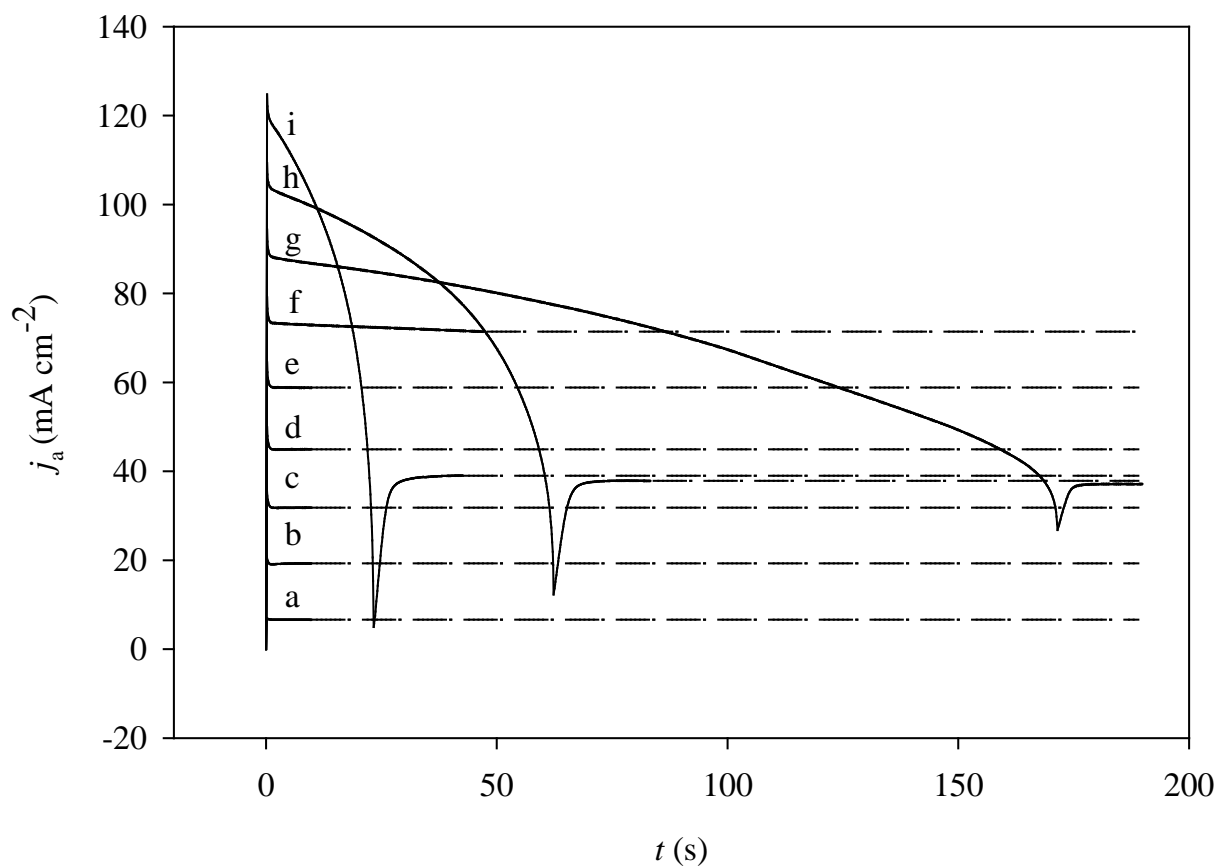
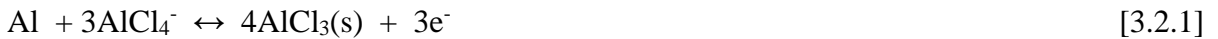


Figure 3.2.1(C): Current-time plots recorded during the anodization of electrode C at different anodic overpotentials in the 65 m/o ionic liquid: (a) 0.028 V, (b) 0.089 V, (c) 0.151 V, (d) 0.208 V, (e) 0.256 V, (f) 0.318 V, (g) 0.893 V, (h) 1.086 V, and (i) 1.273 V. The temperature was 32 °C, and the electrode rotation rates were 157 rad s⁻¹.

of an Al plating bath so that the maximum plating rate might be maintained during processing without encountering the limitations arising from the anode reaction. As Fig. 3.2.2 clearly implies, j_{crit} is clearly dependent on the ionic liquid composition and temperature. An example of a plot of j_{crit} versus composition at a fixed temperature and rotation rate is shown in Fig. 3.2.3. Not surprisingly, active dissolution of the anode proceeds more effectively when the ionic liquid composition is closer to $x_{\text{Al}} = 0.50$. This is explained in part below. The parameter j_{crit} is likely to also depend significantly on other variables as well, including the convection rate, cell geometry and/or current distribution. Thus, it will probably be necessary to experimentally determine this parameter for the practical plating cell under consideration.

The limiting current densities, j_l , in Fig. 3.2.2 were also investigated at $\eta = 1.0$ V as a function of the electrode rotation rate at a fixed temperature and ionic liquid composition. The resulting Levich plots are shown in Fig. 3.2.4, and the linearity of these plots clearly indicates that the passive current densities at all three Al RDEs are limited by mass transport. In a previous investigation of Al dissolution conducted in the $\text{LiAlBr}_4\text{-NaAlCl}_4\text{-KAlCl}_4$ molten salt,³¹ we posited that the passive layer probably consists of a thin blocking layer of $\text{AlX}_3(\text{s})$ ($\text{X} = \text{Cl} + \text{Br}$) on the Al surface as the electrode diffusion layer becomes rich in this anodization product, and its solubility in the molten salt is exceeded. For the present case, this process can be represented by the reactions



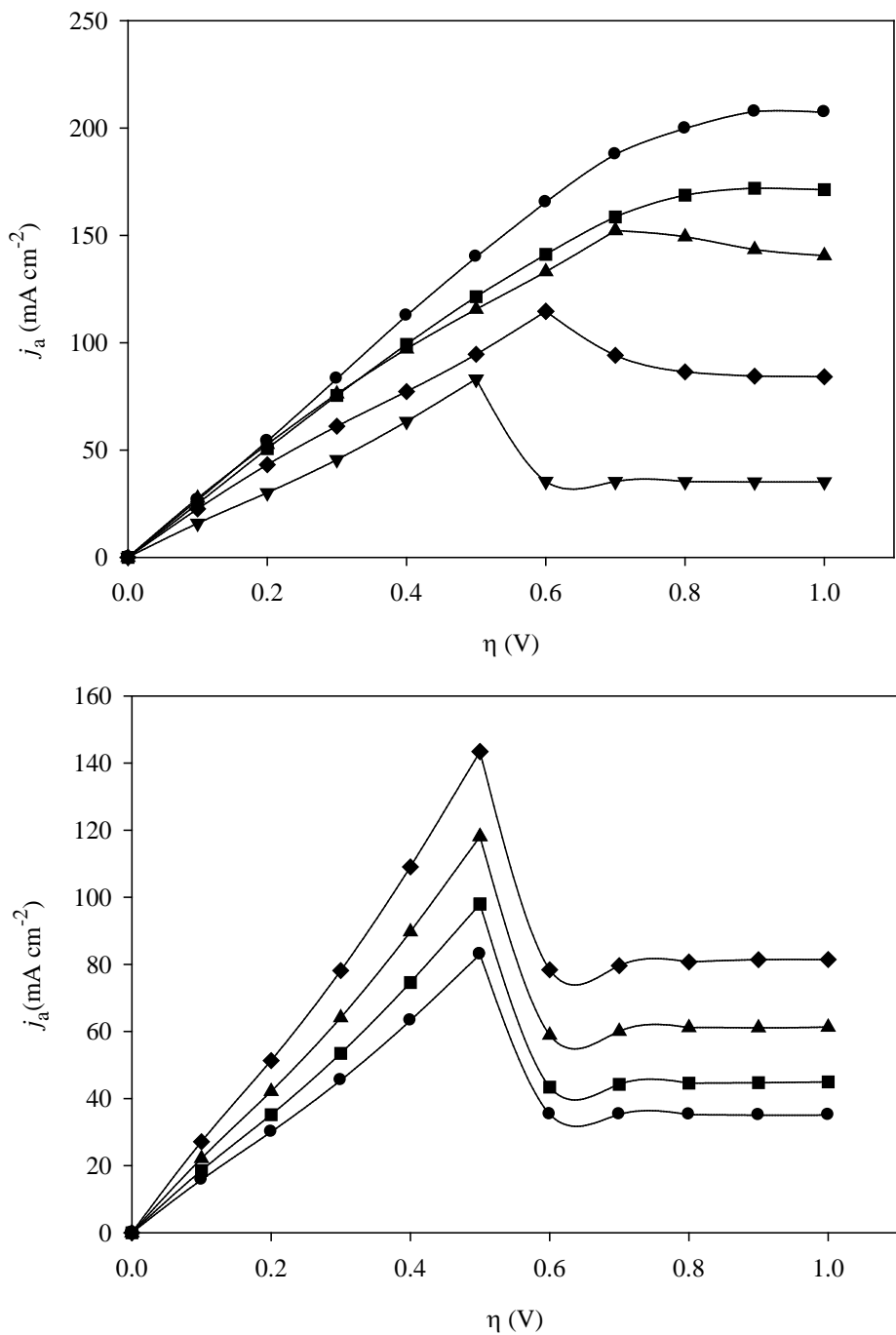


Figure 3.2.2: Current-sampled voltammograms constructed from data similar to that shown in Fig. 3.2.1 for Electrode A, but at different ionic liquid compositions and temperatures: (a) 32 °C; (●) 51 m/o, (■) 54 m/o, (▲) 58 m/o, (◆) 62 m/o, and (▼) 65 m/o AlCl₃; (b) 65 m/o AlCl₃; (●) 32°C, (■) 41°C, (▲) 51°C, and (◆) 62°C. The electrode rotation rate was 157 rad s⁻¹.

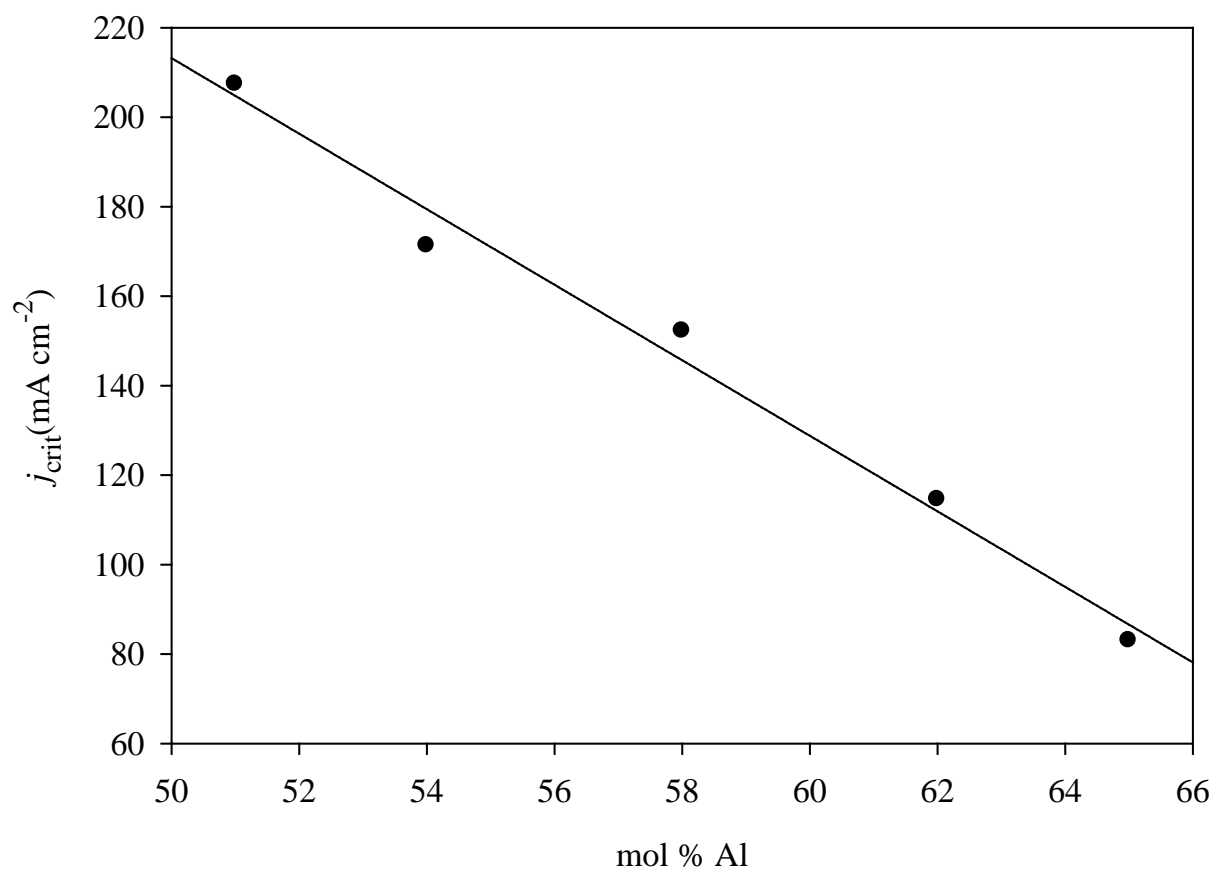


Figure 3.2.3: Plot of the critical current density, j_{crit} , versus the ionic liquid composition for Electrode A. The temperature was 32 °C, and the electrode rotation rate was 157 rad s⁻¹. The line is drawn to aid the eye.

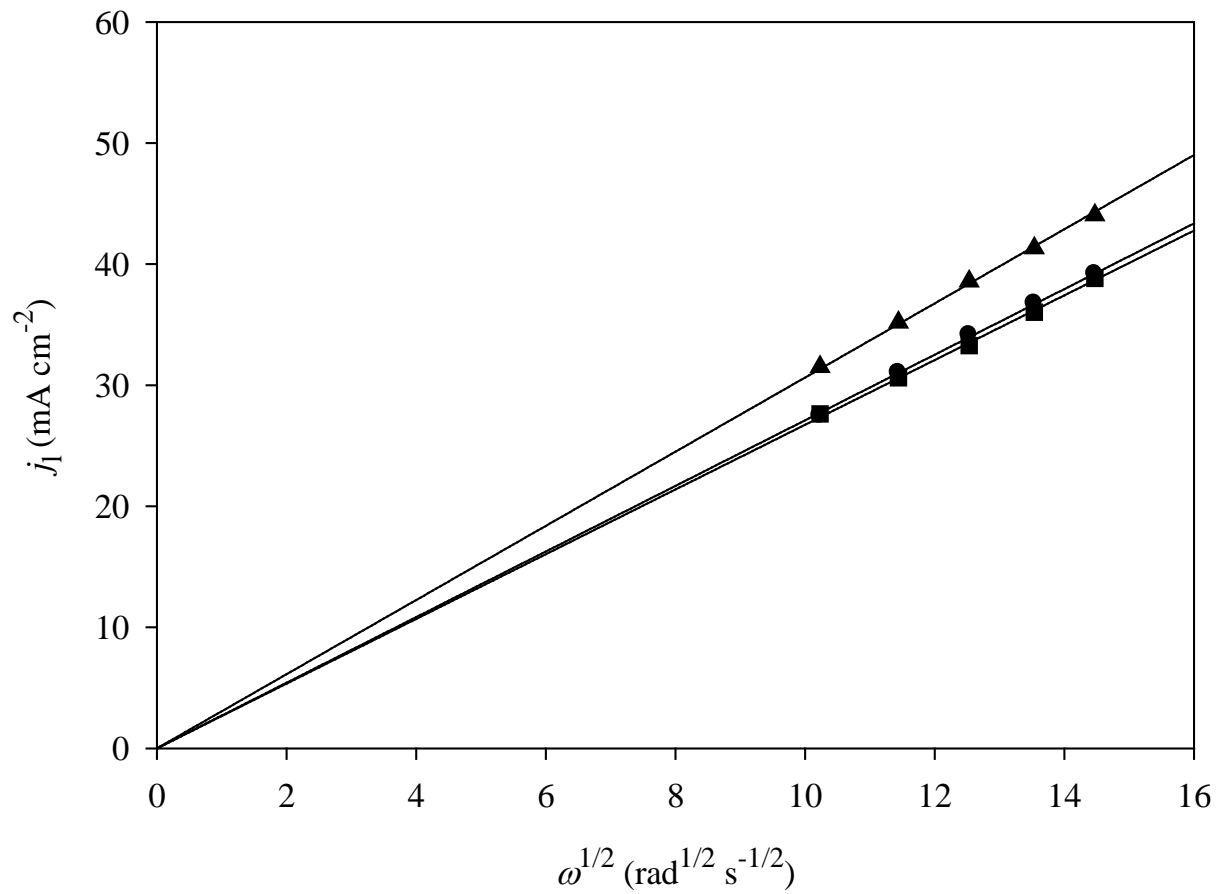


Figure 3.2.4: Levich plots for the passive limiting currents measured at (●) Electrode A, (■) Electrode B, and (▲) Electrode C in the 65 m/o ionic liquid at an anodic overpotential of 1.0 V. The temperature was 32 °C.

that when balanced together constitute the reaction in Eq. 1.1.3. It is a reasonable assumption that the accumulation of $\text{AlCl}_3(\text{s})$ on the electrode surface occurs because the supply of AlCl_4^- in the electrode diffusion layer becomes insufficient to convert all of the former into soluble Al_2Cl_7^- ions. (Note that Eq. 1.1.3 requires a total of seven AlCl_4^- ions overall to accommodate the three-electron oxidation of just one Al atom.) Thus, the limiting current is observed because the effective concentration of AlCl_4^- at the electrode surface is zero. If this is indeed the case, then at a fixed angular frequency, the steady-state or limiting current should show some regular dependence on the concentration of AlCl_4^- , although as pointed out previously,¹ the Levich equation may not otherwise be strictly applicable in this case.

The bulk concentration of AlCl_4^- , $C_{\text{AlCl}_4^-}^*$, in the units of mol cm^{-3} can be readily calculated from the expression

$$C_{\text{AlCl}_4^-}^* = \rho(2 - 3x_{\text{Al}})/[1000(0.1466 - 0.0133x_{\text{Al}})] \quad [3.2.3]$$

where ρ is the density of the acidic $\text{AlCl}_3\text{-EtMeImCl}$ ionic liquid at the specified temperature and ionic liquid composition. The density information required for this calculation can be found in the classical paper by Fannin, et al.⁶³ A complication associated with this approach is that the kinematic viscosity of the ionic liquid also changes with x_{Al} , which will influence the limiting current in two ways. First, the solution viscosity affects the diffusion layer thickness. Second, provided that the hydrodynamic radius of the diffusing species remains constant with changes in x_{Al} , the diffusion coefficient of the reacting species is itself inversely proportional to the solution viscosity. Thus, a strict comparison between j_l and $C_{\text{AlCl}_4^-}^*$ must also take into account the

changes in the viscosity attendant to the variation of x_{Al} . By combining the Stokes-Einstein equation

$$D = kT/6\pi\nu\rho r_s \quad [3.2.4]$$

where D is the diffusion coefficient, ν is the kinematic viscosity of the ionic liquid, and r_s is the hydrodynamic radius of the diffusing species, with the Levich equation, a “viscosity corrected” limiting current density, j_l' , can be defined as

$$j_l' = j_l\nu^{5/6}\rho^{2/3}\omega^{-1/2} = 1.860F(kT/6\pi r_s)^{2/3} C_{AlCl_4}^* \quad [3.2.5]$$

Datta and Vercruysse⁶⁷ used a similar approach in a study of the transpassive dissolution of steel in concentrated aqueous acids with different viscosities. A plot of j_l' versus $C_{AlCl_4}^*$, is shown in Fig. 3.2.5. This plot clearly exhibits a linear relationship between these variables with $j_l' \rightarrow 0$ as $C_{AlCl_4}^* \rightarrow 0$. This result lends strong support to a mechanism involving Eq. 3.2.1 and 3.2.2 in which the passive current is limited by the convective mass transport of $AlCl_4^-$ to the electrode surface. Although this is certainly the most appealing explanation, the results in Fig. 3.2.5 do not preclude the fact that the diffusion of the $Al_2Cl_7^-$ product away from the electrode may be an equally important determinant of the steady-state current because the concentrations of these two species are inseparably related by the stoichiometric expression

$$C_{AlCl_4}^*/C_{Al_2Cl_7}^* = (2 - 3x_{Al})/(2x_{Al} - 1) \quad [3.2.6]$$

Because $\text{AlCl}_3(\text{s})$ is a very effective electrical insulator, this finding also suggests that the resulting electrode surface layer must be porous or spongy. The sharp peak-like drop in the current density seen in Fig. 3.2.1 just before the onset of the steady-state passive current may be due to the initial formation of a non-porous, insulating layer of $\text{AlCl}_3(\text{l})$, which then quickly solidifies into a permeable layer of $\text{AlCl}_3(\text{s})$.

3.2.4 Dissolution of Al under Active Conditions

As shown in Fig. 3.2.2, at smaller overpotentials, i.e., ≤ 0.40 V, the oxidation of Al appears to proceed without the intermediate formation of a passive-like layer. We investigated the dissolution of Al in this potential region at each of the three RDE electrodes by applying different overpotentials and rotation rates. Levich plots were constructed from the resulting data, and examples are shown in Fig. 3.2.6. Although these plots are mostly linear, it is obvious that they do not pass through the origin. This data is typical of that seen for the anodic dissolution of metals under mixed kinetic/mass transport control,⁴⁴ and is very similar to that reported for the anodic dissolution of Al in $\text{LiAlBr}_4\text{-NaAlCl}_4\text{-KAlCl}_4$ (30-50-20 m/o).³¹

Information about the kinetics of the dissolution reaction can be extracted from this data by constructing Koutecky-Levich plots, i.e., plots of j_a^{-1} versus $\omega^{-1/2}$

$$j_a^{-1} = j_k^{-1} + [k_c / (k_a - k_c C_{\text{Al}^{3+}}^*)] [0.537(FD^{2/3})^{-1} \nu^{1/6}] \omega^{-1/2} \quad [3.2.7]$$

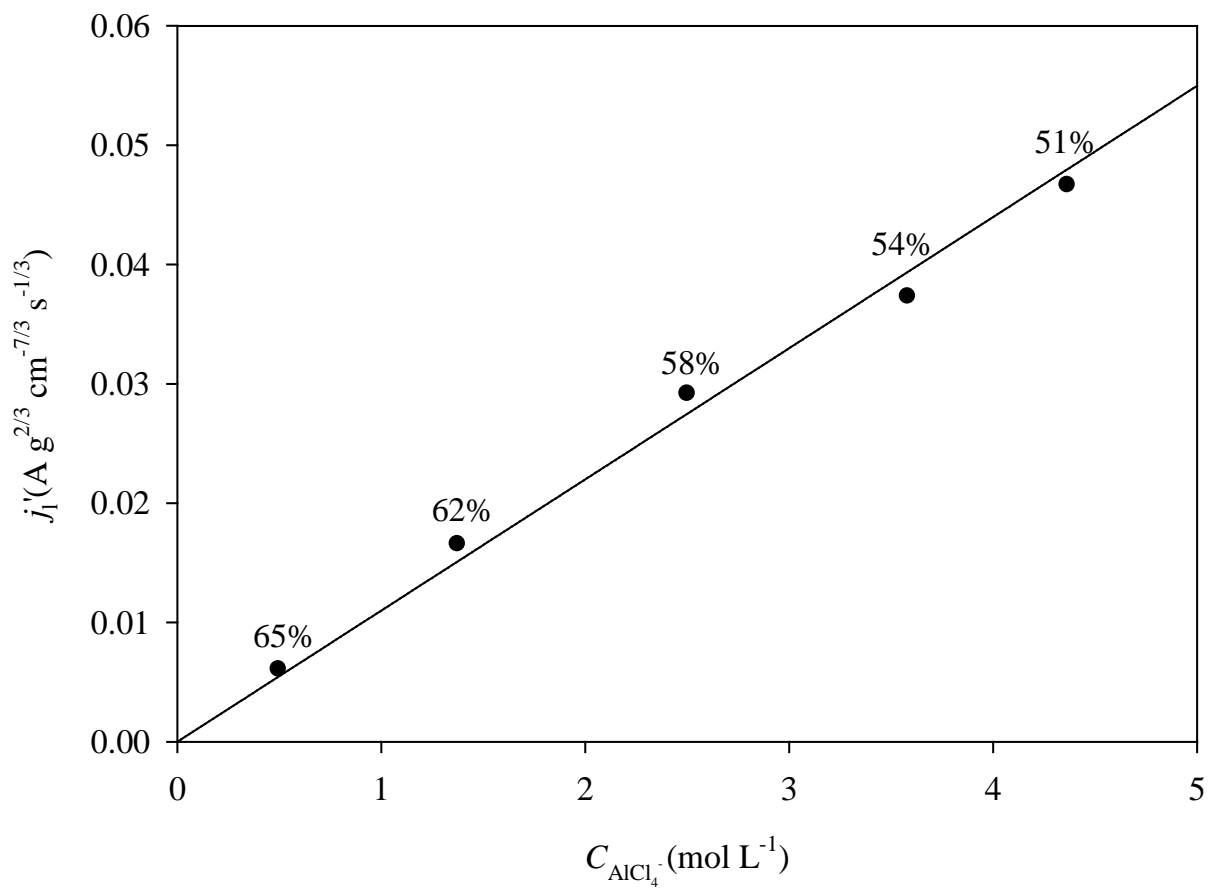


Figure 3.2.5: Viscosity-corrected passive limiting current densities versus the AlCl_4^- concentration for Electrode A. In each case, the temperature was 32 °C, and the electrode rotation rate was 157 rad s⁻¹. The limiting currents were measured at an anodic overpotential of 1.0 V.

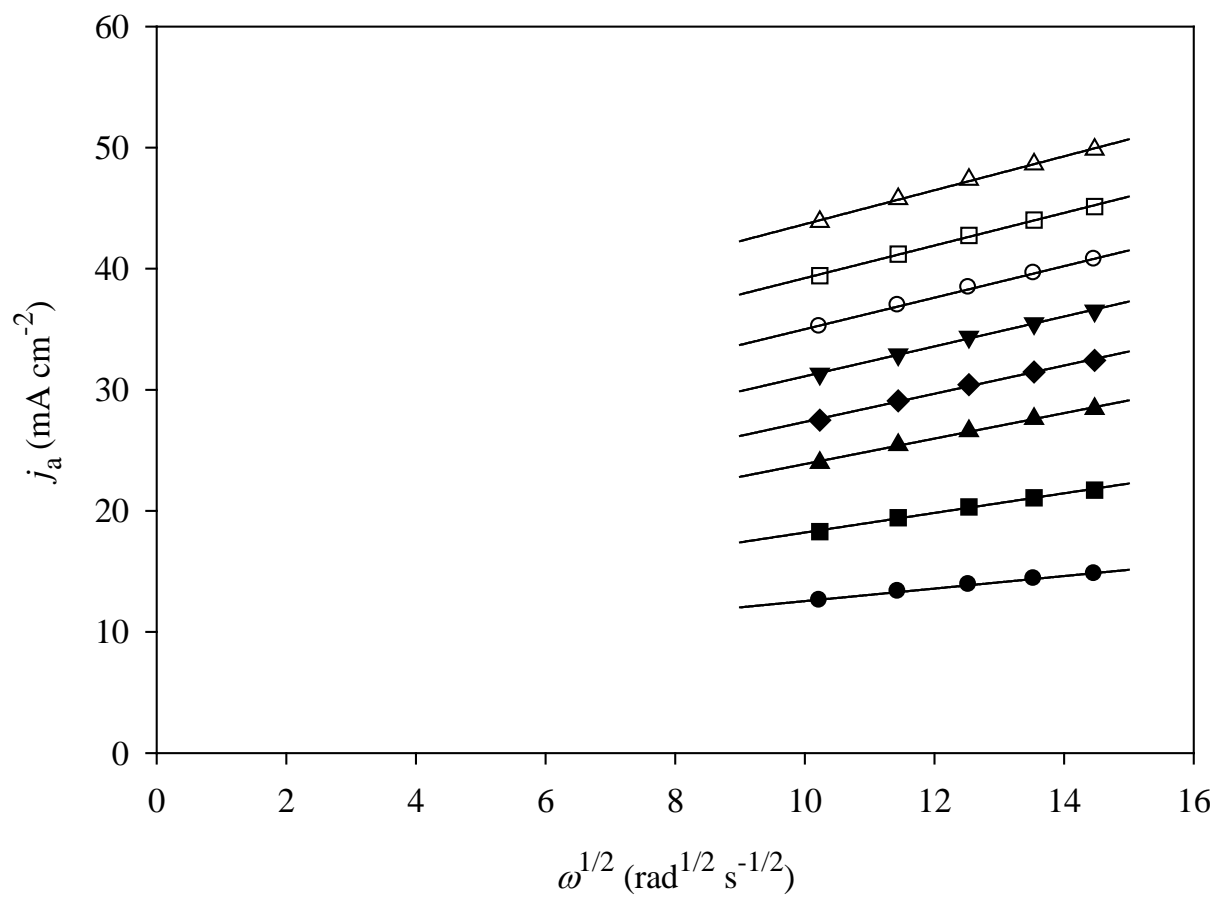


Figure 3.2.6(A): Example of Levich plots for the anodization of Electrode A at 32°C in the 65 m/o ionic liquid. The currents were sampled at 300 s. The anodic overpotentials were: (●) 0.053 V, (■) 0.082 V, (▲) 0.111 V, (◆) 0.130 V, (▼) 0.144 V, (○) 0.160 V, (□) 0.174 V, and (△) 0.190 V.

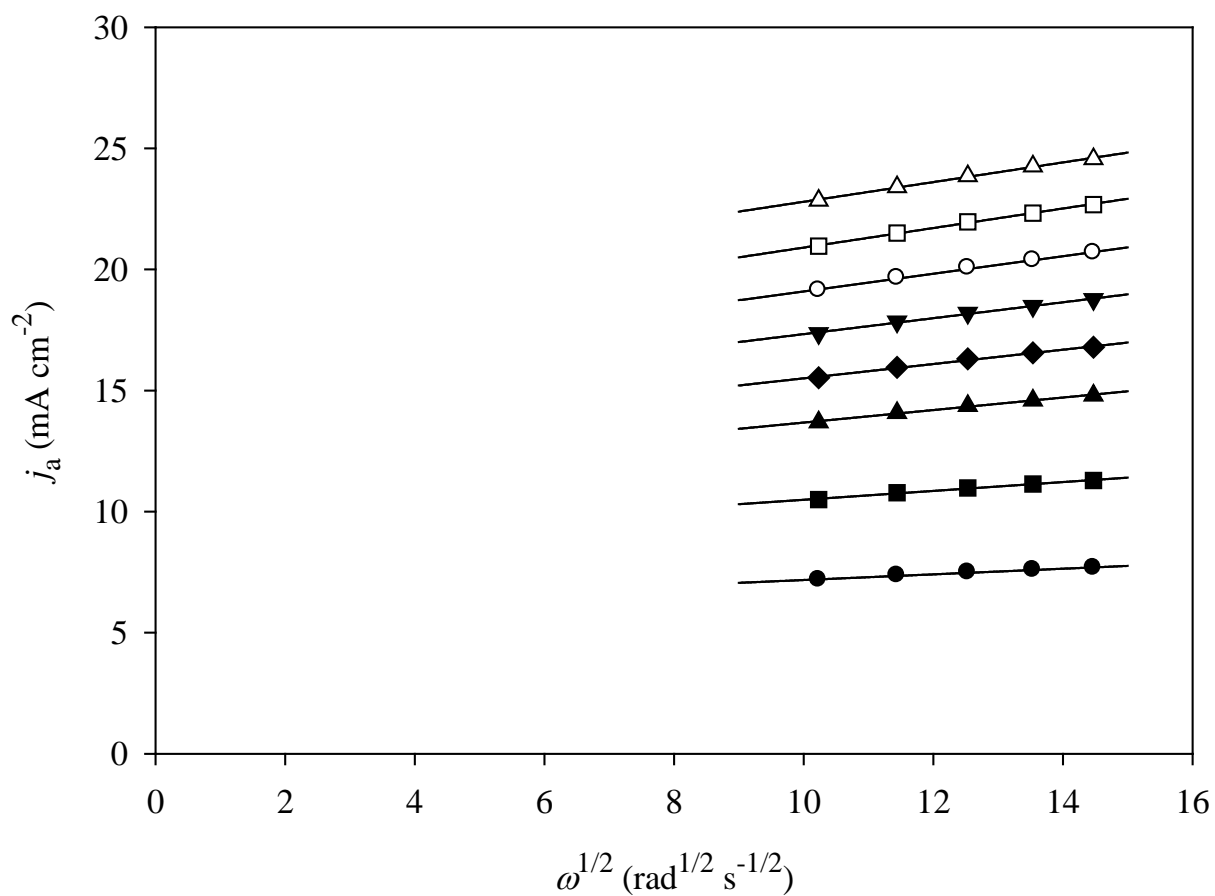


Figure 3.2.6(B): Example of Levich plots for the anodization of Electrode B at 32°C in the 65 m/o ionic liquid. The currents were sampled at 300 s. The anodic overpotentials were: (●) 0.025 V, (■) 0.040 V, (▲) 0.055 V, (◆) 0.065 V, (▼) 0.075 V, (○) 0.086 V, (□) 0.097 V, and (△) 0.108 V.

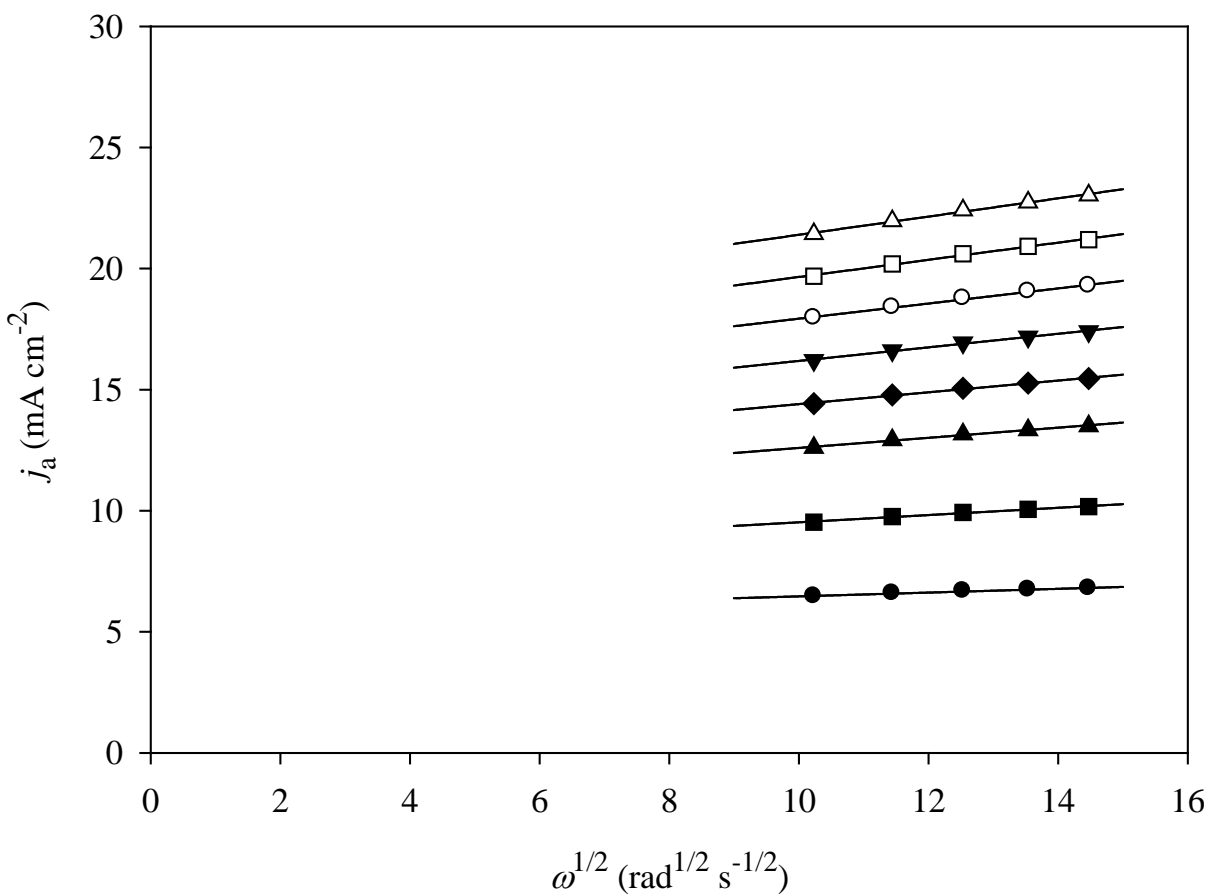


Figure 3.2.6(C): Example of Levich plots for the anodization of Electrode C at 32°C in the 65 m/o ionic liquid. The currents were sampled at 300 s. The anodic overpotentials were: (●) 0.028 V, (■) 0.043 V, (▲) 0.058 V, (◆) 0.068 V, (▼) 0.078 V, (○) 0.088 V, (□) 0.098 V, and (△) 0.108 V.

where the inverse of the intercept of these plots, $j_k = 3F(k_a - k_c C_{\text{Al}^{3+}}^*)$. In this expression, k_a and k_c are the potential-dependent anodic and cathodic heterogeneous rate constants, respectively, and $C_{\text{Al}^{3+}}^*$ is the formal concentration of the reducible Al(III) species in the ionic liquid. Example plots for each electrode based on the corresponding Levich plots are shown in Fig. 3.2.7. Because of contributions to the net current density from the back reaction, i.e., Eq. 1.1.6, it was necessary to construct graphs of $\log j_k$ versus η , i.e., classical Tafel plots, to determine the exchange current density, j_0 , by extrapolation of the linear portions of these graphs to $\eta = 0$

$$\log j_k = \log j_0 + \alpha_a F \eta / 2.303 RT \quad [3.2.8]$$

Examples of these graphs with the extrapolated anodic Tafel lines are shown in Fig. 3.2.8 and 3.2.9. Each data point was carefully corrected for the iR drop in the solution. The slopes of these plots, $\partial \log j_k / \partial \eta$, also give information about the apparent anodic transfer coefficient, α_a .⁶² The value of j_0 obtained from this extrapolation is directly related to the heterogeneous anodic rate constant, referenced to $\eta = 0$, or E_{eq} and defined here as $k_{a,0}$, by the relationship $j_0 = 3Fk_{a,0}$.

The resulting values of j_0 , α_a , and $k_{a,0}$ for each of the three electrodes in four to five different ionic liquid compositions are given in Table 3.2.1. Although there is unavoidable scatter in the data collected in this table due to the inherent inaccuracies associated with the extrapolation needed to avoid the very facile back reaction, it is a reasonable conclusion that j_0 is about the same for the two large disk electrodes, Electrodes B and C, but significantly larger for the small annealed wire electrode, Electrode A. It is not clear if these results reflect structural differences in the Al used to fabricate these electrodes. Thus, we have examined each of the

electrodes with Electron Backscatter Diffraction (EBD), and the results are given in the next section.

The data in this table do not seem to show any obvious dependence of j_0 on the ionic liquid composition at any of the three electrodes, within the experimental precision of these measurements. The implication of this result seems to be that neither AlCl_4^- nor Al_2Cl_7^- ions are directly involved in the rate-determining step of the fundamental Al dissolution process. In addition, the apparent anodic transfer coefficient is close to zero in all of the measurements. Although this result defies ready interpretation, similar small α_a values were found during an investigation of the Al dissolution reaction in the $\text{LiAlBr}_4\text{-NaAlCl}_4\text{-KAlCl}_4$ (30-50-20 m/o) molten salt at $t > 100$ °C. The microscopic pathway for the dissolution of Al in chloroaluminates is without doubt very complex. However, the application of techniques beyond the classical electrochemical methods used in this investigation will likely be required to fully realize this mechanism.

In order to estimate the apparent activation energy, $\Delta G_{a,0}^\ddagger$, for this anodic reaction under the described conditions, we determined j_0 at several additional temperatures at each ionic liquid composition by using the same experimental procedures described above. As noted previously, the temperature range accessible with the Teflon-shrouded disk electrodes is very limited because these electrodes are easily damaged by heating above ~ 60 °C, and the small temperature range available for experiments with these electrodes degraded the precision of these results. However, Electrode A could be used over a wider temperature range, and so we report only this data here. Because the experimental data were very similar to those obtained at 32 °C, and for reasons of space and repetition, the numerous Tafel plots are not reproduced here. Arrhenius

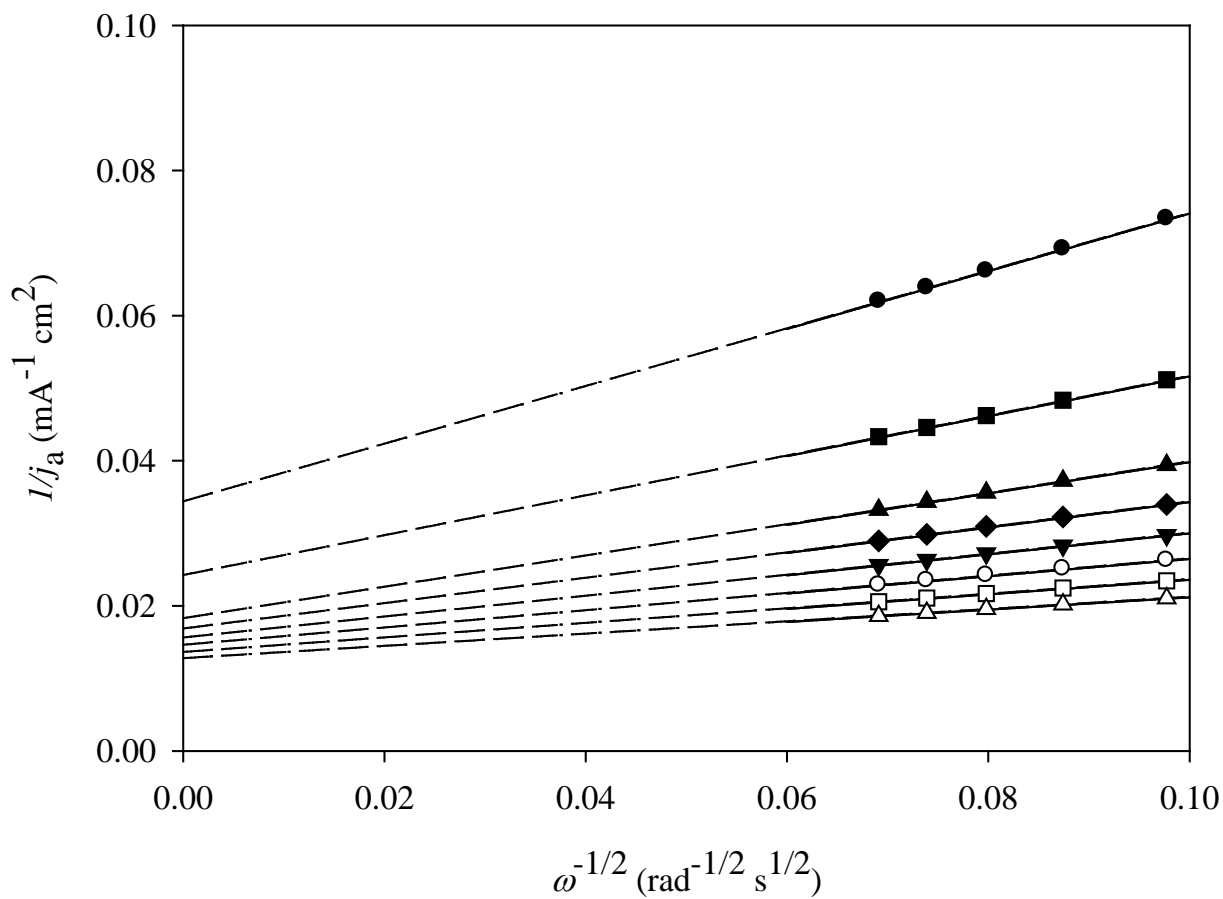


Figure 3.2.7(A): Example of Koutecky-Levich plots for Electrode A constructed from the data in Fig. 3.2.6(A): The anodic overpotentials were the same as those given in this figure. The dashed lines are drawn to aid the eye.

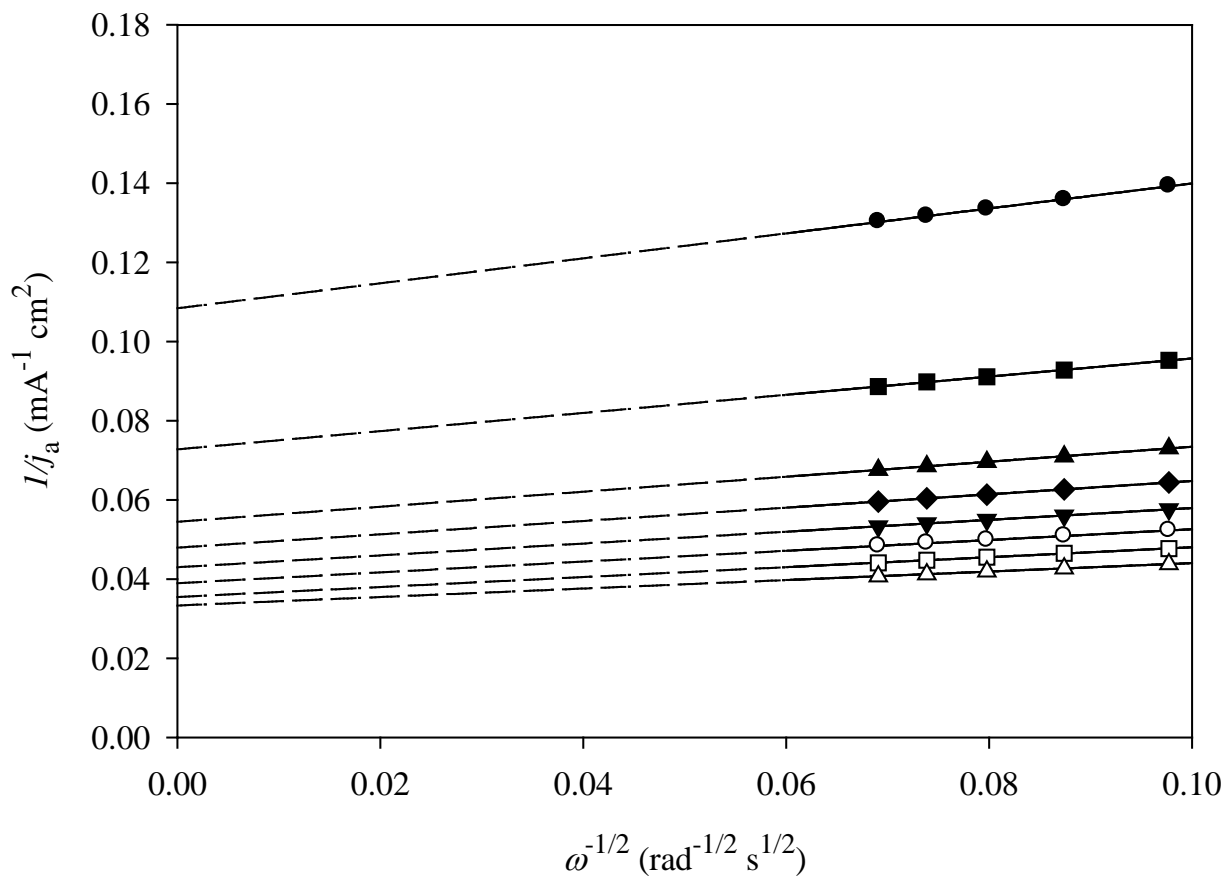


Figure 3.2.7(B): Example of Koutecky-Levich plots for Electrode B constructed from the data in Fig. 3.2.6(B): The anodic overpotentials were the same as those given in this figure. The dashed lines are drawn to aid the eye.

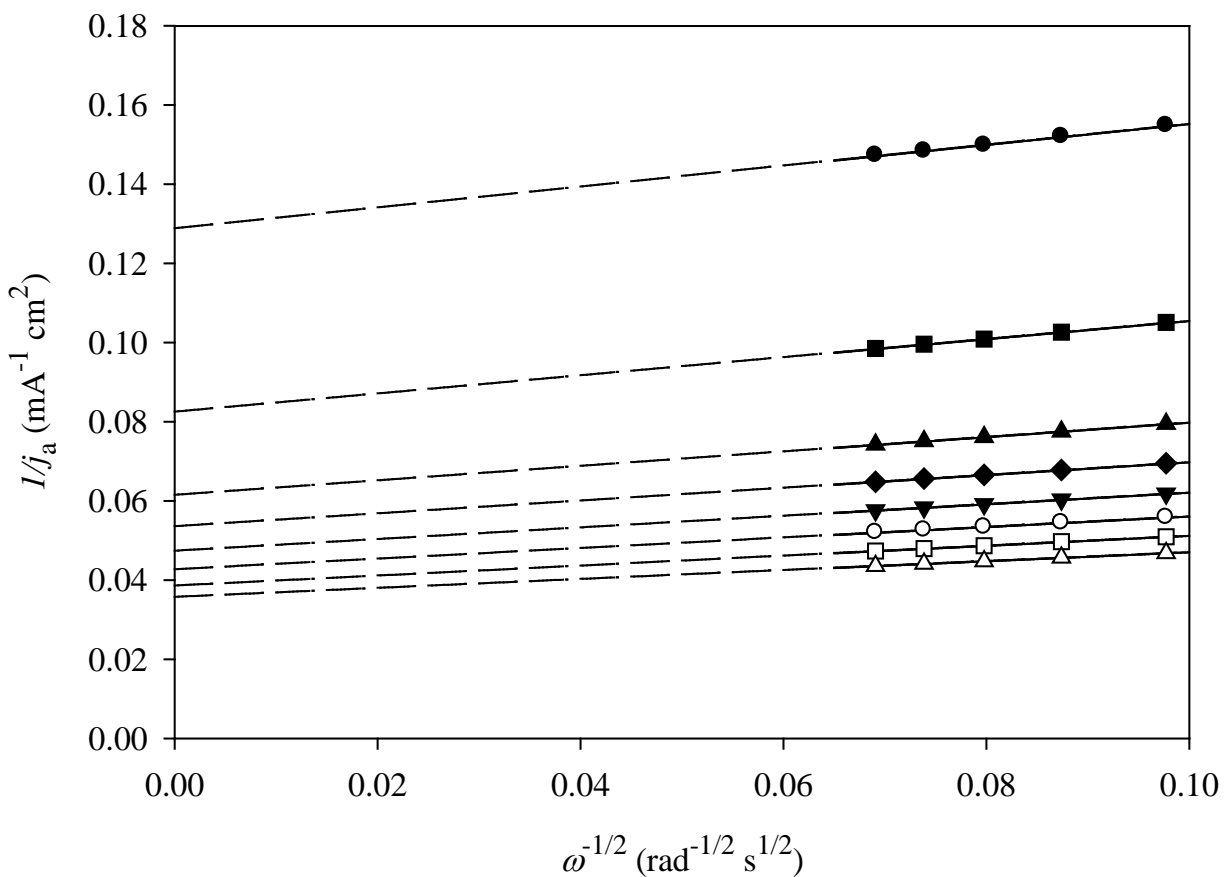


Figure 3.2.7(C): Example of Koutecky-Levich plots for Electrode C constructed from the data in Fig. 3.2.6(C): The anodic overpotentials were the same as those given in this figure. The dashed lines are drawn to aid the eye.

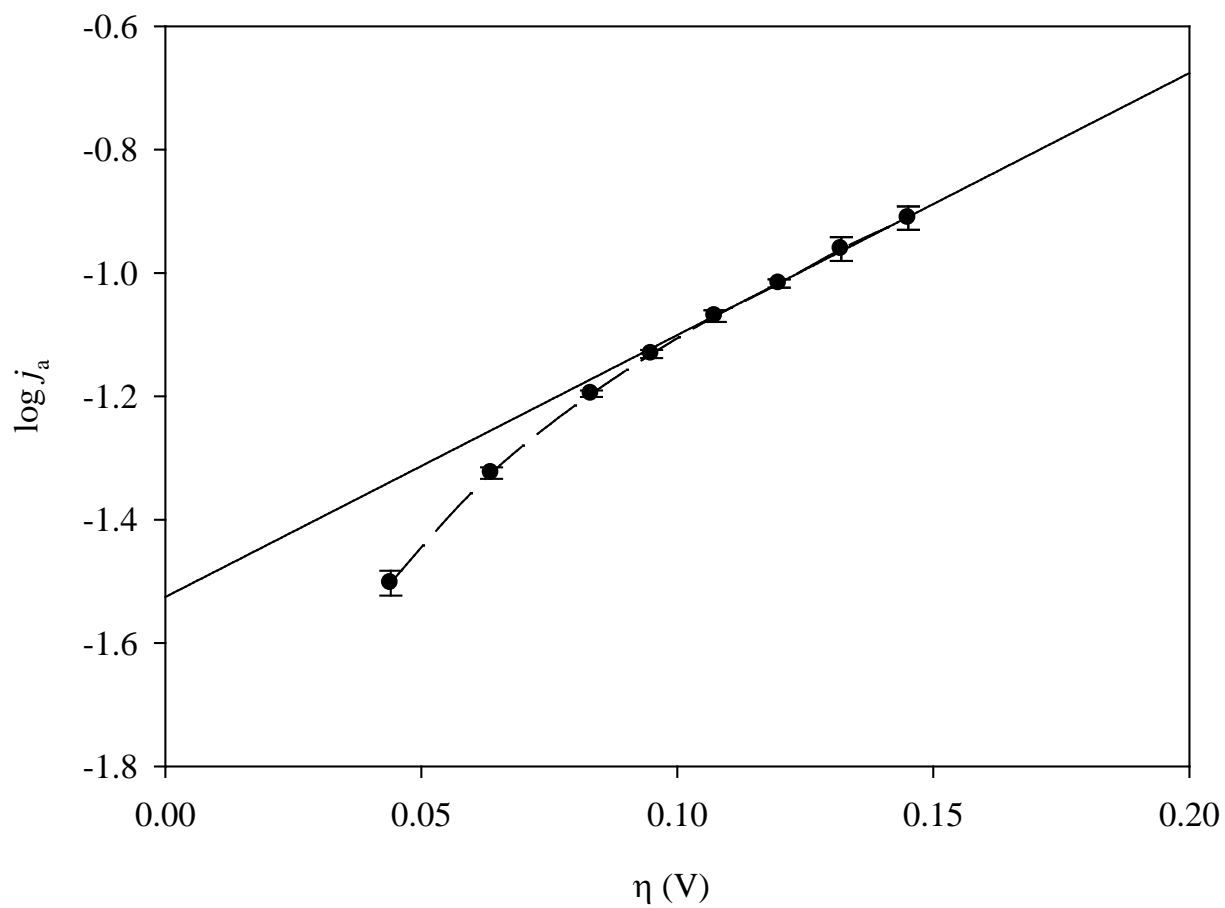


Figure 3.2.8(A): Example of a Tafel plot for Electrode A prepared from the data in Fig. 3.2.7(A). The error bars represent the 95 % C.I. The dashed line is drawn to aid the eye.

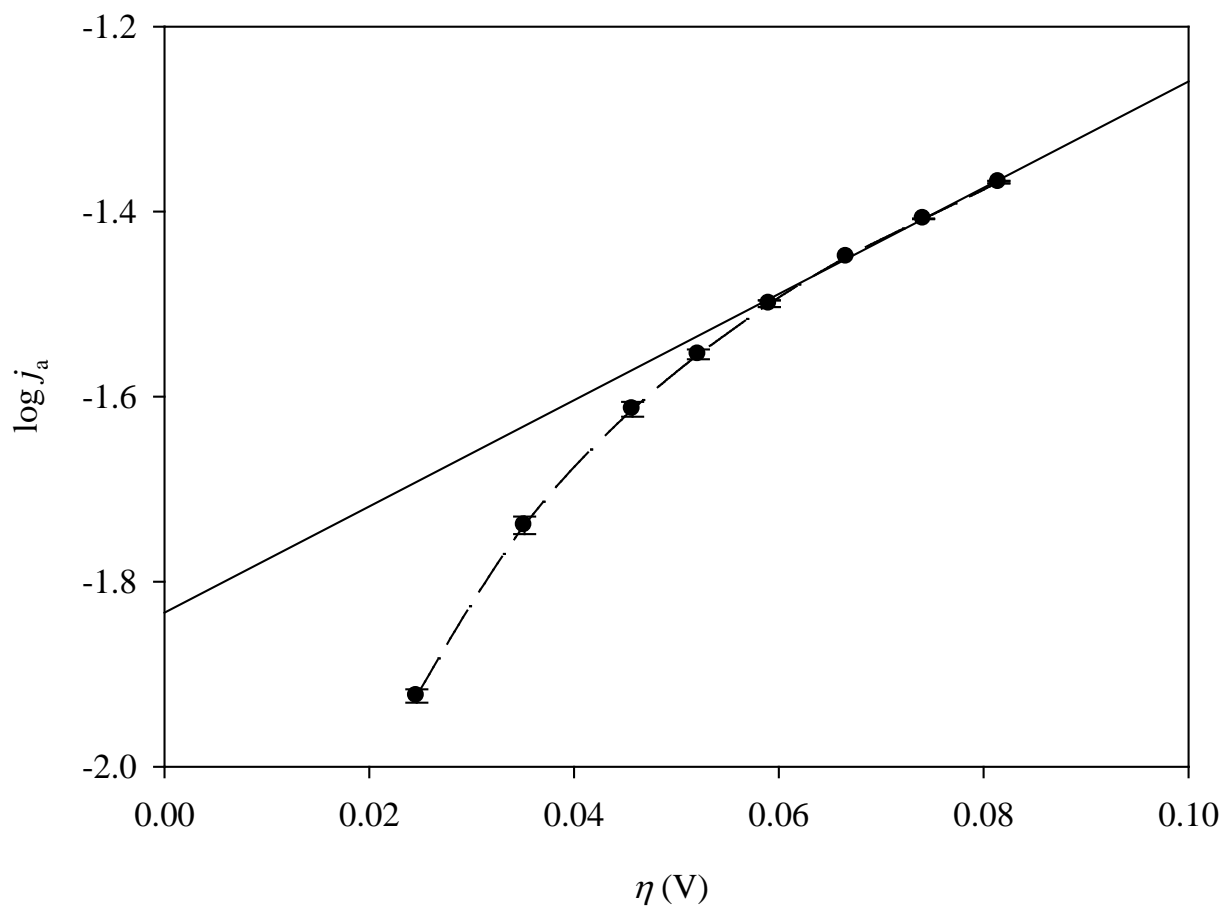


Figure 3.2.8(B): Example of a Tafel plot for Electrode B prepared from the data in Fig. 3.2.7(B). The error bars represent the 95 % C.I. The dashed line is drawn to aid the eye.

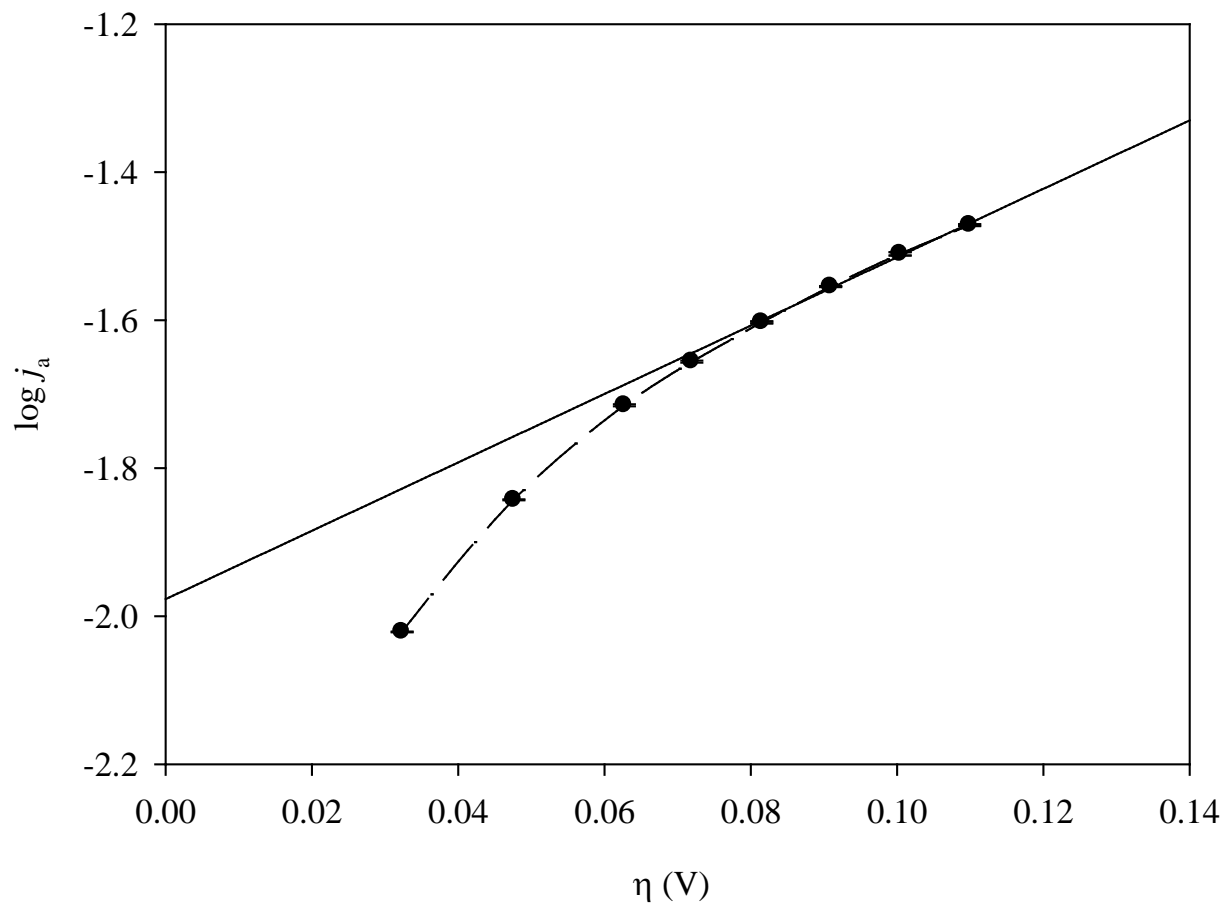


Figure 3.2.8(C): Example of a Tafel plot for Electrode C prepared from the data in Fig. 3.2.7(C). The error bars represent the 95 % C.I. The dashed line is drawn to aid the eye.

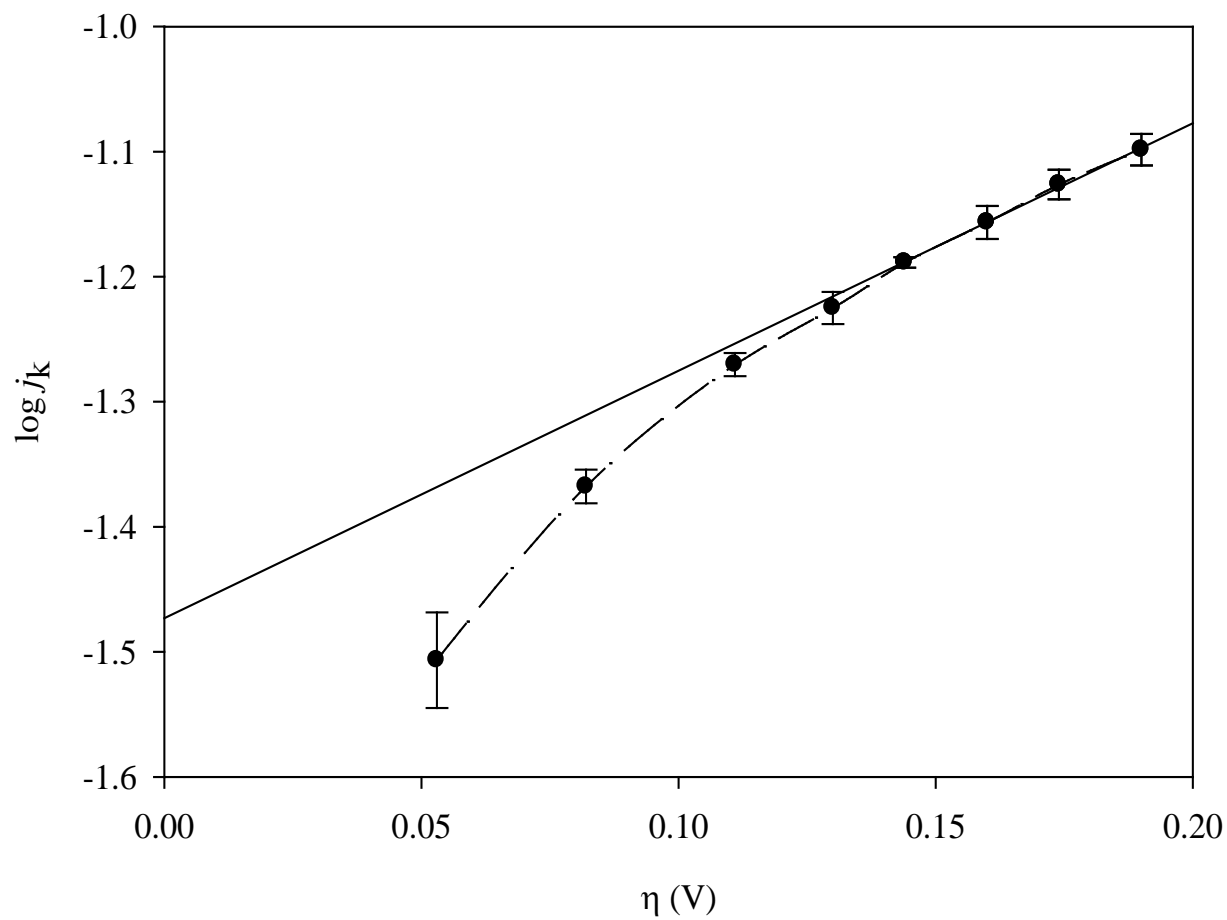


Figure 3.2.9(A): Example of a Tafel plot for Electrode A prepared from data recorded in the 54 m/o ionic liquid.

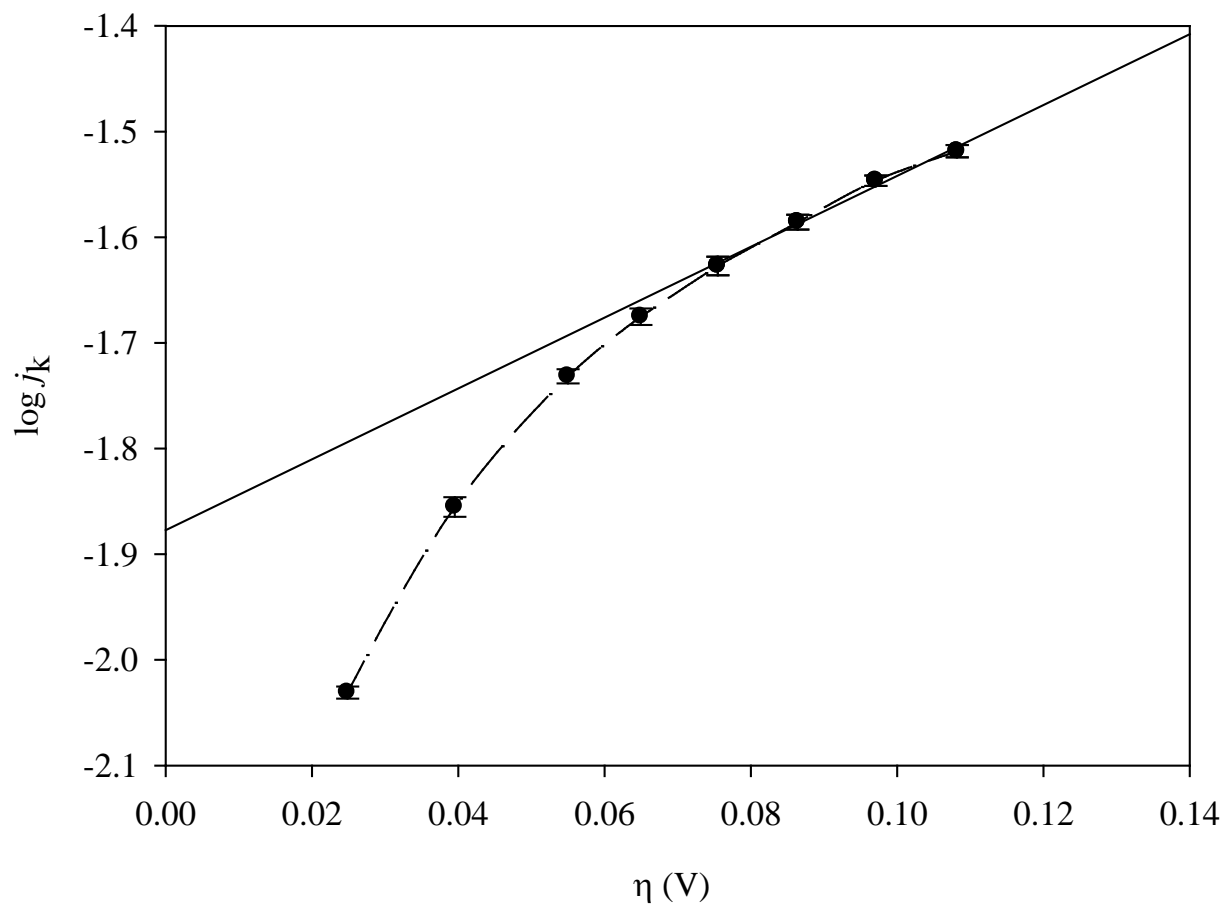


Figure 3.2.9(B): Example of a Tafel plot for Electrode B prepared from data recorded in the 54 m/o ionic liquid.

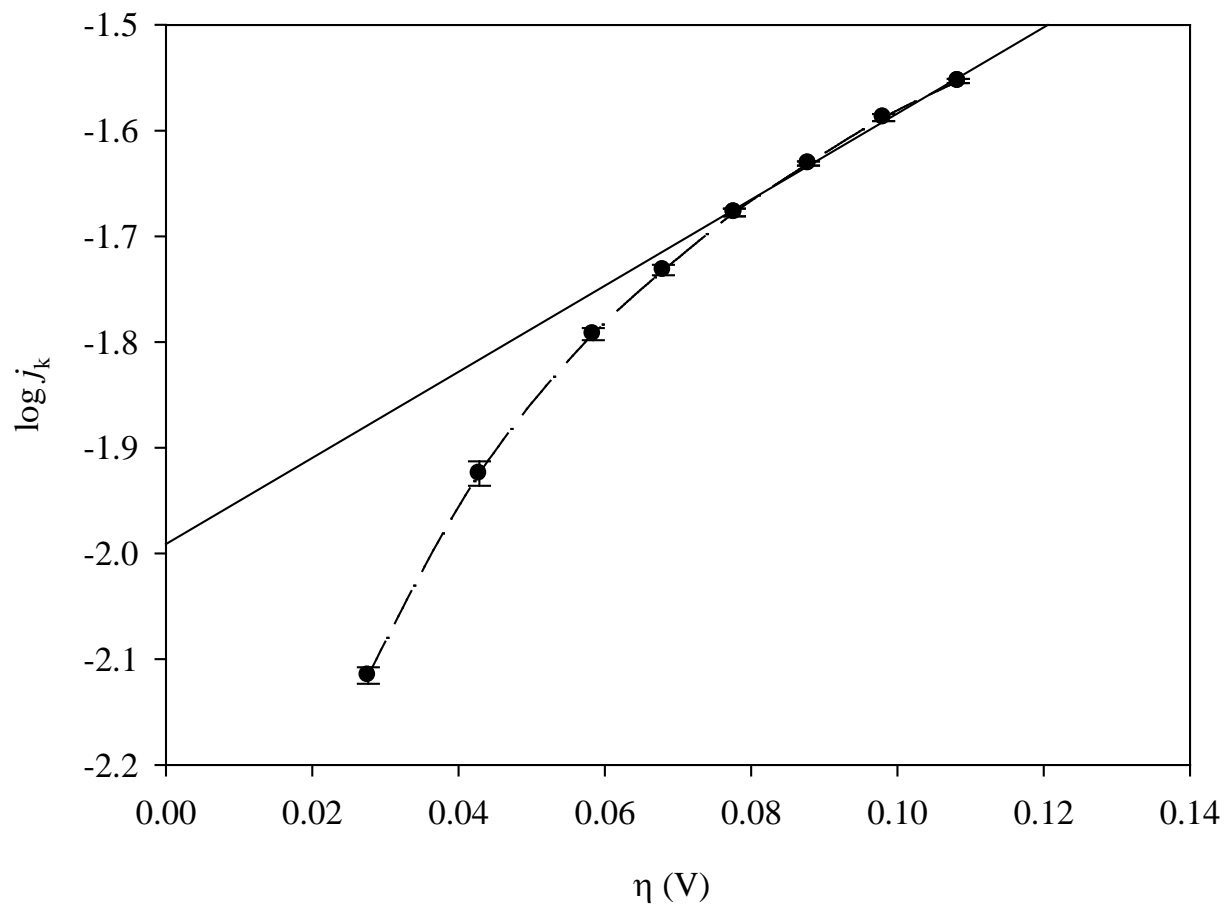


Figure 3.2.9(C): Example of a Tafel plot for Electrode C prepared from data recorded in the 54 m/o ionic liquid.

plots of $\log j_0$ versus $1/T$ that were constructed from this data were linear, and $\Delta G_{a,0}^\#$ was estimated from the slopes of these plots with the expression⁴⁶

$$\Delta G_{a,0}^\# = -2.303R[\partial \log j_0 / \partial (1/T)] \quad [3.2.9]$$

The resulting values of $\Delta G_{a,0}^\#$ are collected in Table 3.2.1. Within the precision of these results, there does not seem to be an obvious dependence of $\Delta G_{a,0}^\#$ on the ionic liquid composition. Interestingly, the average value of $\Delta G_{a,0}^\#$ measured for Electrode A at much higher temperatures in the $\text{LiAlBr}_4\text{-NaAlCl}_4\text{-KAlCl}_4$ molten salt, 17.1 kJ mol^{-1} ,¹³ lies inside the 95 % C.I. for this same electrode in $\text{AlCl}_3\text{-EtMeImCl}$, $17.8 \pm 0.7 \text{ kJ mol}^{-1}$.

3.2.5 Electron Backscatter Diffraction

In an effort to determine why the kinetic results obtained at the wire electrode were substantially different from those observed at the two larger disk electrodes, the electrode materials were subjected to structural analysis with Electron Backscatter Diffraction (EBSD) as described in the Experimental section. Figure 10 shows the inverse pole maps and the pole figures of the three aluminum electrodes that were examined in cross-section; (a) electrode A (2-mm diameter aluminum wire), (b) electrode B (Pine Instruments RDE), and (c) electrode C (in-house, 6 mm diam Al rod). The pole figures show similar 100 fiber texture aligned with the wire/rod axis for all three electrodes. The 110 and 111 pole figures demonstrate the axisymmetry expected in a drawn or extruded wire or rod. While the 100 pole figure for electrode C has a

Table 3.2.1: RDE results for the anodization of Al in the AlCl₃-EtMeImCl ionic liquid.

| | | 31 °C | | 41 °C | | 51 °C | | 61 °C | | |
|---------------------------------|-------------------|------------------------|------------|------------------------|------------|------------------------|------------|------------------------|------------|--------------------------------------|
| | mol % | log j_0 | α_a | ΔG^0 (kJ mol ⁻¹) |
| | AlCl ₃ | | | | | | | | | |
| Electrode A | 51% | -1.622 | 0.107 | -1.505 | 0.093 | -1.403 | 0.096 | -1.356 | 0.097 | 17.6 |
| | 54% | -1.525 | 0.111 | -1.364 | 0.100 | -1.294 | 0.097 | -1.217 | 0.098 | 19.4 |
| | 58% | -1.445 | 0.147 | -1.248 | 0.107 | -1.187 | 0.098 | -1.164 | 0.093 | 17.6 |
| | 62% | -1.294 | 0.065 | -1.153 | 0.063 | -1.132 | 0.071 | -1.015 | 0.063 | 16.8 |
| | 65% | -1.473 | 0.052 | -1.412 | 0.061 | -1.293 | 0.056 | -1.195 | 0.052 | 18.7 |
| | avg | | -1.472 | 0.096 | -1.336 | 0.085 | -1.262 | 0.084 | -1.189 | 0.081 |
| 95 % CI | | 0.11 | | 0.12 | | 0.09 | | 0.11 | | 0.9 |
| $k_{a,0}$ (cm s ⁻¹) | | 1.2 x 10 ⁻⁷ | | 1.6 x 10 ⁻⁷ | | 1.9 x 10 ⁻⁷ | | 2.2 x 10 ⁻⁷ | | |
| Electrode B | 51% | * | * | * | * | * | * | * | * | * |
| | 54% | -1.834 | 0.151 | -1.798 | 0.154 | -1.689 | 0.174 | -1.644 | 0.176 | 13.3 |
| | 58% | -1.885 | 0.135 | -1.769 | 0.111 | -1.706 | 0.157 | -1.583 | 0.151 | 19.5 |
| | 62% | -1.883 | 0.083 | -1.766 | 0.101 | -1.650 | 0.104 | -1.525 | 0.079 | 23.3 |
| | 65% | -1.877 | 0.088 | -1.751 | 0.084 | -1.722 | 0.073 | -1.656 | 0.089 | 13.5 |
| | avg | | -1.870 | 0.114 | -1.771 | 0.113 | -1.692 | 0.127 | -1.602 | 0.124 |
| 95 % CI | | 0.024 | | 0.019 | | 0.030 | | 0.059 | | 4.772 |
| $k_{a,0}$ (cm s ⁻¹) | | 4.7 x 10 ⁻⁸ | | 5.9 x 10 ⁻⁷ | | 7.0 x 10 ⁻⁷ | | 8.6 x 10 ⁻⁸ | | |
| Electrode C | 51% | * | * | * | * | * | * | * | * | * |
| | 54% | -1.980 | 0.038 | -1.873 | 0.130 | -1.787 | 0.129 | -1.727 | 0.126 | 16.5 |
| | 58% | -1.945 | 0.164 | -1.850 | 0.143 | -1.759 | 0.144 | -1.702 | 0.208 | 16.0 |
| | 62% | -1.987 | 0.117 | -1.882 | 0.145 | -1.820 | 0.135 | -1.746 | 0.165 | 15.3 |
| | 65% | -1.991 | 0.106 | -1.848 | 0.098 | -1.806 | 0.114 | -1.710 | 0.096 | 17.3 |
| | avg | | -1.976 | 0.106 | -1.863 | 0.129 | -1.793 | 0.131 | -1.721 | 0.149 |
| 95 % CI | | 0.021 | | 0.017 | | 0.026 | | 0.019 | | 0.800 |
| $k_{a,0}$ (cm s ⁻¹) | | 3.7 x 10 ⁻⁸ | | 4.7 x 10 ⁻⁸ | | 5.6 x 10 ⁻⁸ | | 6.6 x 10 ⁻⁸ | | |

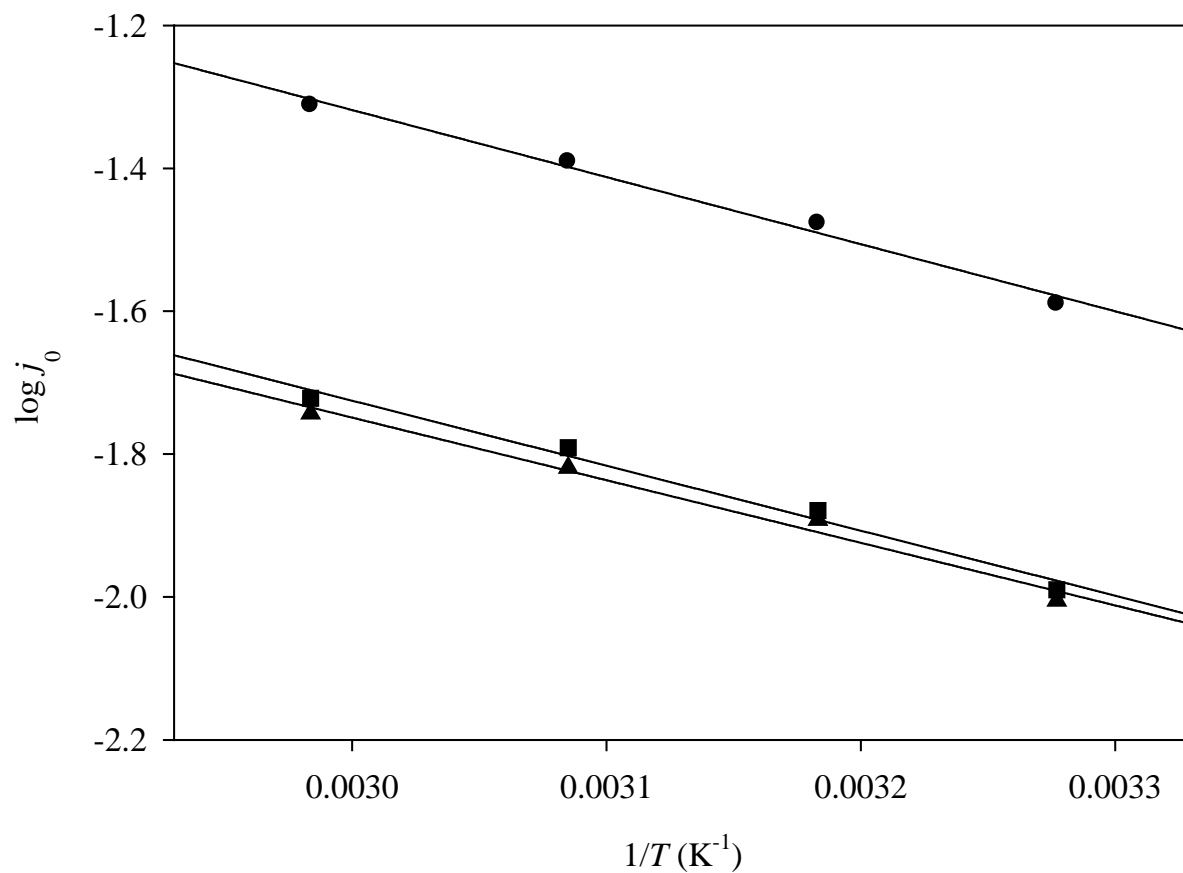


Figure 3.2.10: Example of Arrhenius plots for (●) Electrode A, (■) Electrode B, and (▲) Electrode C prepared from data recorded in the 54 m/o ionic liquid.

more intense peak, the small number of grains makes a quantitative comparison with the other electrodes unreliable. The grain structure of the small wires (electrode A) exhibits a bimodal distribution, with smaller grains embedded in larger grains. The wires appear to have been only partially annealed after drawing or extrusion, as indicated by the smaller grain size and areas of similar orientation, but with misorientation boundaries of 2° to 4° . Grains range in size from 4 to $340\ \mu\text{m}$, with an average size of $21\ \mu\text{m}$. Electrode B has a higher density of small grains, but some larger grains are also present. Grain sizes range from 4 to $200\ \mu\text{m}$, with an average size of $14\ \mu\text{m}$. The inverse pole map of electrode C is quite different from the other samples, showing a large, equi-axed grain structure. The grain size and shape, as well as the high degree of texture (the 100 axis aligned with the rod axis) indicate that this sample was fully annealed. Grain sizes in this sample range from 40 to $880\ \mu\text{m}$, with an average size of $90\ \mu\text{m}$.

In order to quantify the extent of possible work-hardening in the wire (A) sample, the microhardness was measured and compared to that of the large-grained sample (C). The average microhardness (H_v) for sample C was 17.69 ± 0.78 (one standard deviation), while for sample A was 19.44 ± 1.58 . The measured difference in microhardness is slight, and not statistically significant. The slight hardness differences imply that the small wires do not have a large degree of cold work and dislocations. Since smaller grain size typically increases hardness, this may be the primary cause for the small difference in hardness.

The EBSD analysis does not explain the enhanced dissolution kinetics of the sample (A) wire electrode. All three samples have a similar 100 fiber texture aligned with the wire/rod. Although the three samples appear to have different thermal history, based on the grain size distribution, the grain size alone does not correlate to the aluminum dissolution kinetics. At this

point we can only attribute the enhanced kinetics to artificially larger current densities at the miniature electrode as the result of edge effects.

3.2.6 Summary

At small anodic (positive) potentials, the anodization of aluminum in $\text{AlCl}_3\text{-EtMeImCl}$ ionic liquid proceeds under mixed kinetic and mass-transport control. At larger anodic potentials and higher oxidation rates, the anodization reaction transitions to a mass-transport limited process resulting from the formation of a steady-state passive layer of AlCl_3 on the Al electrode. Under conditions such as those encountered in a plating bath, the formation of this passive layer would significantly limit the overall rate of the cell reaction. Thus, because of these anode limitations, careful choices must be made about the temperature, ionic liquid composition, and applied potential when using this and related chloroaluminate ionic liquids for Al plating. In fact, for a given set of conditions, it is possible to define a critical current density above which the passivation is likely to be observed. Although the three Al samples examined in this investigation exhibited different dissolution kinetics and grain size, there was no obvious correlation between these properties.

3.3 Lewis Acid-Dependent Copper Anodization in the $\text{AlCl}_3\text{-EtMeImCl}$ Ionic Liquid

3.3.1 Cu anodization in Acidic Ionic Liquids

It was necessary to determine the formal potential, E^0 , of the reaction: $\text{Cu}^+ + \text{e}^- \leftrightarrow \text{Cu}$ electrode couple so as to provide a reference point for the calculation of the overpotential, $\eta = E_{\text{app}} - E_{\text{eq}}$. The open circuit potential (OCP), which is equivalent to E_{eq} , was measured for ionic

liquid with different Cu^+ concentrations, can be used to estimate $E^{0'}$ by using the well-known Nernst relation:

$$E_{eq} = E^{0'} + \frac{RT}{F} \ln C_{\text{Cu}^+} \quad [3.3.1]$$

A plot of E_{eq} versus $\ln C_{\text{Cu}^+}$ is shown below in Fig. 3.3.1. Based on Eq. 3.3.1 as discussed above, the intercept of this plot yields a preliminary measurement indicating that $E^{0'} = 0.86$ V. However, the slope of this plot is 0.035, and at the temperature of these experiments, the theoretical value should be 0.026. Figure 3.3.2 shows current-time plots resulting from Cu dissolution experiments that were carried out at a Cu-RDE using the same method that was used to study Al dissolution. These plots are similar to those observed for Al dissolution prior to the onset of electrode passivation. However, unlike the results for Al, passivation of the Cu surface does not seem to take place. However, there are suspicious minima associated with the CA plots that were recorded at larger overpotentials, Fig. 3.3.2(h, i, j).

A plot of $\log j$ versus the overpotential with j measured at 30s, is shown in Fig. 3.3.3. The shape of this Tafel plot is typical of that reported for Cu oxidation in aqueous solutions.³⁴ As was the case for Al, Levich plots that were prepared from data similar to that shown in this figure, but at different rotation rates, do not intersect the origin, signifying a reaction operating under mixed control. An example plot is shown in Fig. 3.3.4. This data was then evaluated by using the Koutecky-Levich equation for the case of the oxidation of Cu to Cu^+

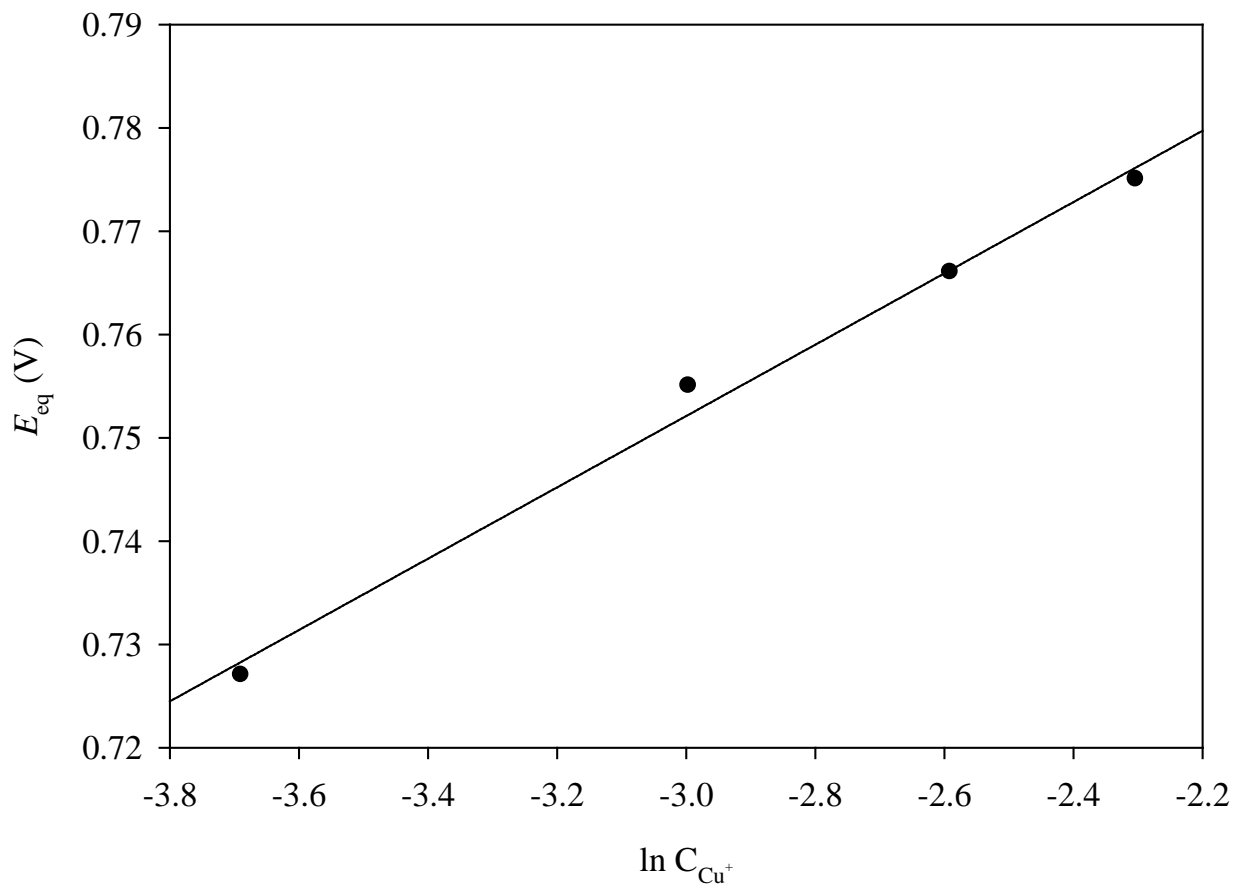


Figure 3.3.1: Nernst plot for the $\text{Cu}^+ + \text{e}^- \leftrightarrow \text{Cu}$ reaction in the 60 m/o AlCl_3 -EtMeImCl ionic liquid.

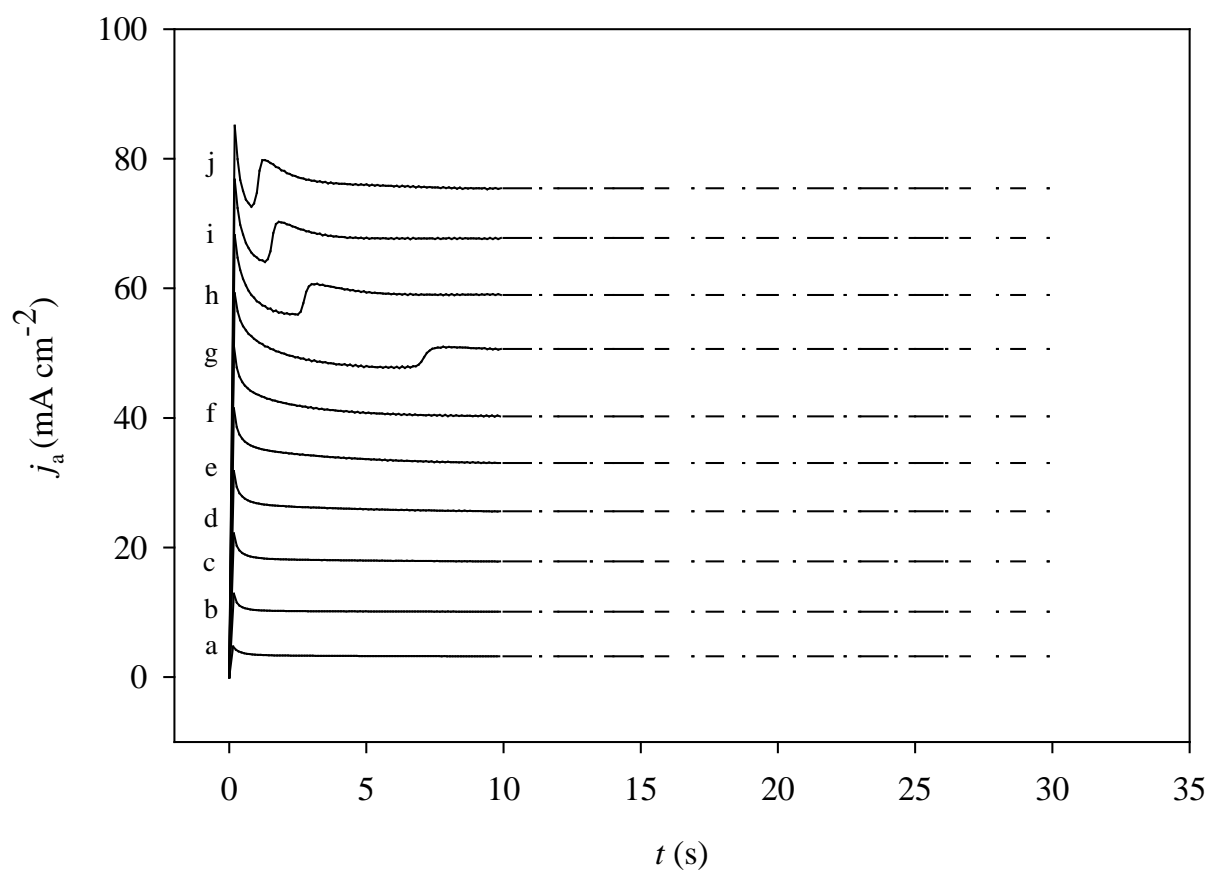


Figure 3.3.2: Current-time plots recorded during the anodization of Cu rotating disk electrode at different anodic overpotentials in the 60 m/o ionic liquid: (a) 0.8 V, (b) 0.9 V, (c) 1.0 V, (d) 1.1 V, (e) 1.2 V, (f) 1.3 V, (g) 1.4 V, (h) 1.5 V, (i) 1.6 V and (j) 1.7 V.

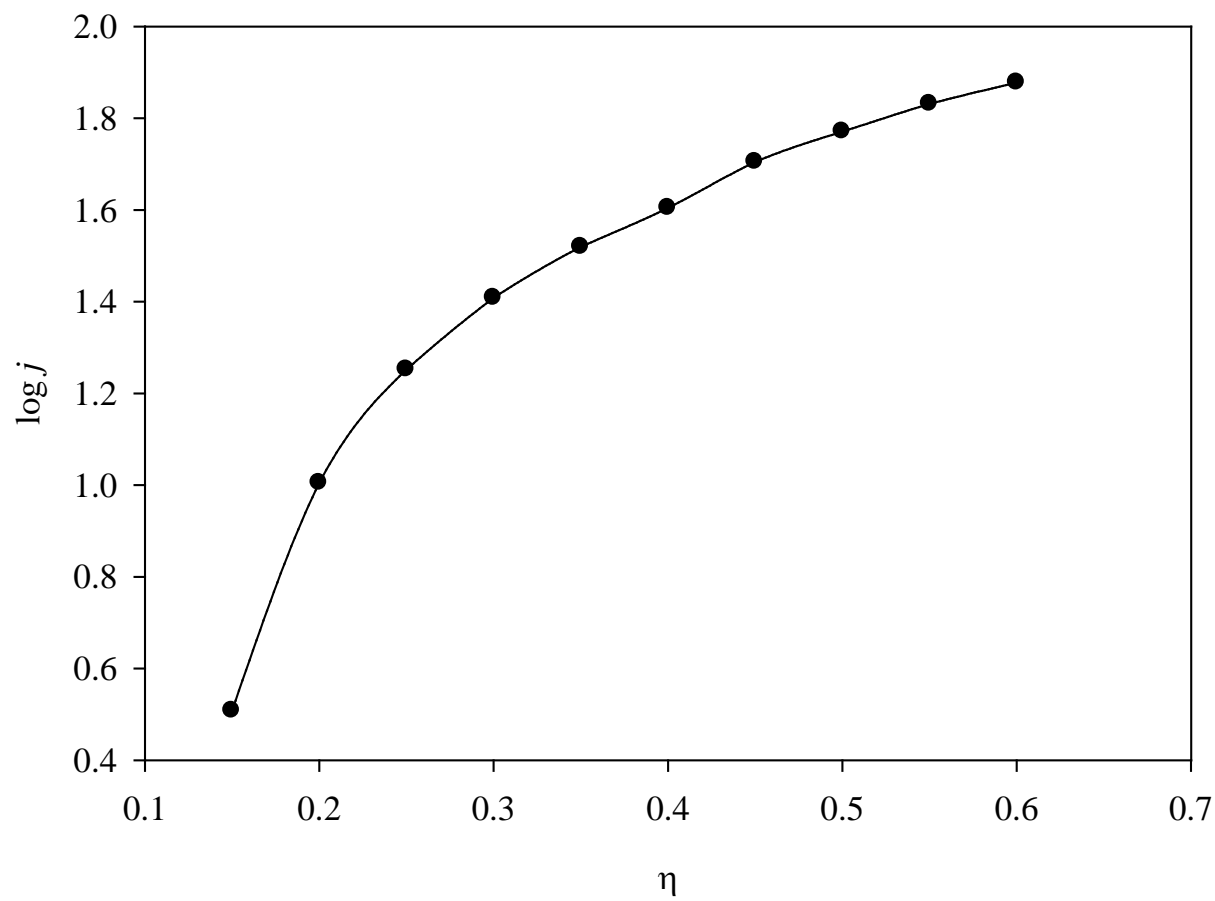


Figure 3.3.3: Example of a Tafel plot prepared from the data in Fig. 3.3.2.

$$1/j = 1/F(k_a - k_c C_{Cu^+}^*) + k_c/k_a [1.613(FD^{2/3})^{-1} \nu^{1/6}] \omega^{-1/2} \quad [3.3.2]$$

where k_a and k_c are the potential-dependent anodic and cathodic rate constants, and $C_{Cu^+}^*$ is the concentration of the reducible Cu(I) species in the ionic liquid. The first term in this expression, $F(k_a - k_c C_{Cu^+}^*)$ corresponds to the inverse kinetic current, $1/j_k$, at infinite rotation rate. Examples of these graphs with the extrapolated lines added to aid the eye are shown in Fig. 3.3.5. The intercepts correspond to $1/j_k$.

In order to study the relationship between the kinetic current and the concentration of Cu^+ , RDE measurements were performed in the ionic liquid with different concentrations of Cu^+ (25, 50, 75, and 100 mmol L⁻¹). Tafel plots for each concentration based on the corresponding Levich plots are shown in Fig. 3.3.6. These Tafel plots exhibit a linear segment at higher overpotentials, where the back reaction is negligible. The data obtained at higher overpotentials, $\eta \gg RT/nF$, can be used to extract Tafel slopes for analysis of the anodic dissolution mechanism. The exchange current density, j_0 , can be determined from the graph of $\log j_k$ versus η by extrapolation of the linear portions of these graphs to $\eta = 0$ according to Eq. 3.2.8. Like the anodization of Al in the same ionic liquid, the anodization of copper shows some involvement from the back reaction. In order to determine the order of the reaction with respect to C_{Cu^+} , more experiments were performed. As can be seen in Fig. 3.3.6, j_0 shows no obvious dependence on C_{Cu^+} , i.e., the partial derivative $(\partial \log j_k / \partial C_{Cu^+})_{T, P} = 0$.

The slope of this plot also gives an estimate of the anodic transfer coefficient, α_a .⁶² The exchange current density, j_0 , is related to the heterogeneous anodic rate constant, $k_{a,0}$, referenced to $\eta = 0$, and can be calculated by the relationship $j_0 = Fk_{a,0}$.³⁷ Based on the methods discussed above, the resulting values were: $j_0 = 7.00 \text{ mA cm}^{-2}$, $\alpha_a = 0.054$ and $k_{a,0} = 7.25 \times 10^{-8} \text{ cm}^{-1} \text{ s}$.

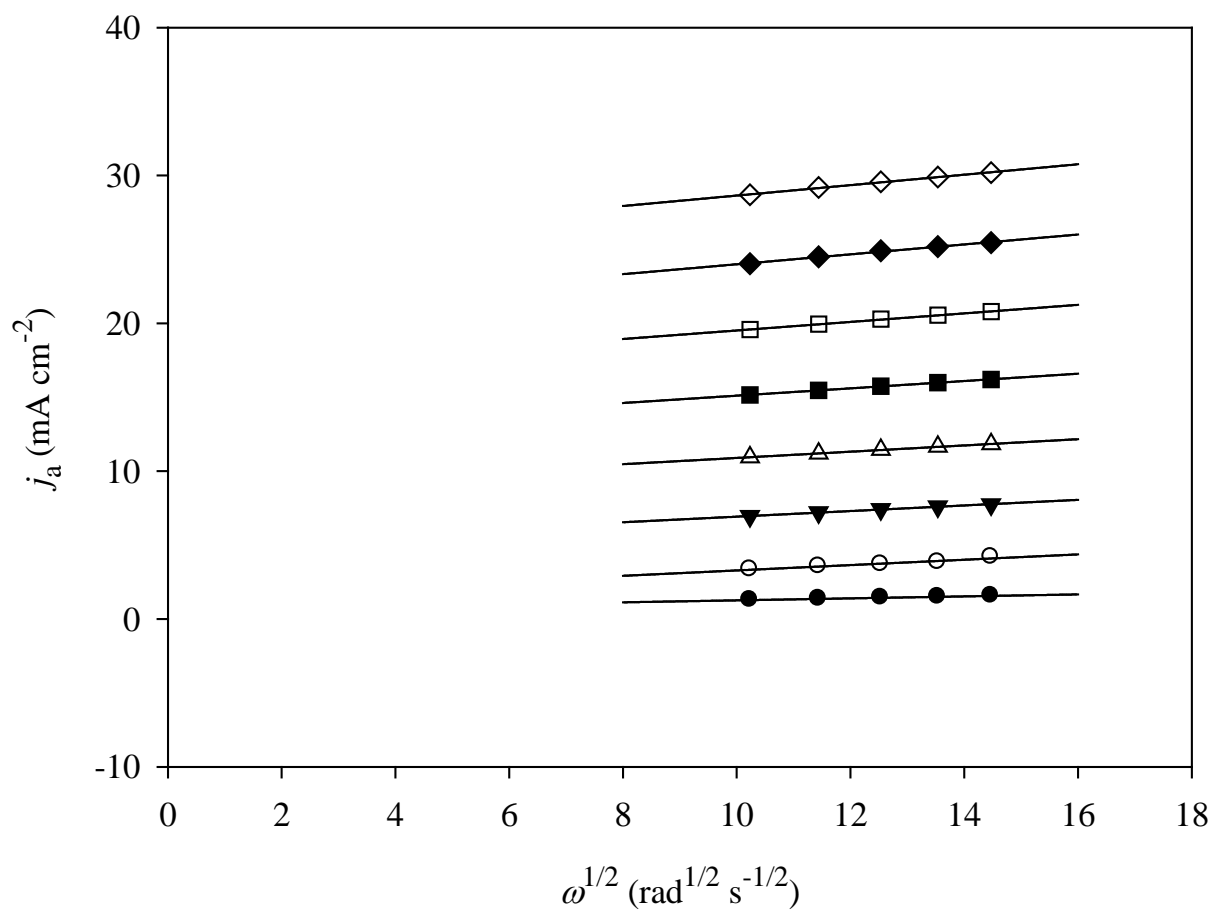


Figure 3.3.4: Examples of Levich plots for the anodization of a Cu RDE at 32°C in the 60 m/o ionic liquid.

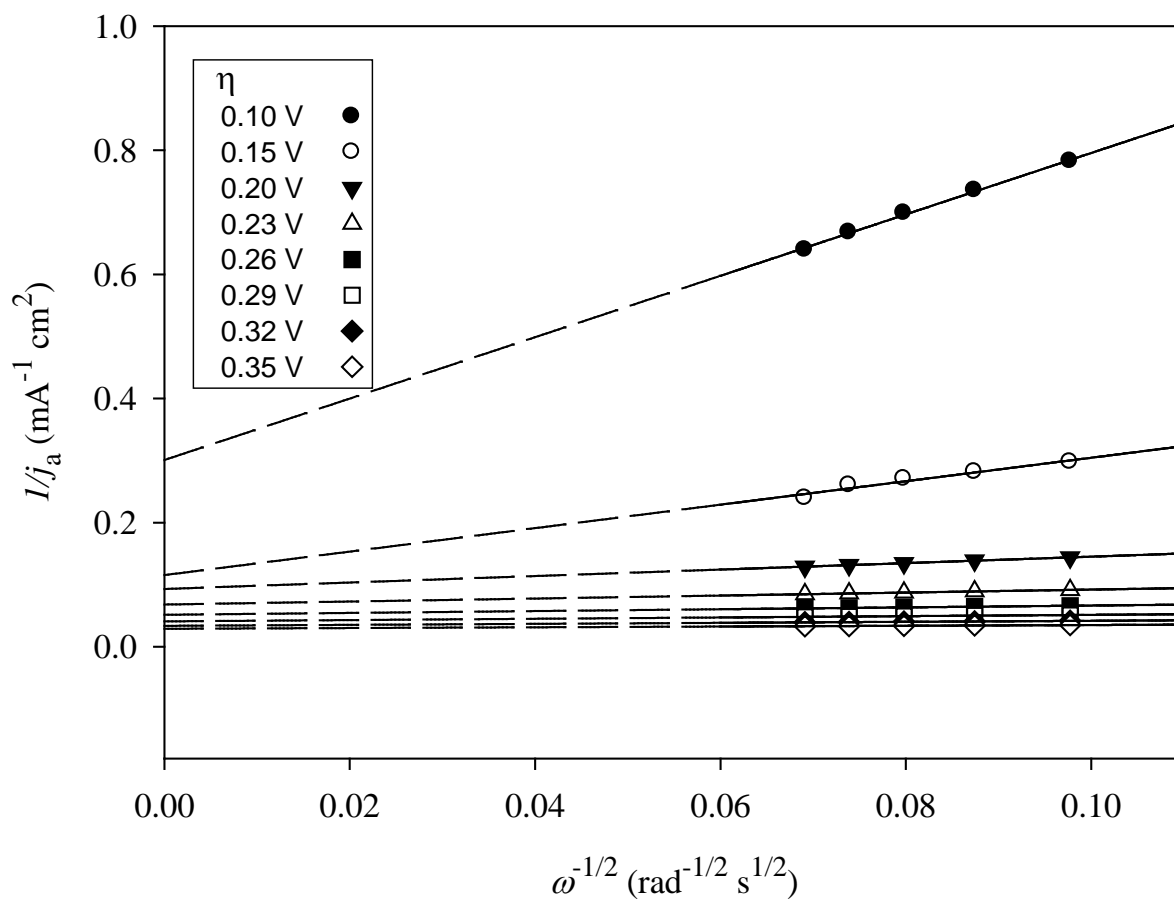


Figure 3.3.5: Examples of Koutecky-Levich plots, constructed from the data in Fig. 3.3.4: The anodic overpotentials were the same as those given in the previous figure. The dashed lines are drawn to aid the eye.

The apparent activation energy,⁶⁸ $\Delta G_{a,0}^{\#}$, for this anodic reaction can be estimated by determining j_0 at several additional temperatures using the same experimental procedures described above for Al. Because the expensive Pine Teflon-sheathed Cu RDE might be damaged above ~ 60 °C, only a small temperature range could be sampled with this electrode. The experimental data were very similar to those obtained at 31 °C, and for reasons of space and repetition, the Tafel plots are not reproduced here. A plot of $\log j_0$ versus $1/T$ that was constructed from this data is shown in Fig. 3.3.7. The points were recorded at 31, 41, 51 and 61°C. $\Delta G_{a,0}^{\#}$ was estimated from the slope of this plot with the Eq [3.2.9]. The resulting value of $\Delta G_{a,0}^{\#}$ is 19.7 kJ mol⁻¹. Next we report the oxidation of Cu in basic ionic liquid solutions containing Cl⁻.

3.3.2 Anodic Dissolution of Copper in Basic Chloroaluminate Ionic Liquids

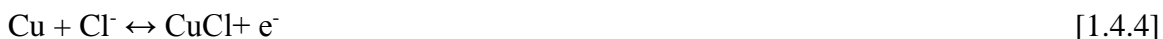
Before Cu dissolution experiments were conducted in basic ionic liquids, a cyclic voltammogram was recorded for a 25 mmol L⁻¹ solution of Cu(I) in 44 m/o AlCl₃-EtMeImCl at 30 °C. This voltammogram is shown in Fig. 3.3.8. The red trace indicates a scan starting at the equilibrium potential and proceeding toward negative potentials, reversing at about -0.8 V and then proceeding to the positive limit at 1.8 V before returning to the starting point. As can be seen during the negative-direction scan, copper metal is deposited on the working electrode at ~ -0.4 V and then removed at ~ 0.7 V. During the reverse scan, which proceeds to positive potentials first, there is no copper stripping peak at ~ 0.7 V because no copper has been deposited beforehand. Also, the peak at around 1.5 V is due to the oxidation of Cu(I) to Cu(II). Because this investigation will only focus on the anodization of copper to Cu(I), no experiments will be performed at potentials more positive than 1.2 V. This cyclic voltammetry experiment

also confirms that any Cu(I) in the solution is reduced to Cu⁰ at the counter electrode during the anodization of the copper electrode RDE. In other words, an aluminum wire can be used as counter electrode without any barrier or frit if it is desired to remove any Cu(I) generated during the anode reaction.

The procedure used to investigate of Cu oxidation in acidic ionic liquids was also used to study the anodization of Cu in the basic ionic liquids. That is, the oxidation current at a Cu-RDE was recorded as a function of time after the application of a series of potential steps. Figure 3.3.9 shows current-time plot recorded during the anodization of a Cu RDE at potentials extending from 0.1 V to 1.2 V. As can be seen in the Fig. 3.3.9, when the applied potentials are smaller than 0.50 V, the current is potential-dependent and time-independent throughout the duration of the experiment. However, as the reaction rate is increased by making the applied potential more positive, the current density increases with potential at first, but then decayed to a time- and potential-independent value. At a fixed rotation rate, all potentials more positive than 0.50 V but smaller than 1.1 V produced this same final steady-state current. These phenomena were very similar to the passivation process occurring on Al electrodes. Also, it has been shown that the CuCl film starts to build on the Cu surface.

In order to see the data more clearly, Fig. 3.3.10, which is a graph of the current density versus the applied potential, was prepared from the data in Fig. 3.3.9.

From these graphs, a possible explanation can be given by using the following equations:



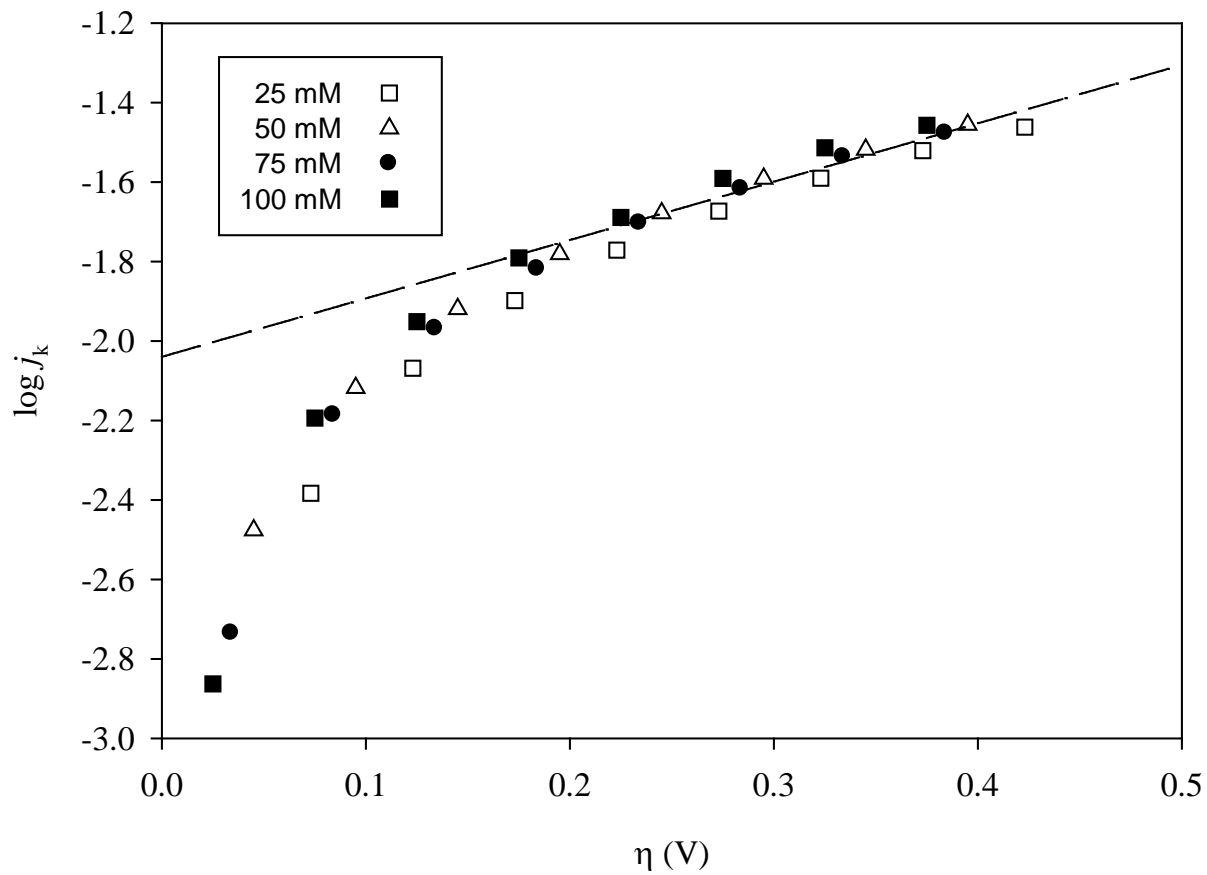


Figure 3.3.6: Tafel plots resulting from experiments conducted at different Cu^+ concentrations.

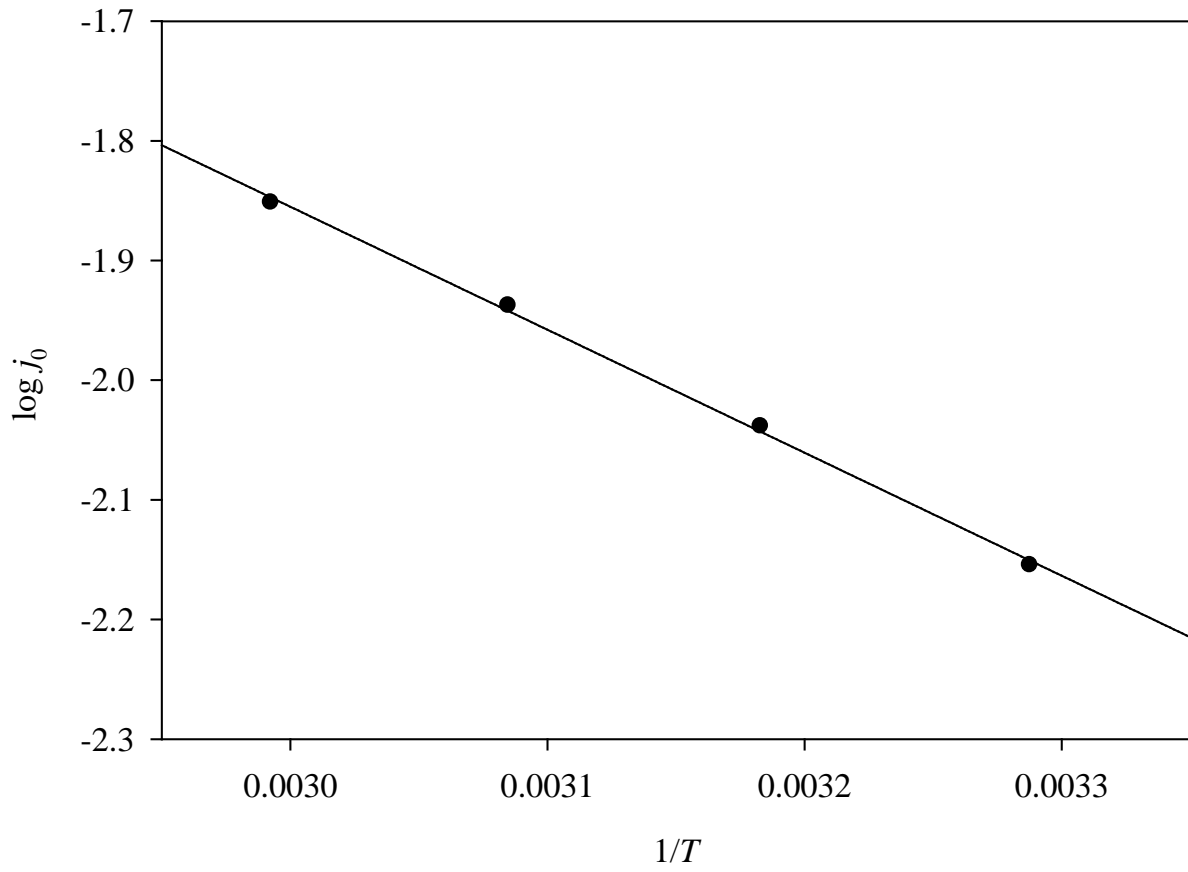


Figure 3.3.7: Arrhenius plot for the exchange current density referenced to the equilibrium potential.

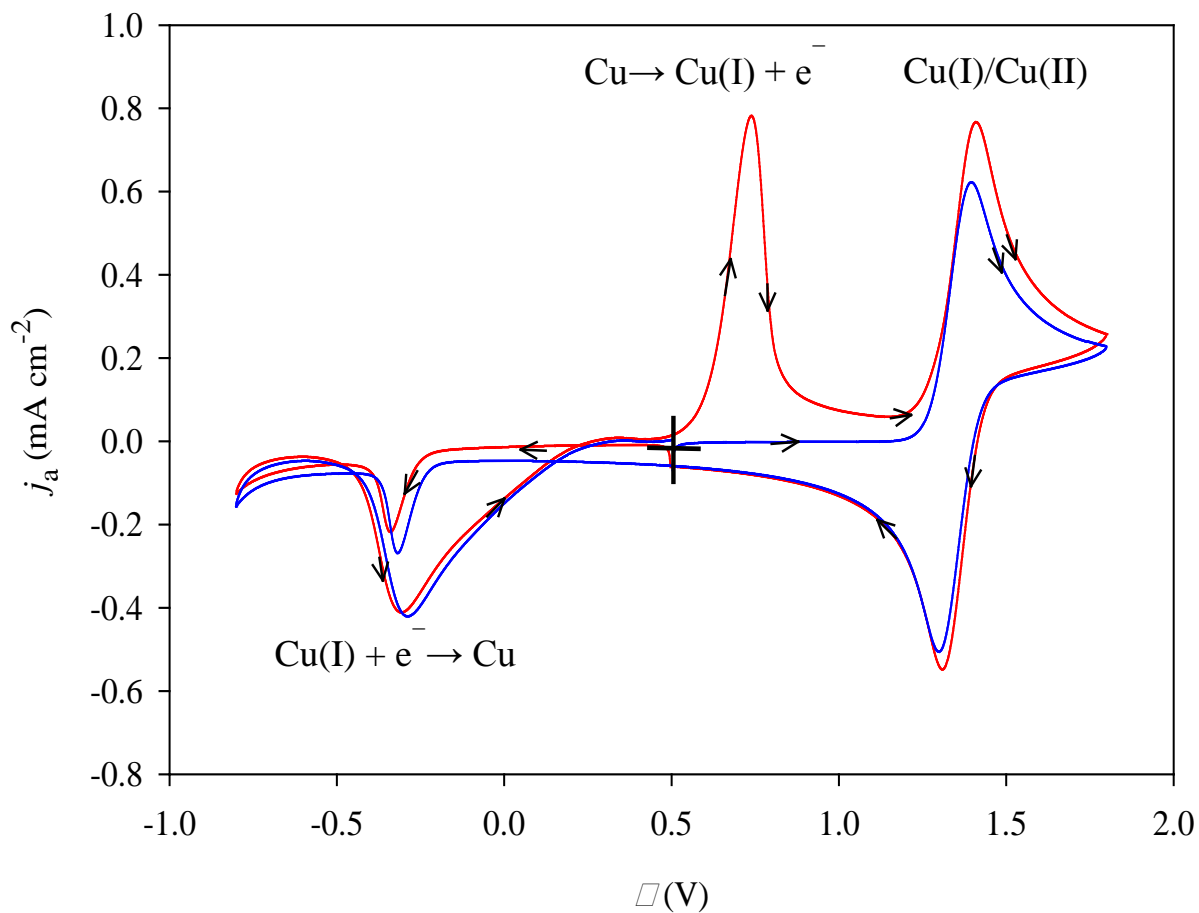


Figure 3.3.8: Cyclic voltammogram recorded at a Pt electrode at 30 °C in 44 m/o AlCl₃-EtMeImCl containing 25 mmol L⁻¹ Cu(I).

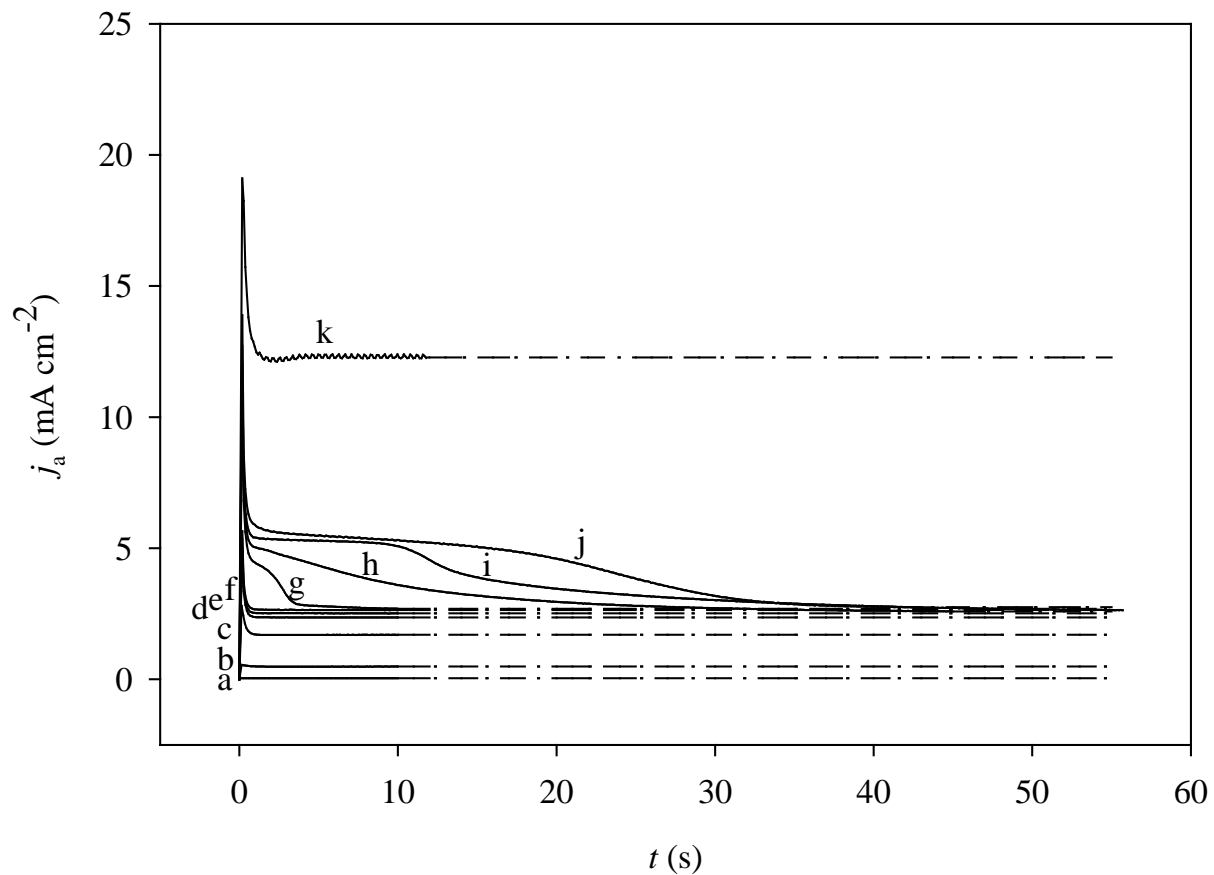


Figure 3.3.9: Current-time plots recorded during the anodization of Cu RDE at different applied potentials: (a) 0.1, (b) 0.2, (c) 0.3, (d) 0.4, (e) 0.5, (f) 0.6, (g) 0.7, (h) 0.8 V, (i) 1.0 V, (j) 1.1 V and (k) 1.2 V. $\text{AlCl}_3\text{-EtMeImCl}$ solution containing $75 \text{ mmol L}^{-1} \text{ Cl}^-$ at 30°C .

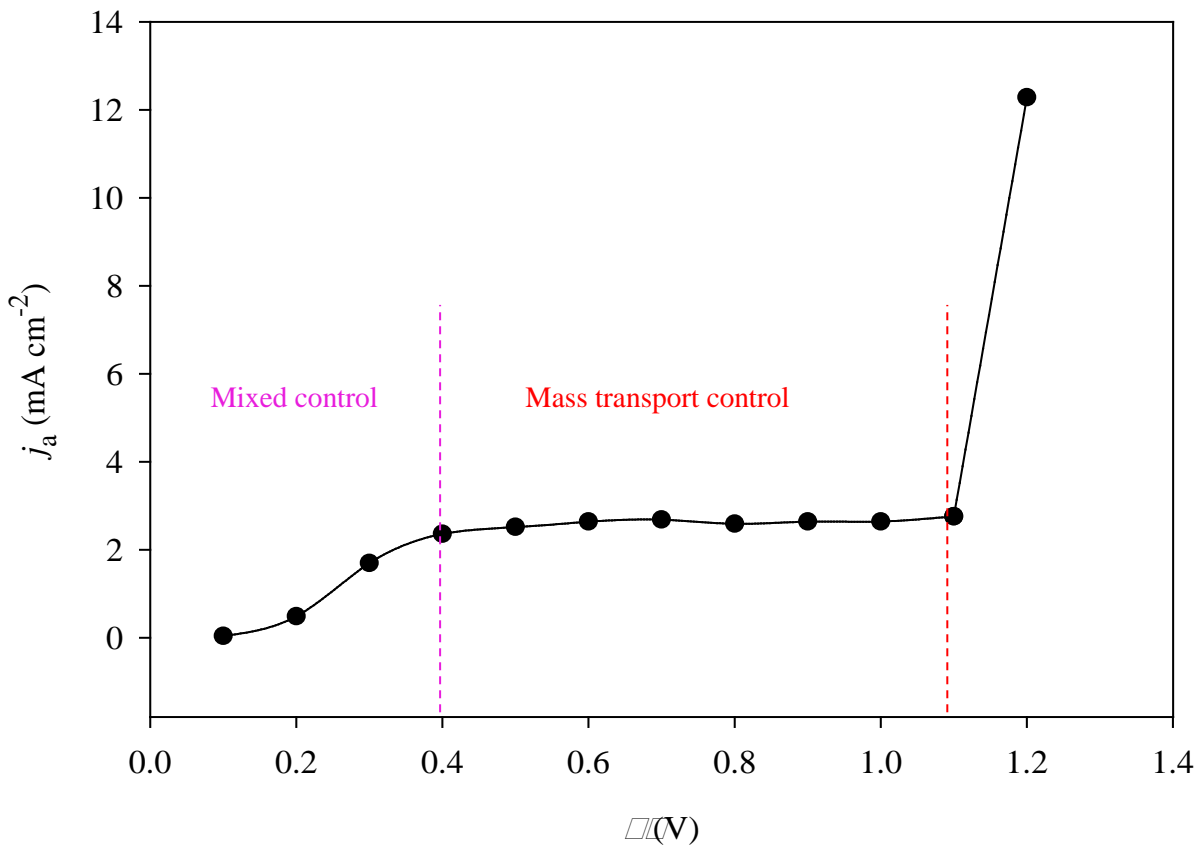


Figure 3.3.10: Current-potential plots constructed from data in the previous figure at 60 s.



At E_{app} below the onset of passivation, the electrode reaction proceeds completely according to the Eq. 1.4.4 and Eq. 1.4.5. In this potential range, Cu oxidation exhibits mixed control, which shows clearly in Fig. 3.3.10. As E_{app} is made more positive, and the rate of the Cu anodization reaction increases, the electrode diffusion layer becomes rich in CuCl. The solubility of this species is eventually exceeded, and the electrode becomes passivated by a thin layer of CuCl(s), as indicated in Eq. 3.3.20. Following the onset of passivation, the current densities reach limiting values, which are governed by the steady-state formation and dissolution of CuCl(s) according to Eq. 3.3.21. Thus, in this region, the Cu oxidation process is under pure mass-transport control. If the applied potential is increased further, the one-electron oxidation of Cu(I) to Cu(II) is observed, which is shown in Eq. 3.3.22. That is why the current increases at potentials above 1.1 V in agreement with the results in Fig. 3.3.8. As shown in Fig. 3.3.10, at smaller overpotentials, i.e., ≤ 0.40 V, the Cu anodization process proceeds without apparent formation of the passivation layer. We investigated the dissolution of Cu in this potential region at the Cu RDE electrode by applying overpotentials from 0.17 V to 0.45 V at different rotation rates. Levich plots were constructed from the resulting data, and examples are shown in Fig.

3.3.11. These plots are mostly linear, but do not pass through the origin. These data are similar to those obtained during the anodic dissolution of Al in LiAlBr₄-NaAlCl₄-KAlCl₄ (30-50-20 m/o)³¹ and AlCl₃-EtMeImCl under mixed control. When Cu oxidation exhibits mixed control at potentials below 0.4 V, there are two possible diffusion limited species, either CuCl₂⁻ or Cl⁻.



To probe this question, Professor Kenneth Nobe³⁴ proposed two models, which are shown below, based on the assumption of a two-step mechanism, involving Eq. 3.3.23 and Eq. 3.3.24. Here,

$$K_0 = \frac{k_2 k_1}{k_{-1}} \exp(FE_{\text{eq}}/RT).$$

$$\frac{1}{j} = \frac{1}{FK_0 C_{\text{Cl}^-}{}^{-2}} + \frac{1.62 k_{-2}}{FD_{\text{CuCl}_2^-}{}^{-2/3} \nu^{-1/6} K_0 C_{\text{Cl}^-}{}^{-2} \omega^{1/2}} \quad [3.3.25]$$

$$\frac{1}{j} = \frac{1}{FK_0 C_{\text{Cl}^-}{}^{-2}} + \frac{3.24}{FD_{\text{Cl}^-}{}^{-2/3} \nu^{-1/6} C_{\text{Cl}^-}{}^{-2} \omega^{1/2}} \quad [3.3.26]$$

Based on this assumption, if CuCl₂⁻ is the diffusion-limited species, Eq. 3.3.25 results, and the slope of a plot of j^{-1} vs $\omega^{-1/2}$ plot should be proportional to $C_{\text{Cl}^-}{}^{-2}$. However, if the slope is proportional to C_{Cl^-} , Cl⁻ is the diffusion limited species (Eq. 3.3.26). In another word, if we make

a plot of $\log(\partial j^{-1} / \partial \omega^{-1/2})$ versus $\log C_{\text{Cl}^-}$, which is shown in Fig. 3.3.12, since the slope is close to -2, that confirms that the first model is correct. CuCl_2^- is the diffusion-limiting species. This is similar to what is observed in aqueous solutions.

Following the work with Al, information about the kinetics of the heterogeneous dissolution reaction rate can be extracted from this data by constructing Koutecky-Levich plots (Fig. 3.3.12), i.e., plots of $1/j_a$ versus $\omega^{-1/2}$

$$1/j_a = 1/(Fk_a) + k_c/k_a [1.613(FD^{2/3})^{-1} \nu^{1/6}] \omega^{-1/2} \quad [3.3.27]$$

Potential-dependent anodic and cathodic heterogeneous rate constants are written as k_a and k_c . In case the back reaction is not negligible, we construct graphs classical Tafel plots like that in Fig. 3.3.6, to calculate the exchange current density, j_0 . As can be seen on Fig. 3.3.14, the Tafel plot is linear, which is because there is no Cu^+ presents in the basic ionic liquid. This also verifies that the Al counter electrode did help trapping the Cu^+ formed on the working electrode. And the exchange current density can be calculated by using Eq. 3.1.9.

Examples of a graph with the extrapolated anodic Tafel lines are shown in Fig. 3.3.14. The slopes of these were used to estimate α_a , and the resulting values of j_0 were used to calculate the $k_{a,0}$. These data are given in Table 3.3.1.

The resulting values of j_0 , α_a , and $k_{a,0}$ for the Cu electrode in ionic liquids with different Cl^- are given in Table 3.3.1. It is a reasonable conclusion that j_0 is about the same for the four different ionic liquid compositions, that is because the difference between the results in the four

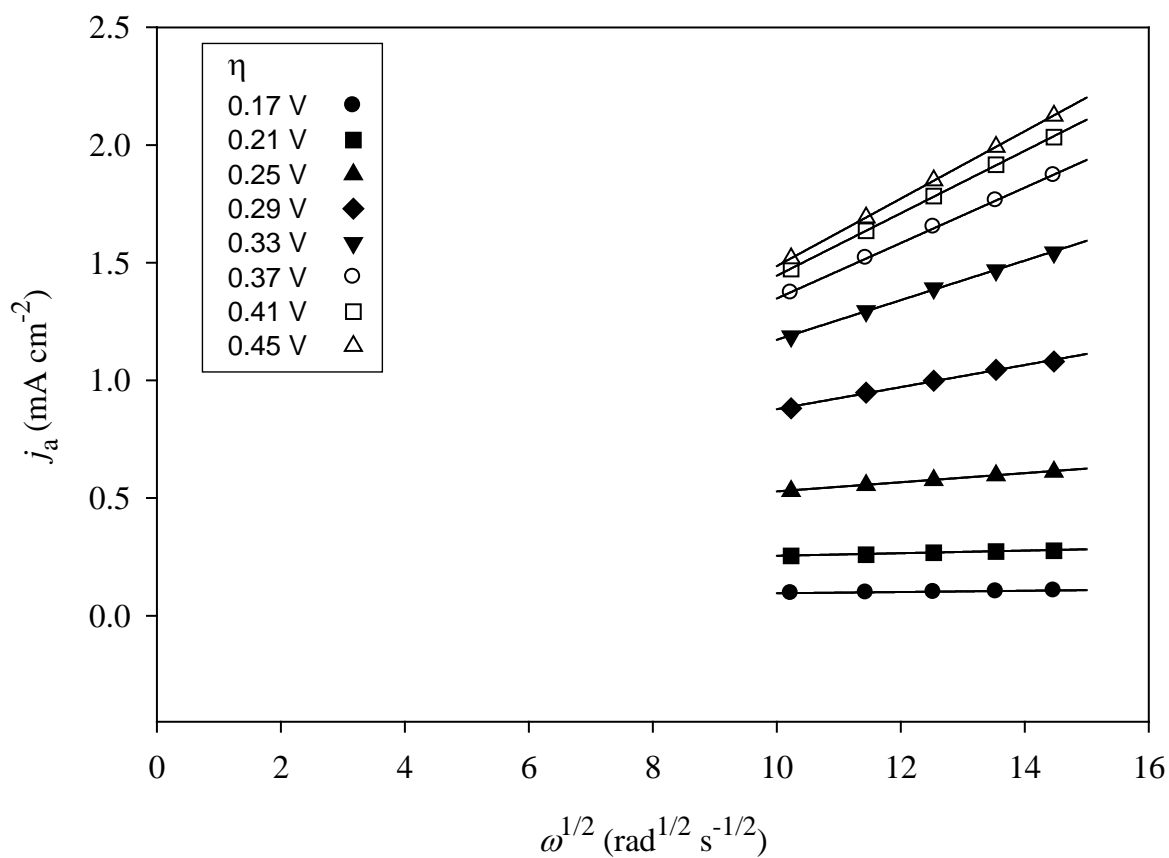


Figure 3.3.11: Examples of Levich plots for the anodization of a Cu RDE at 32°C in the ionic liquid containing 75 mmol L⁻¹ Cl⁻. The anodic overpotentials were: (●) 0.17 V, (■) 0.21 V, (▲) 0.25 V, (◆) 0.29 V, (▼) 0.33 V, (○) 0.37 V, (□) 0.41 V, and (△) 0.45 V.

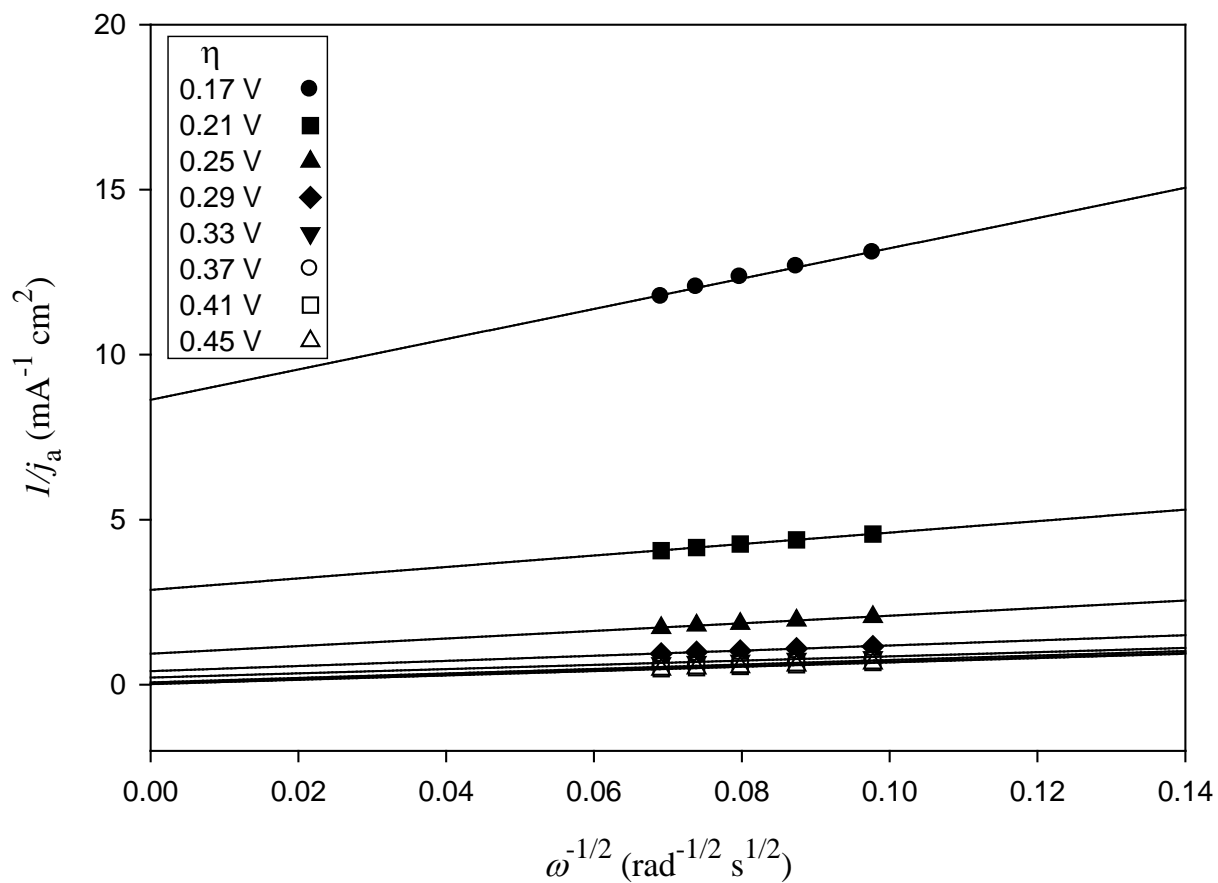


Figure 3.3.12: Examples of Koutecky-Levich plots for the anodization of Cu Electrodes at 32°C in the ionic liquid containing 75mmol L⁻¹ Cl⁻. The anodic overpotentials were: (●) 0.17 V, (■) 0.21 V, (▲) 0.25 V, (◆) 0.29 V, (▼) 0.33 V, (○) 0.37 V, (□) 0.41 V, and (△) 0.45 V.

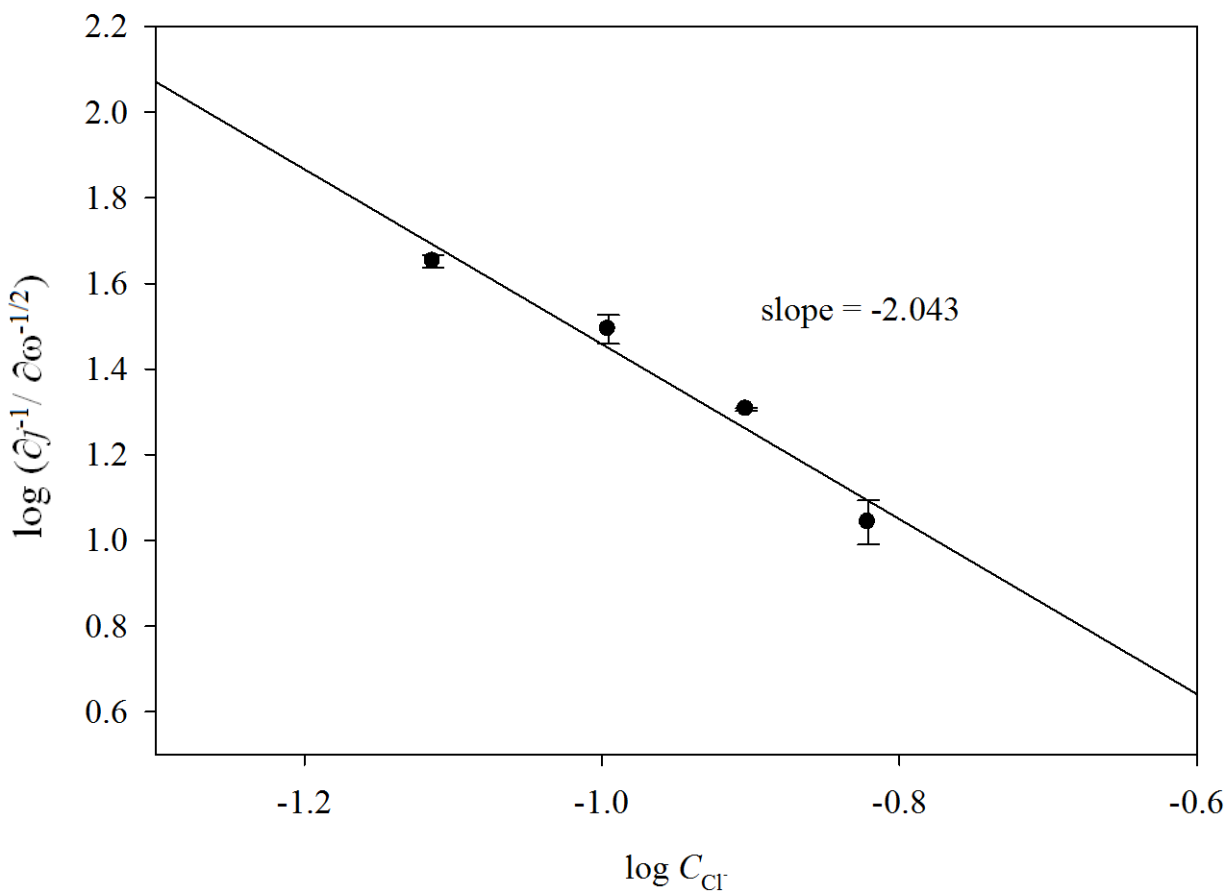


Figure 3.3.13: Log- log plot of $\partial_j^{-1} / \partial \omega^{-1/2}$ versus the Cl^- concentration at 30 °C, $\eta = 0.17$

V.

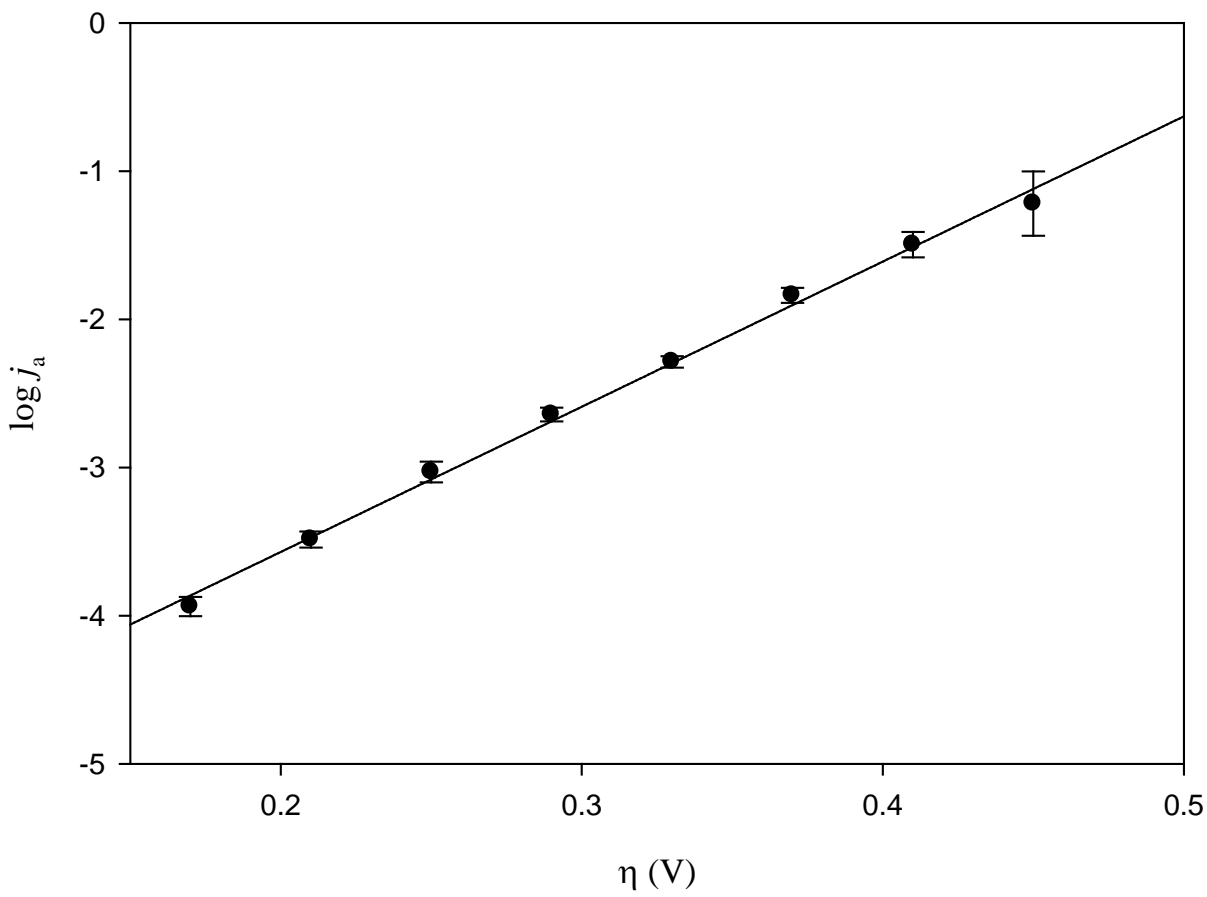


Figure 3.3.14: Examples of Tafel plots recorded at a Cu RDE prepared from the data in Fig. 3.3.12. The error bars represent the 95 % C.I.

ionic liquids are very small. However, the 75 mmol L⁻¹ Cl⁻ solution is little off, this might due to the difficulty in controlling the small amount of Cl⁻ in the solution. The α_a , anodic transfer coefficients in the different composition are close to each other and also close to 0.5, which suggests that the rate determining step of the copper anodization reaction is the indeed electron transfer step. Note this result is much different from that recorded for the three-electron oxidation Al.

3.3.3 Summary

Like the anodization of Al in the acidic AlCl₃-EtMeImCl ionic liquid, the anodization of Cu proceeds under mixed kinetic and mass-transport control in both acidic and basic ionic liquids at small positive overpotentials. However, in basic ionic liquids, the anodization reaction transits to a mass-transport limited process due to the formation of a passive layer of CuCl on the Cu electrode. This phenomenon doesn't occur in the acid ionic liquid because there are no available chloride ions in the acidic composition, precluding the formation of CuCl. Also, when the anodization reaction is under mixed kinetic and mass transport control in the basic solution, CuCl₂⁻ is the diffusion limited species, not Cl⁻.

Table 3.3.1: RDE results for the anodization of Al in the Lewis basic AlCl₃-EtMeImCl ionic liquid.

| Mmol L ⁻¹ Cl ⁻ in AlCl ₃ -EtMeImCl | log j_0 | α_a |
|---|-----------------------|------------|
| 75 | -5.664 | 0.589 |
| 100 | -4.472 | 0.517 |
| 125 | -4.775 | 0.551 |
| 150 | -4.786 | 0.542 |
| Average value of j_0 | 1.72×10^{-5} | |
| Average value of α_a | | 0.550 |
| $k_{a,0}$ (cm s ⁻¹) | 8.21×10^{-8} | |

LIST OF REFERENCES

1. G. L. Holleck and J. Giner, *J. Electrochem. Soc.*, **119**, 1161 (1972).
2. H. A. Hjuler, R. W. Berg, and N. J. Bjerrum, unpublished results.
3. K. P. Rajurkar, M. M. Sundaram, and A. P. Malshe, *Procedia CIRP*, **6**, 13 (2013).
4. J. A. McGeough, *Principles of Electrochemical Machining*, CRC Press (1974).
5. M. Datta and D. Landolt, *Electrochim. Acta.*, **26**, 899 (1981).
6. J. Bannard, *J. Appl. Electrochem.*, **7**, 1 (1977).
7. D. T. Chin, *J. Electrochem. Soc.*, **11**, 174 (1971).
8. G. Song, A. Atrens, D. St John, X. Wu, and J. Nairn, *Corros. Sci.*, **39**, 1981 (1997).
9. P. Marcus and F. B. Mansfeld, *Analytical Methods in Corrosion Science and Engineering*, CRC Press (2005).
10. C. L. Hussey and G. Mamantov, in *Advances in Molten Salt Chemistry*, Vol. 5, Elsevier, New York (1983).
11. R. W. Berg, H. A. Hjuler, and N. J. Bjerrum, *Inorg. Chem.*, **23**, 557 (1984).
12. I. Galasiu, R. Galasiu, and J. Thonstad, in *Nonaqueous Electrochemistry*, D. Aurbach Editor, CRC Press, Boca Raton, FL (1999).
13. H. A. Hjuler, S. von Winbush, R. W. Berg, and N. J. Bjerrum, *J. Electrochem. Soc.*, **136**, 901 (1989).
14. F. H. Hurley and T. P. Wier Jr., *J. Electrochem. Soc.*, **98**, 203 (1951).
15. R. J. Gale and R. A. Osteryoung, *Inorg. Chem.*, **18**, 1603 (1979).
16. R. J. Gale and R. A. Osteryoung, *J. Electrochem. Soc.*, **127**, 2167 (1980)
17. J. S. Wilkes, J. A. Levisky, R. A. Wilson, and C. L. Hussey, *Inorg. Chem.*, **21**, 1263 (1982).

18. C. Scordilis-Kelley, J. Fuller, R. T. Carlin, and J. S. Wilkes, *J. Electrochem. Soc.*, **139**, 694 (1992).
19. C. L. Hussey, T. B. Scheffler, J. S. Wilkes, and A. A. Fannin Jr., *J. Electrochem. Soc.*, **139**, 694 (1992).
20. N. H. Hansen, R. Fehrmann, and N. J. Bjerrum, *Inorg. Chem.*, **21**, 744 (1982).
21. B. Del Duca, *J. Electrochem. Soc.*, **118**, 405 (1971).
22. R. Piontelli and U. Ducati, *J. Electrochem. Soc.*, **118**, 1966 (1971).
23. Q. Li and N. J. Bjerrum, *J. Power Sources*, **20**, 1 (2002).
24. R. J. Gale and R. A. Osteryoung, *J. Electrochem. Soc.*, **121**, 983 (1974).
25. J. Fischer and K. Leadbetter, <http://engineering.und.edu/research/aemc/aluminum-plating-report-01-15-2014.pdf> (2014).
26. A. P. Abbott, G. Frisch and K. S. Ryder, *Annu. Rev. Mater. Res.*, **43**, 335 (2013).
27. B. Tremillon and G. Letisse, *J. Electroanal. Chem.*, **17**, 371 (1968).
28. Y. Zhao and T. J. VanderNoot, *Electrochim. Acta*, **42**, 3 (1997).
29. B. Gilbert, D. L. Brotherton and G. Mamantov, *J. Electrochem. Soc.*, **121**, 773 (1974).
30. R. T. Carlin and R. A. Osteryoung, *J. Electrochem. Soc.*, **136**, 1409 (1989).
31. C. Wang and C. L. Hussey, *J. Electrochem. Soc.*, **162**, H151 (2015).
32. H. Lai and H. R. Thirsk, *J. Chem. Soc.*, 2638 (1953).
33. M. Braun and K. Nobe, *J. Electrochem. Soc.*, **126**, 1666 (1979).
34. H. P. Lee and K. Nobe, *J. Electrochem. Soc.*, **133**, 2035 (1986).
35. G. Kear, B. D. Barker, and F. C. Walsh, *Corros. Sci.*, **46**, 109 (2004).
36. L. Brossard, *J. Electroanal. Chem.*, **130**, 403 (1983).
37. G. Faita, G. Fiori, and D. Salvatore, *Corros. Sci.*, **15**, 383 (1975).

38. W. F. Smith, *Foundations of Materials Science and Engineering*, McGraw-Hill (2004).
39. S. R. de Sanchez and D. J. Schiffrin, *Corros. Sci.*, **22**, 585 (1982).
40. S. R. de Sanchez and D. J. Schiffrin, *Corros. Sci.*, **28**, 141 (1988).
41. F. K. Crundwell, *Electrochim. Acta.*, **37**, 2707 (1992).
42. B. Tribollet and J. Newman, *J. Electrochem. Soc.*, **131**, 2780 (1984).
43. V. G. Levich, *Physicochemical Hydrodynamics*, Prentice-Hall, Englewood Cliffs, NJ, (1962).
44. L. Kiss, *Kinetics of Electrochemical Metal Dissolution*, p. 260, Elsevier, Amsterdam (1988).
45. D. Pletcher, R. Greef, R. Peat, L. M. Peter, and J. Robinson, *Instrumental Methods in Electrochemistry*, Ellis Horwood (2001).
46. A. J. Bard and L. R. Faulkner, *Electrochemical Methods : Fundamentals and Applications*, John Wiley & Sons, New York (2001).
47. I. L. Alanis and D. J. Schiffrin, *Electrochim. Acta*, **27**, 837 (1982).
48. F. G. Cottrell, *Z. Phys. Chem.* **42**, 385 (1903).
49. M. E. Orazem and B. Tribollet, *Electrochemical Impedance Spectroscopy*, John Wiley & Sons, New York (2008).
50. Solartron Analytical, Technical Report 6 (1999).
51. A. A. Fannin, F. C. Kibler, L. A. King and D. W. Seegmiller, *J. Chem. Eng. Data*, **19**, 266 (1974).
52. W. Brockner, K. Tørklep and H. A. Øye, *Ber. Bunsenges Phys. Chem.*, **83**, 1 (1979).
53. R. A. Carpio, F. C. Kibler, L. A. King, W. Brockner, K. Tørklep and H. A. Øye, *Ber. Bunsenges Phys. Chem.*, **85**, 31 (1981).

54. R. A. Carpio, L. A. King, F. C. Kibler and A. A. Fannin, *J. Electrochem. Soc.*, **126**, 1650 (1979).
55. G. J. Janz, *J. Phys. Chem. Ref. Data*, **17**, 271 (1988).
56. W. Xu, E. I. Cooper and C. A. Angell, *J. Phys. Chem. B*, **107**, 6170 (2003).
57. C. Schreiner, S. Zugman, R. Hartl and H. J. Gores, *J. Chem. Eng. Data*, **55**, 1784 (2010).
58. D. R. MacFarlane, M. Forsyth, E. I. Izgorodina, A. P. Abbott, G. Annat and K. J. Fraser, *Phys. Chem. Chem. Phys.*, **11**, 4962 (2009).
59. Y. Pan, L. E. Boyd, J. F. Kruplak, W. E. Cleland, J. S. Wilkes and C. L. Hussey, *J. Electrochem. Soc.*, **158**, F1 (2011).
60. M. Yoshizawa, W. Xu and C. A. Angell, *J. Am. Chem. Soc.*, **125**, 15411 (2003).
61. K. Nitta, T. Nohira, R. Hagiwara, M. Majima and S. Inazawa, *Electrochim. Acta*, **54**, 4898 (2009).
62. R. Guidelli, R. G. Compton, J. M. Feliu, E. Gileadi, J. Lipkowsky, W. Schmickler and S. Trasatti, *Pure Appl. Chem.*, **86**, 259 (2014).
63. A. A. Fannin, D. A. Floreani, L. A. King, J. S. Landers, B. J. Piersma, D. J. Stech, R. L. Vaughn, J. S. Wilkes and J. L. Williams, *J. Phys. Chem.*, **88**, 2614 (1984).
64. H. A. Hjuler, R. W. Berg, K. Zachariassen and N. J. Bjerrum, *J. Chem. Soc.*, **30**, 203 (1985).
65. Y. K. Delimarskii, V. F. Makogon and A. Y. Zhigailo, *Elektrokhimiya*, **5**, 108 (1969).
66. V. N. Storozhenko, *Elektrokhimiya*, **8**, 973 (1972).
67. M. Datta and D. Verduyn, *J. Electrochem. Soc.*, **137**, 3016 (1990).
68. T. J. Schmidt, P. N. Ross Jr, and N. M. Markovic, *J. Electroanal. Chem.*, **524-525**, 252 (2002).

VITA

Mr. Chen Wang was born March 15, 1988 in Shijiazhuang, Hebei Province, Peoples Republic of China. He is the son of Mr. Jianhai Wang and Ms. Lingling Zuo. After graduating from the No. 2 High School of Shijiazhuang in the summer of 2006, he enrolled in the Department of Chemical Engineering at Hebei University of Technology, Tianjin, China, receiving his Bachelor of Engineering degree in 2010. In 2009, he was admitted to the Department of Chemistry at Winona State University as an exchange student. In August, 2010, he enrolled in the chemistry graduate program in the Department of Chemistry and Biochemistry at the University of Mississippi. He joined the research group of Professor Charles L. Hussey in the summer of 2012. There he began the investigations described in this dissertation. He is married to Ms. Jing Ma in 2013. They have a daughter, Evelin. His permanent address is: No. 122 Yuhua West Road, Qiaoxi District, apt. 2-2-303, Shijiazhuang, Hebei, China, 050000.